



TECHNISCHE  
UNIVERSITÄT  
WIEN

## PhD Thesis

Dissertation

# 3D Printed Micro-Environments as Biomimetic *In Vitro* Models

ausgeführt zum Zwecke der Erlangung des akademischen Grades eines  
Doktors der technischen Wissenschaften

unter der Leitung von

**Univ.Prof. Dr.Heinz Redl**

Institut für Verfahrenstechnik, Umwelttechnik und Technische Biowissenschaften

und Co-Betreuung von

**Univ.Prof. Dr. Aleksandr Ovsianikov**

Institut für Werkstoffwissenschaften und Werkstofftechnologie

eingereicht an der Technischen Universität Wien

Fakultät für Technische Chemie

von

**Agnes Dobos, MSc**

01652643

Wien, 27.02.2019

Agnes Dobos, MSC

# Abstract

One of the main challenges of current biomedical research and drug development is the lack of available physiological *in vitro* models. Traditionally *in vitro* research was performed using two-dimensional cell culture methods. However, there has been an increasing evidence that culturing cells under planar conditions do not recapitulate the complexity of the three-dimensional (3D) environment cells experience in the body, which often results in increased drug response at preclinical research phase. Multiple different approaches have been developed over the last decades to introduce 3D microenvironments for cells, either by “bottom up” or “top down” technologies. In the bottom up method, the cells self-assemble without any mechanical support and form aggregates (spheroids), while the top down production of 3D cell cultures involves the use of scaffolds which later on can be seeded with cells.

Two photon-polymerization (2PP) is a high-definition 3D printing approach, where the absorption of femtosecond-pulsed laser radiation leads to localized cross-linking of photosensitive materials within the focal volume enabling the direct embedding of cells inside photosensitive hydrogels at high structural resolution in accordance to a computer assisted designs. Structures can be printed within the bulk of the material eradicating the need of a layer-by-layer deposition, which is required in other 3D printing technologies.

One of the main bottlenecks of using 2PP for biofabrication is the lack available biocompatible photoinitiators and bioinks. The aim of the thesis is to establish the printing conditions and material compositions which allows the embedding of cells directly into the bioink, while maintaining cell viability. Several different materials can be employed as bioinks for 2PP including natural and synthetic photopolymers. One of the main advantages of natural hydrogels is that they are often derived from the non-cellular compartment of the tissues, the extracellular matrix, therefore they contain the necessary biological and mechanical cues the cells require. The ultimate goal of this thesis is to use 2PP platform to create biomimetic tissue models and disease models and study cell behaviour in complex 3D environment.

# Acknowledgement

I would like to express my thanks to all the people who helped me during the course of this research.

First and foremost, I would like to thank my supervisor Aleksandr Ovsianikov giving me the opportunity to do my PhD in this group and his help and support during this work. I would also like to thank Heinz Redl for his support. I would like to express my very great appreciation to Marica Markovic for her never-ending support and her continuing trust throughout my PhD and I am really lucky to call her my friend. I would like to thank Jasper Van Hoorick for years of fruitful discussions about science and (not-so fruitful ones) about not-science and I am really looking forward to continue working with you in the future. I would also like to thank my wonderful colleagues; Wolfgang Steiger whose enthusiasm is unmatched when it comes to lasers and movies; Peter Gruber for building the coolest printer there is and for always being there when needed; Elise Zerobin who makes everything so much fun; Franziska Gartner, my first project student, who just continues to be the most hard working and amazing PhD student and Markus Lunzer for being Markus Lunzer especially when it came to correcting manuscripts. I would also like to thank all our collaborators in Ghent, Austria and Los Angeles for their help throughout these projects.

Most importantly a special appreciation is due to my parents, siblings and friends. I am extremely grateful for their encouragement, their never-ending support and patience all these years. None of this would have been possible without them.

# Contents

Abstract .....	ii
Acknowledgement .....	iii
Contents .....	iv
List of Figures .....	vii
List of Tables .....	xi
Abbreviations .....	xii
1 Introduction .....	16
2 Bioinks and Biocompatible Two-Photon Initiators .....	20
2.1 A biocompatible diazosulfonate initiator for direct encapsulation of human stem cells via two-photon polymerization .....	20
2.1.1 Introduction .....	21
2.1.2 Aim.....	22
2.1.3 Experimental .....	22
2.1.4 Results and Discussion.....	25
2.1.5 Conclusion .....	30
2.2 Alternative Strategies Towards Improving Cell Viability During Encapsulation	31
2.2.1 Introduction .....	32
2.2.2 Aim.....	33
2.2.3 Experimental .....	33
2.2.4 Results and Discussion.....	34
2.2.5 Conclusion .....	49
2.3 Thiol-Gelatin-Norbornene Bioink for Laser-based High-Definition Bioprinting	50
2.3.1 Introduction .....	51

2.3.2	Aim.....	52
2.3.3	Experimental.....	53
2.3.4	Results and Discussion.....	58
2.3.5	Conclusion .....	67
3	Applications.....	69
3.1	On-Chip High-Definition Bioprinting of Microvascular Structures.....	69
3.1.1	Introduction .....	70
3.1.2	Aim.....	72
3.1.3	Experimental.....	72
3.1.4	Results and Discussion.....	77
3.1.5	Conclusion .....	88
3.2	Glioblastoma-on Chip.....	89
3.2.1	Introduction .....	90
3.2.2	Aim.....	92
3.2.3	Experimental.....	93
3.2.4	Results and Discussion.....	98
3.2.5	Conclusion .....	112
3.3	Screening of Two-Photon Activated Photodynamic Therapy Sensitizers Using a 3D Osteosarcoma Model.....	114
3.3.1	Introduction .....	115
3.3.2	Aim.....	117
3.3.3	Experimental.....	119
3.3.4	Results and Discussion.....	123
3.3.5	Conclusion .....	131
3.4	T-cell Activation in 3D microenvironments.....	132
3.4.1	Introduction .....	133

3.4.2	Aim.....	133
3.4.3	Experimental.....	134
3.4.4	Conclusion .....	141
4	Conclusion .....	142
5	Bibliography .....	144
6	Curriculum Vitae.....	166

Die approbierte gedruckte Originalversion dieser Dissertation ist an der TU Wien Bibliothek verfügbar.  
 The approved original version of this doctoral thesis is available in print at TU Wien Bibliothek.

# List of Figures

## Chapter 2.1

**Figure 1.** Quantification of cell viability of ASC/TERT1 cells 24 h after treatment with 2PIs DAS and P2CK.

**Figure 2.** Quantification of DNA content of ASC/TERT1 cells treated with DAS.

**Figure 3.** 2PP processing of 7.5% Gel-NB hydrogels.

**Figure 4.** Survival and proliferation of ASC/TERT1 cells in 2PP-produced GelMOD hydrogel constructs.

## Chapter 2.2

**Figure 5.** MC3T3 cells treated with different concentrations of ascorbic acid.

**Figure 6.** MC3T3 cells treated with different concentrations of ascorbic acid (UV).

**Figure 7.** MC3T3 cells treated with different concentrations of Trolox.

**Figure 8.** MC3T3 cells treated with different concentrations of Trolox (UV).

**Figure 9.** GSH pre-treatment of MG63 cells.

**Figure 10.** NAC pre-treatment of MG63 cells.

**Figure 11.** Combination treatment of MG63 cells with different concentrations GSH and NAC.

**Figure 12.** ASC/TERT1 cells treated with different concentrations of GA.

**Figure 13.** ASC/TERT1 cells treated with different concentrations of GA followed by UV treatment.

**Figure 14.** ASC/TERT1 cells treated with different concentrations of CAT.

**Figure 15.** MG63 cells treated with different concentrations of CAT.

**Figure 16.** Cubes produced using 10% GelMOD-97 supplemented with 1 mM P2CK with additional 5  $\mu$ M CAT

**Figure 17.** MG63 cells treated with different concentrations of DTT and ETTMP.

**Figure 18.** MG63 cells treated with different concentrations of DTT and ETTMP followed by 10 min UV irradiation.

**Figure 19.** MG63 cells treated with different concentrations of MDEA and TEA.

**Figure 20.** 100x100  $\mu\text{m}$  cubes printed with or without 10 mM DTT

**Figure 21.** Structuring with TEA and MDEA and co-initiators.

### **Chapter 2.3**

**Figure 22.** Schematic design of the used 2PP setup.

**Figure 23.** Visualization of the degradation scanner.

**Figure 24.** Characterization of Gel-NB hydrogels.

**Figure 25.** mCherry labelled L929 cells embedded in 7.5% Gel-NB hydrogel cubes.

**Figure 26.** Direct encapsulation of L929 mouse fibroblasts in 7.5% Gel-NB hydrogels.

**Figure 27.** Morphology and migration of embedded cells in a stiffness gradient cube.

**Figure 28.** Cell loading capacity of direct cell encapsulation compared to scaffold seeding.

**Figure 29.** mCherry labelled L929 fibroblast cells embedded in 7.5 wt% GelNB hydrogels.

### **Chapter 3.1**

**Figure 30.** UV encapsulation of RFP-HUVEC and ASC/TERT1 cells in 5% Gel-SH and Gel-NB hydrogels.

**Figure 31.** The accuracy and optimization of HD printing of small channelled structures.

**Figure 34.** The two different chip setups tested for the vascular network formation of RFP-HUVECs.

**Figure 35.** Immunostaining of vascular structures under different culturing conditions.

### **Chapter 3.2**

**Figure 36.** GBM-on-chip.

**Figure 37.** Microfluidic chamber design.



**Figure 38.** Degradation of 3D printed membrane using 1 CDU mL<sup>-1</sup> collagenase.

**Figure 39.** Viability of human primary pericytes after encapsulation.

**Figure 40.** Seeding of cells on the membrane.

**Figure 41.** Permeability of the 80  $\mu$ M membrane to different sized molecules.

**Figure 42.** Diffusion of different sized molecules through the BBB construct.

**Figure 43.** Diffusion of different sized molecules (70 kDa and 4 kDa FITC-dextran, fluorescein and FITC-albumin) across the membrane in the presence and absence of cells.

**Figure 44.** The transport of riboflavin across the BBB in presence of HUVECs and 50B11 cells at different time points.

**Figure 45.** Immunostaining of hCMEC cells after 2 and 5 days.

**Figure 46.** Live-dead staining of UV encapsulated of U-87 spheroids.

**Figure 47.** Proliferation of U-87 cells treated with TMZ, RV and the combination of both in 2D, 3D and GBM-on-chip calculated.

**Figure 48.** Caspase and Ki-67 staining of the treated U.87 spheroids using three different setups.

### **Chapter 3.3**

**Figure 49.** Molecular structures of the investigated two-photon photosensitizers (TPE-PS) and reference compound cisplatin.

**Figure 50.** Calibration of cell numbers for the Presto Blue assay using the 384-well glass bottom plate.

**Figure 51.** One-photon and two-photon absorption spectra of the investigated compounds.

**Figure 52.** Concentration dependence of  $q_0$  value to the concentration of TPP.

**Figure 53.** Dark toxicity of investigated PS.

**Figure 54.** Accumulation of PS in the cells.

**Figure 55.** Phototoxicity of PS.

**Figure 56.** Cell viability before and after irradiation with different wavelengths (720 nm, 850 nm and 960 nm).

**Figure 57.** TPE-PDT treatment of mCherry MG63 spheroids surrounded with ASC-GFP single cells.

**Figure 58.** Cell viability after treatment with 30  $\mu$ M cisplatin.

#### **Chapter 4.4**

**Figure 59.** Methacrylated glass and plasma treatment samples showing the distribution of the antibodies.

**Figure 60.** CAD picture of the designed microplates.

**Figure 61.** LSM pictures of the microplates visualized by the absorption of the antibodies.

**Figure 62.** Jurkat cells seeded in the microplate.

**Figure 63.** Number of individual Jurkat cells/microwell.

**Figure 64.** Calcium Imaging of samples.

**Figure 65.** MitoBeacon staining of mitochondria in Jurkat cells.

# List of Tables

**Table 1.** FWHM for x and z (beam propagation)-direction of the IPSF<sup>2</sup> at different depths in the bioink.

**Table 2.** Average powers, peak intensities, intensities at FWHM<sub>z</sub> and threshold layer spacings at different power settings.

**Table 3.** Full width half maximum (FWHM) and the resulting volume of the voxel for the different objectives.

**Table 4.** OrmoComp parameters obtained from the manufacturer`s website.

# Abbreviations

2D	Two-dimensional
2PA	Two-Photon absorption
2PI	Two-photon photoinitiator
2PP	Two-photon polymerization
3D	Three-dimensional
<b><u>A</u></b>	
AFM	Atomic force microscopy
AMT	Additive manufacturing technologies
APC	Antigen presenting cells
ASC/TERT1	Adipose derived stem cells
<b><u>B</u></b>	
BBB	Blood-brain barrier
BdECM	Brain decellularized ECM
<b><u>C</u></b>	
CAD	Computer aided design
CAT	Catalase
CNS	Central nervous system
<b><u>D</u></b>	
DAPI	4',6-diamidino-2-phenylindole
DAS	4,4'-(1,2-ethenediyl)bis[2-(3 sulfophenyl)diazenesulfonate]
DMEM	Dulbecco's modified eagle medium
DS	Degree of substitution
DS	Degree of substitution
DTT	Dithiothreitol
<b><u>E</u></b>	
ECM	Extracellular matrix
EDTA	Ethylenediaminetetraacetic acid
EGM-2	Endothelial cell growth medium-2
ETTMP	Ethoxylated-trimethylolpropane tri-3-mercaptopropionate
EMEM	Eagle's minimum essential media

**F**

FBS	Fetal bovine serum
FRET	Förster resonance energy transfer microscopy
fs	Femtosecond or $10^{-15}$ seconds
FWHM	Full width half maxima

**G**

GA	Gallic acid
GBM	Glioblastoma multiforme
GBM	Glioblastoma
GelMOD	Methacrylamide modified gelatin
Gel-NB	Gelatin-norbornene
Gel-SH	Thiolated gelatin
GM	Goeppert-Mayer Unit or $10^{-50}$ cm <sup>4</sup> s photon <sup>-1</sup>
GSH	Glutathione

**H**

HA	Hyaluronic acid
hBMVEC	Human brain-derived microvascular endothelial cells
hCMEC/D3	Human brain endothelial cells
HD	High definition
hiPSCs	Human induced pluripotent stem cells
hMSCs	Human mesenchymal stem cells
HUVEC	Human umbilical vein endothelial cells

**I**

ISPF	Illumination point spread function
------	------------------------------------

**L**

L929	Murine fibroblast cells
Li-TPO-L	Lithium phenyl-2,4,6-trimethylbenzoylphosphinate
LSM	Laser scanning confocal microscope

**M**

MC3T3	Murine osteoblast cells
MDEA	Methyldiethanolamine
MG63	Human bone osteosarcoma cells

**N**

NA	Numerical aperture
NAC	N-acetylcysteine
NIR	Near infrared
NVU	NeuroVascular Unit

**P**

P2CK	Benzyldiene cycloketone-based two-photon photoinitiator
PBS	Phosphate buffered saline
PBS-BSA	Bovine serum albumin dissolved in phosphate buffered saline
PEG	Polyethylene glycol
PI	Photoinitiator
pMHC	Major histocompatibility complexes
PS	Photosensitizer
PSF	Point spread function

**R**

RBEC	Rat brain capillary endothelial cells
RFP-HUVEC	Red fluorescent protein labelled human umbilical vein endothelial cells
ROS	Reactive oxygen species
RV	Roscovitine

**S**

SMAC	Supra-molecular activation complexes
------	--------------------------------------

**T**

TCRs	T-cell antigen receptors
TEA	Triethanolamine
TEER	Trans-endothelial electrical resistance
TMZ	Temozolomide
TPE-PDT	Two-photon excited photodynamic therapy
TPE-PS	Two-photon excitation photosensitizer
TPP	Porphyrin

**U**

U-87	Human glioblastoma cell line
------	------------------------------

UV

Ultraviolet

V

VE-Cadherin

Vascular endothelial cadherin

Z

ZO-1

Zona occludin-1

$\sigma_{2PA}$

Two photon absorption cross section

# 1 Introduction

The chapter “Introduction” is based on and contains text from Marshall Plan Foundation Grant Report titled “3D Printed Blood-Brain Barrier-on-a-Chip”.



The overall probability of success of any drug entering clinical trials ranges between 3.4% and 33.4% with the lowest success rate presented in oncology drug development.<sup>1</sup> Although animals have been used as primary models for preclinical studies, there is growing evidence that their use in drug development is often hindered due to their limitation to imitate human conditions efficiently.<sup>2,3</sup> Furthermore, due to ethical concerns, the 3R principle as in to reduce, replace and refine animal testing to provide a more humane research environment has been introduced in the last few decades encouraging researchers to reach out towards other alternatives.<sup>4</sup>

Traditionally *in vitro* research has been performed using two-dimensional (2D) planar cell culture. However, recent studies showed that culturing cells in 2D often fails to recapitulate the complexity of the physiological conditions.<sup>5-7</sup> Additionally, using 2D cell culture models for drug testing often results in increased drug response compared the three-dimensional (3D) cell culture which could lead to an overestimation of the efficiency.<sup>8,9</sup> Multiple different ways have been introduced to create 3D cell culture. The two main approaches are often being referred to as bottom up and top down tissue engineering. Bottom up tissue engineering employs the capacity of the cells to self-assemble into aggregates (spheroids) without any mechanical support using non-adhesive (agarose or coated) plates or hanging drop cultures, etc. Top down tissue engineering is based on the use of scaffolds to provide mechanical support and architecture for the cells.<sup>10-17</sup>

Additive manufacturing technologies (AMTs) and bioprinting are emerging new technologies that could provide a useful tool to create complex 3D tissue architectures in a controllable manner.<sup>18-20</sup> In traditional extrusion based bioprinting the 3D structure is created by the layer by layer deposition of materials onto a substrate. Cells can be incorporated into a biocompatible bioink formulation and can be deposited via extrusion, inkjet or laser-assisted strategies.<sup>21-24</sup> While this approach can provide high initial cell numbers and control over spatial distribution of cells, shear stress could compromise cell viability and the resolution which could be achieved is limited.<sup>25,26</sup> Stereolithography employs light of a certain wavelength ( ultraviolet (UV) light) to cure a photosensitive resin according to a computer assisted design (CAD) layer by layer by moving a motorized stage.<sup>27,28</sup> Two-photon polymerization (2PP) is a high-definition (HD) bioprinting method, based on the nonlinear absorption of a tightly focused, femtosecond (fs) near infrared (NIR) laser pulse into photosensitive materials to induce

crosslinking of the material within the focal volume with feature sizes from less than 100 nm.<sup>29–33</sup> Structures can be directly printed within the bulk of the material according to a CAD.

Several different materials can be employed as bioinks for 2PP and other AMTs including natural and synthetic polymers.<sup>34–36</sup> In general, synthetic polymers have a wide medical applications range, such as implants and intraocular lenses among many others.<sup>37,38</sup> Some of the main advantages of such materials are that they exhibit high reproducibility between batches and the chemical composition of them can be easily modified to introduce new functionalities and material properties. However, the disadvantages of synthetic materials include they often lack of cell-responsive moieties and biodegradation, and they could be cytotoxic.<sup>38</sup> Natural polymers often perform better in terms of biocompatibility and biodegradability, but they often lack control over mechanical properties and they could trigger immune responses in some cases.<sup>39</sup> The non-cellular component of all tissues is the extracellular matrix (ECM), which provides not only the necessary biological cues needed for cell signalling, tissue development, differentiation, proliferation, and migration but also the desired mechanical support including elasticity, tensile and compressive strength.<sup>40,41</sup>

Hydrogels are polymer networks which are capable of up taking large quantities of water. The crosslinking of hydrogels can occur through a variety of mechanisms to form either a physically or chemically crosslinked hydrogel.<sup>42–44</sup> During physical (reversible) crosslinking the polymer is formed by secondary forces such as hydrogen-, or ionic bonds, hydrophilic or hydrophobic forces,  $\pi$ - $\pi$  stacking, or entanglements. One of the main advantages of these hydrogels is that they can be formed without any crosslinking additives which are often cytotoxic. On the other hand chemically crosslinked hydrogels are stabilized by covalent bonds. The chemical crosslinking of the polymer could be driven by free radicals, enzymes, Diels-Alder click reaction, Michael type addition and Schiff base formation among others.<sup>45</sup>

Photopolymerization is driven by different reactive species (radicals, cations or anions).<sup>46</sup> Photoinitiators (PIs) are substances which generate reactive species upon irradiation. Based on their mechanism of action they can be either type I or type II. The type I initiators cleave to produce two radicals upon irradiation, while type II initiators undergo a bimolecular process in which the first step is abstract an electron or

hydrogen atom from a second molecule (co-initiator) and in turn this molecule then reacts to initiate polymerization.<sup>47-51</sup> There are several biocompatible PIs such as Irgacure 2959 and lithium phenyl-2,4,6-trimethylbenzoylphosphinate (Li-TPO-L). These PIs have a good absorption in the UV region (250-370 nm), however they often have poor performance in two-photon setting. There are a few water soluble two-photon PIs (2PIs) reported in literature, however only a very few of them presented as biocompatible for biological applications.<sup>52,53</sup> Once the polymerization process is initiated by the PI, the polymer network formation can occur either via chain-growth or step growth mechanism. In chain growth polymerization, the process is introduced by an initiation step followed by a propagation period where the monomer only reacts at the end of the growing polymer chain, and the monomer concentration is decreasing throughout the reaction, and finally a chain termination occurs. One of the most well-known chain growth polymers used in tissue engineering approaches is gelatin-methacrylamide (GelMOD).<sup>54,55</sup> Traditional photopolymerization of polymers with (meth)acrylate functionalities have been largely employed in medical and biological applications.<sup>56</sup> GelMOD hydrogels are an inexpensive, biocompatible platforms for 3D cell culture applications, where the mechanical properties of the material can be fine-tuned by changing the polymer concentration.<sup>54</sup> In step-growth polymerization the monomers first form dimers, then trimers, longer oligomers and ultimately long chain polymers. Thiol-ene click reaction is based on the orthogonal reaction of thiols with carbon-carbon double bonds.<sup>57,58</sup> The network formation proceeds by repeated addition of thiyl radicals to double bonds and chain transfer reactions by hydrogen abstraction.<sup>59</sup>

## 2 Bioinks and Biocompatible Two-Photon Initiators

### 2.1 A biocompatible diazosulfonate initiator for direct encapsulation of human stem cells via two-photon polymerization

This chapter is published and contains text from the following publications

Tromayer M\*, Dobos A\*, Gruber P, Ajami A, Dedic R, Ovsianikov A and Liska R **2018** A biocompatible diazosulfonate initiator for direct encapsulation of human stem cells via two-photon polymerization *Polym. Chem.* 9 3108–17 with permission from Royal Society of Chemistry.

DOI: 10.1039/c8py00278a

\* equal contribution

And

Dobos A, Van Hoorick J, Steiger W, Gruber P, Markovic M, Andriotis O G, Rohatschek A, Dubruel P, Thurner P J, Van Vlierberghe S, Baudis S and Ovsianikov A **2019** Thiol–Gelatin–Norbornene Bioink for Laser-Based High-Definition Bioprinting *Adv. Healthc. Mater.* 1900752

DOI:10.1002/adhm.201900752

The synthesis of the photoinitiator DAS was carried out by M. Tromayer (TU Wien).

### 2.1.1 Introduction

3D cell encapsulation is a powerful tool for tissue engineering, not only offering the benefits of cellular environments mimicking physiological tissues closer than classical 2D culture models, but also being advantageous to the general approach of seeding cells on porous prefabricated scaffolds.<sup>6,60,61</sup> Compared to the latter method, direct encapsulation within the scaffold is a desirable alternative providing high initial cell loading, uniform cell distribution and more intimate cell–matrix contact.<sup>62</sup> Furthermore, the concomitant presence of cells during scaffold fabrication allows for high throughput, streamlining the process towards automated tissue fabrication.<sup>27</sup>

2PP has been employed using rose bengal as photosensitizer to fabricate micropillars from bovine serum albumin as artificial stem cell niches, as well as cross-linking cytoplasmic proteins inside live starfish oocytes to create barriers and channels isolating different intracellular regions, with the aim of conducting functional studies.<sup>63,64</sup> Direct 3D encapsulation of polymicrobial bacterial communities *via* 2PP has also been achieved.<sup>65</sup> However, there is still a lack of studies demonstrating more sensitive cell types kept viable after successful 2PP encapsulation. This is in part due to the limitations associated with currently available photosensitizers and photoinitiators (PIs) used to start the covalent cross-linking processes, such as free radical polymerization.

Classical UV-encapsulation of cells has made use of commercial PIs such as Irgacure 2959, VA-086 and Li-TPO-L, which generate initiating radicals by homolytic bond cleavage upon photoexcitation.<sup>62,66–68</sup> Due to their relatively small conjugated  $\pi$ -systems, classical PIs generally have low two photon absorption cross section ( $\sigma_{2PA}$ ) and tend to suffer from poor performance and low achievable writing speeds in 2PP.<sup>69,70</sup> Thus, specialized water-soluble 2PIs such as the benzylidene cycloketone-based 2PI P2CK have been developed and proved highly efficient in the microfabrication of 3D hydrogel structures.<sup>71</sup> Nonetheless, these 2PI systems exhibit significant cytotoxicity above certain concentrations and can cause extensive photodamage to cells after laser irradiation.<sup>72</sup> Since aforementioned cleavable commercial PIs have shown good cytocompatibility in UV-encapsulation of cells, we hypothesize that generation of polymerization initiating radicals by rapid, unimolecular

2PI cleavage could help minimize unwanted side-processes associated with bimolecular initiation mechanisms of conventional 2PIs during long lived triplet state.

Aryl diazosulfones cleave under formation of phenyl- and sulfonyl-based radicals as well as molecular nitrogen, and have been used for thermally induced free radical polymerization.<sup>73</sup> Their use in 2PP has not been previously reported in literature, but they exhibit strong absorption in the visible range that was suspected to also be excited by two-photon absorption (2PA) at 800 nm.

### 2.1.2 Aim

The objective of the present study was to develop a water-soluble, cleavable aryl diazosulfonate 2PI tetrapotassium 4,4'-(1,2-ethenediyl)bis[2-(3 sulfophenyl)diazene-sulfonate] (DAS) with excellent cytocompatibility, transcending the limitations of state-of-the-art materials. The 2PP structuring threshold and swelling behaviour of cross-linked hydrogel structures were analyzed. 2D and 3D *in vitro* biocompatibility was evaluated by using immortalized adipose-derived stem cells (ASC/TERT1) in cell viability assays both in the absence of light and after direct cell encapsulation via 2PP.

### 2.1.3 Experimental

#### 2.1.3.1 *Mode of practice for photosensitive compounds*

The preparation and analysis of the photosensitive compounds and formulations was conducted in an orange light lab. The windows and fluorescent lamps were covered with foil filters or filter coatings so that light with a wavelength <520 nm was cut off.

#### 2.1.3.2 *ASC/TERT1 cell culture*

ASC/TERT1 (Evercyte, Vienna, Austria) were cultured and maintained in Endothelial Cell Growth Medium-2 EGM-2 media (Lonza, Basel, Switzerland) supplemented with foetal bovine serum (FBS) to a final concentration of 10%. Cells were incubated in a humidified atmosphere with 5% CO<sub>2</sub> at 37°C. At 80% confluence the cells were detached using 0.5% trypsin-EDTA solution (Gibco, Waltham, MA, USA) and after the cells detached trypsin inhibitor was added (Gibco, Waltham, MA, USA), the cells were

resuspended in media and centrifuged at 170 g for 5 min before seeding onto T75 flasks.

### 2.1.3.3      *Cell viability*

Cell viability was measured using PrestoBlue Assay (Invitrogen, Carlsbad, CA, USA). Briefly, cells were seeded in 96-well culture plates. 0.5-4 mM DAS and P2CK solution in EGM-2 (10% FBS) media was added to the wells (followed by a 10 min UV irradiation on one plate) and the plates were incubated for 3 h at 37 °C. Afterwards the cells were washed with Dulbecco's Phosphate Buffered Saline PBS (Sigma-Aldrich, Saint Louis, MO, USA) twice before fresh media was added and the cells were left to recover overnight. After 24 h PrestoBlue assay was performed, by diluting the reagent 1:10 with EGM-2 media and the plates were incubated for 1 h. The absorbance was measured in a plate reader (Synergy H1, BioTeck) at an excitation wavelength of 560 nm and the emission was recorded at 590 nm. Data were analyzed with GraphPad Prism software using one-way ANOVA with Kruskal–Wallis test followed by Dunn's multiple comparisons post-hoc.

### 2.1.3.4      *DNA Quantification*

FlouReporter Blue Fluorometric dsDNA Quantitation Kit (Thermo-Fisher, Waltham, MA, USA) was used to measure the DNA content of the samples after treatment with the photoinitiators. The plates on which PrestoBlue assay was applied were frozen for 5 days at -80°C and Hoechst assay was performed following the instructions of the manufacturer. Briefly, the plates were thawed at room temperature and 100 µL distilled water was added and the plates were incubated at 37°C for 1 h. Afterwards, Hoechst 33258 staining was diluted to 1:400 with TNA buffer (10 mM Tris, 2 M NaCl, 1 mM EDTA, 2 mM sodium azide), 100 µL of the reagent was added to the wells and the fluorescence was measured using excitation and emission filters at 369 nm and 460 nm, respectively.



#### 2.1.3.5      *2PP setup*

For 2PP structuring, a femtosecond NIR-laser (MaiTai eHP DeepSee, Spectra-Physics) was used at 800 nm, with a repetition rate of 80 MHz and a pulse duration of 70 fs after the microscope objective (Plan-Apochromat 10x/0.3, Zeiss). The peak intensity for these parameters at 1 mW average power is 7 GW/cm<sup>2</sup> in the focal plane of the objective and the spectral width of the used laser system at 800 nm is 9.6 nm. To facilitate high-speed structuring a combination of sample positioning via a motorized stage and a galvo-scanner was used for laser beam positioning within the sample. The in-house developed software controls the complete setup. The structuring process was monitored in real time with a CMOS-camera mounted behind the dichroic mirror in the beam path.

#### 2.1.3.6      *Methacrylation of glass surfaces*

To ensure proper attachment of the 3D printed hydrogel structures to the substrate, the glass surfaces were modified with methacrylate functionalities following a silanization procedure using 3-(trimethoxysilyl)propyl methacrylate prior to the structuring. All structures were printed in glass bottom dishes (IBIDI 35 mm diameter with glass bottom, high version, Ividi GmbH, Martinsried, Germany). The glass surfaces were plasma treated (Harrick plasma, Ithaca, USA) for 10 min prior to the addition of the methacrylation solution (49.9 % deionized water, 47.9 % ethanol, 0.3 % acetic acid, and 1.9 % of 3-(trimethoxysilyl)propyl-methacrylate) for 45 min. Afterwards, the glass dishes were washed with deionized water and dried at room temperature.

#### 2.1.3.7      *Structuring Threshold*

In order to evaluate the structuring threshold of the hydrogels, 10% gelatin methacrylamide hydrogel (GelMOD) with a substitution rate of 95%, (provided by Ghent University) was dissolved in EGM-2 media supplemented with 1 mM or 2 mM P2CK or DAS. Cubes with a side length of 100 μm were printed on methacrylated glass using the previously mentioned 2PP setup, with different writing speeds (100-1000 mm·s<sup>-1</sup>), different powers (45-100 mW), and hatching with 0.5 μm line and 0.5 μm layer spacing. The threshold was defined as the minimal power needed for stable structures.



### 2.1.3.8 Swelling

The swelling ratio of samples (10% GelMOD with 1 mM P2CK or 2 mM DAS) was addressed by measuring the changes in perimeter of the samples using ImageJ FIJI software. 100  $\mu\text{m}$  cubes were printed using parameters above the structuring threshold. The printed structures were immersed in PBS for 48 h until they reached the swelling equilibrium. The swelling ratio ( $Q$ ) was calculated using **Equation 1**:

$$Q = \frac{P_t - P_b}{P_b} * 100 \quad (1)$$

where,  $P_t$  is the perimeter of the cubes on the top,  $P_b$  is the perimeter of the sample on the bottom.

### 2.1.3.9 Cell encapsulation

ASC/TERT1 cells were trypsinized and resuspended in 10% GelMOD solution supplemented with either 1 mM P2CK or 2 mM DAS at a concentration of  $2 \times 10^6$  cells/mL. The cell-containing hydrogel precursor solution was applied to methacrylated  $\mu$ -dishes (35 mm diameter with glass bottom, high version, Ibidi GmbH, Martinsried, Germany). The structures were printed with the above mentioned 2PP setup, using 0.5  $\mu\text{m}$  line and 0.5  $\mu\text{m}$  layer spacing. In order to assess the changes in cell numbers, larger cubes of 300  $\mu\text{m}$  sides were printed, using 1000  $\text{mm} \cdot \text{s}^{-1}$  writing speed. For demonstration TU logos were printed with a writing speed of 250  $\text{mm} \cdot \text{s}^{-1}$ . The viability of cells was assessed with Calcein AM/Propidium iodide staining (Sigma-Aldrich, St. Luis, USA). The samples were incubated for 20 min before the images were captured by confocal laser scanning microscope (LSM700 Zeiss, Germany).

## 2.1.4 Results and Discussion

The 2PA cross section of DAS is around 40 Goeppert-Mayer Unit (GM) at the 2PP structuring wavelength used (800 nm), while P2CK has a more than three times higher cross section of about 140 GM.<sup>53</sup> However, the resulting lower 2PP structuring efficiency of DAS can be sufficiently compensated by using a concentration of 2 mM, versus 1 mM for P2CK, to obtain good 2PP processing results.

PrestoBlue mitochondrial activity assay was used to address the viability of ASC/TERT1 in 2D. PrestoBlue reagent is a resazurin-based, cell-permeant solution that uses the reducing power of mitochondrial enzymes of living cells to quantitatively measure proliferation.<sup>74</sup> 24 h after stimulation with different concentrations of 2PIs the cells exhibited normal metabolic activity in case of DAS, while P2CK treatment led to significant decrease of cell viability above 0.5 mM (**Figure 1a**). These results were in accordance with DNA quantification using Hoechst 33258 staining, a dye that stains double stranded DNA, and therefore corresponds to the actual cell number of the sample and it showed no statistical significance between the treated samples compared to the control (**Figure 2a**).<sup>75</sup> The drawback of this method is that partial precipitation of P2CK in the samples interferes with the measurement of fluorescence intensity at the required wavelengths leading to unreliable results. Therefore, this method of DNA quantification could only be used for the DAS samples. In a further experiment, a plate containing 2PIs was irradiated at 365 nm in order to mimic the photoinitiation process. The UV irradiation resulted in significantly lower survival of cells, however even at 3 mM and 4 mM DAS samples the cell survival reached 60% compared to the untreated control (**Figure 1b**). The DNA quantification also corresponded with the experienced results shown in (**Figure 2b**). On the other hand, these conditions led to cell death in all samples treated with any concentrations of P2CK (not plotted).

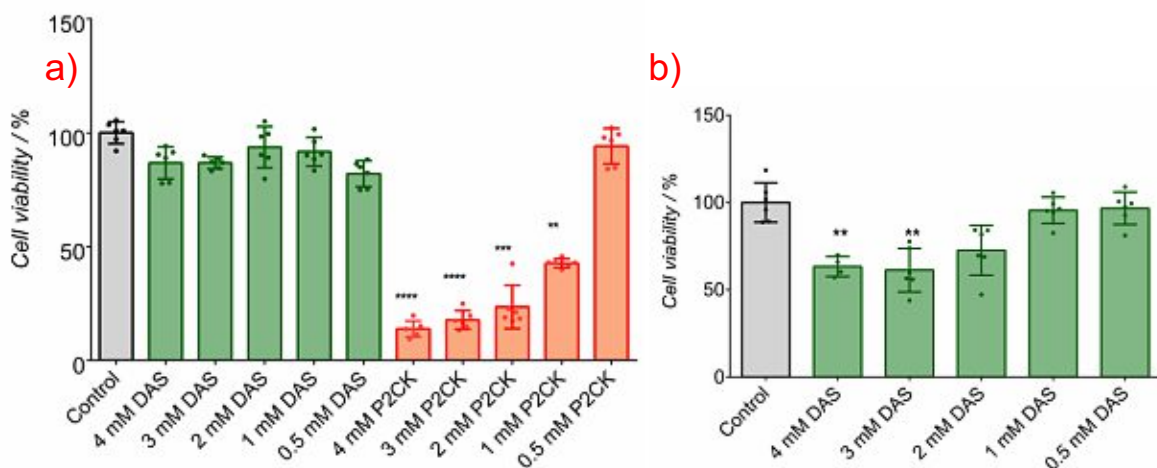


**Figure 1. Quantification of cell viability of ASC/TERT1 cells 24 h after treatment with 2PIs DAS and P2CK.** Presto blue assay was used to evaluate the metabolic activity of the cells. (a) DAS was well tolerated in the analyzed range (0.5-4 mM), while all concentrations of P2CK above 0.5 mM affected cell viability significantly. (b) When the cells were irradiated with UV to model the initiation of the 2PIs, cell viability was maintained up to 2 mM DAS concentration. The statistical significance was addressed by ANOVA with Kruskal–Wallis test followed by Dunn’s multiple comparisons test. n = 6; \*\*p < 0.01; \*\*\*p < 0.001 ; \*\*\*\* p < 0.0001

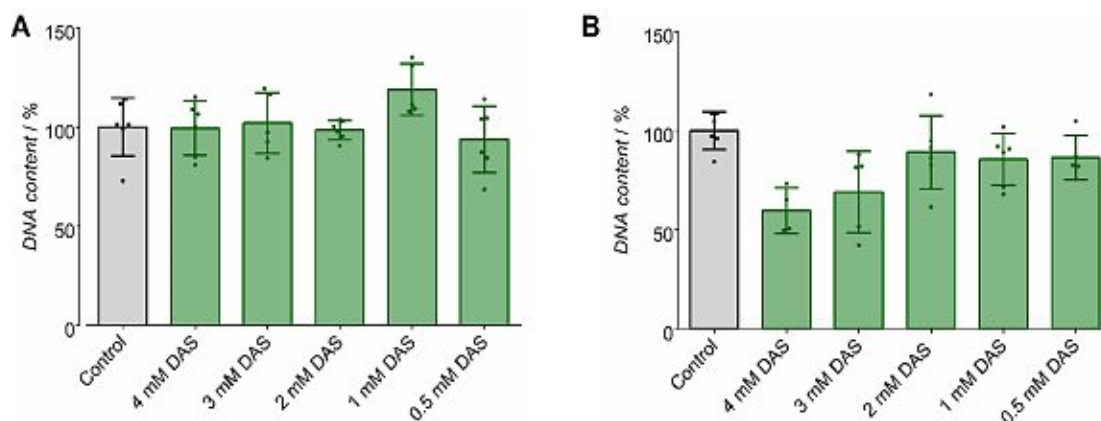


**Figure 2. Quantification of DNA content.** The drawback of this method is that partial precipitation of P2CK in the samples interfere with the measurement of fluorescence intensity at the required wavelengths leading to unreliable results. Therefore, this method of DNA quantification could only be used for the DAS samples (a) DNA content of the samples treated with DAS. (b) DNA content of the samples that were UV treated in order to mimic the activation of DAS.

DAS was tested in 2PP processing and compared to the well-established 2PI P2CK. In order to investigate the laser power threshold for structuring, a 10% GelMOD hydrogel supplemented with 1 mM or 2 mM P2CK and DAS was prepared and 100  $\mu\text{m}$  cubes were printed at 45-100 mW and up to 1  $\text{m}\cdot\text{s}^{-1}$  writing speed. The applied 2PI concentrations were kept as low as possible, while still reaching fabrication threshold at an acceptable laser power. **Figure 3a** shows that although 1 mM P2CK needs an average 15 mW less power at every given writing speed to reach the threshold limit, it is possible to use 2 mM DAS as a suitable alternative to P2CK for 2PP application.

The swelling profile of a hydrogel demonstrates its ability to absorb water, which is related to the crosslinking density of the material, hence the more crosslinked the gel is, the less it swells. It could affect not only the diffusion rate of nutrients and metabolites in the hydrogel, but also the migration and stretching of cells. Besides the 2PI and hydrogel polymer concentrations, the laser power and writing speed affect the number of crosslinks within the gel. In order to study the swelling of the samples, a set of 100  $\mu\text{m}$  cubes were fabricated with different writing speeds and powers, using 10% GelMOD supplemented with either 1 mM P2CK or 2 mM DAS. After the samples reached equilibrium swelling state (approximately after 48 h) their dimensions were recorded.

Both the writing speed and the laser power influenced the swelling behavior of the hydrogels as expected (**Figure 3b**). Increased speed and decreased power led to more

extensive swelling regardless of the 2PI used, and both 2PIs led to similar results under these circumstances. For this reason, 2 mM of DAS can be used as a substitute for 1 mM P2CK to reach the similar cross-linking density of material.

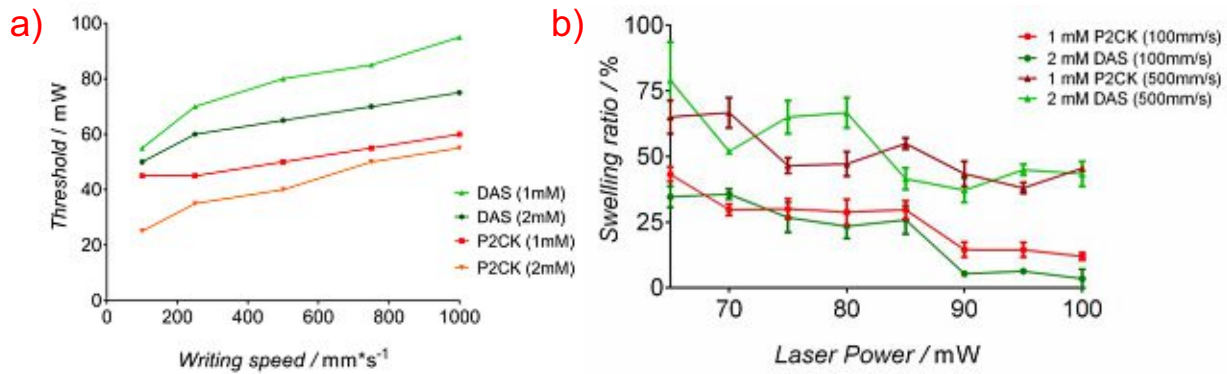


**Figure 3. 2PP processing of hydrogels. (a) Structuring threshold of 2PIs. At all tested writing speeds it was possible to structure in the gels using either 2PI. P2CK (red) required less laser power in comparison to DAS (green). (b) Swelling of hydrogels fabricated at different writing speeds of 100 mm·s<sup>-1</sup> and 500 mm·s<sup>-1</sup>. The swelling was power and speed dependent and comparable in both cases.**

In order to evaluate the biocompatibility of the 2PIs in 2PP processing, ASC/TERT1 cells were encapsulated in 10% GelMOD-95 hydrogel using 1 mM P2CK or 2 mM DAS and followed through the course of 5 days. To facilitate high throughput, relatively high powers (80-110 mW) were chosen to allow a writing speed as fast as 1 m·s<sup>-1</sup>. The cells were stained with Calcein-AM and Propidium Iodide and were automatically counted using ImageJ FIJI software with an automatic object counting. Although the same number of cells were encapsulated in both cases, P2CK samples resulted in average 75% less cell survival on day 1, and led to more decrease over the course of time at laser powers above 80 mW. By using DAS, the proliferation of the cells reached up to 140% after 5 days when laser powers below 100 mW were used. However, at higher powers cell numbers decreased, possibly due to too tightly crosslinked hydrogels which did not support the long-term proliferation of ASC/TER1 cells. The survival of the cells was dose dependent and reached up to 140% relative cell number compared to day 1 when laser powers under 100 mW were used. **(Figure 4a).**

To further demonstrate the capacities of DAS as a biocompatible 2PI, ASC/TERT1 cells were encapsulated in a structure containing not only crosslinked, but also non-polymerized sections **(Figure 4b)**, and were stained on day 1 and day 5, using

CalceinAM/Propidium iodide live/dead staining. In the P2CK samples, the auto-fluorescence of the 2PI makes the visualization of dead cells challenging, however the cells were only proliferating in the void areas (**Figure 4d**). On the other hand in DAS samples no auto-fluorescence was detected, the encapsulated cells were expanding in the gel as well and still responded to the live stain after 5 days (**Figure 4c**).

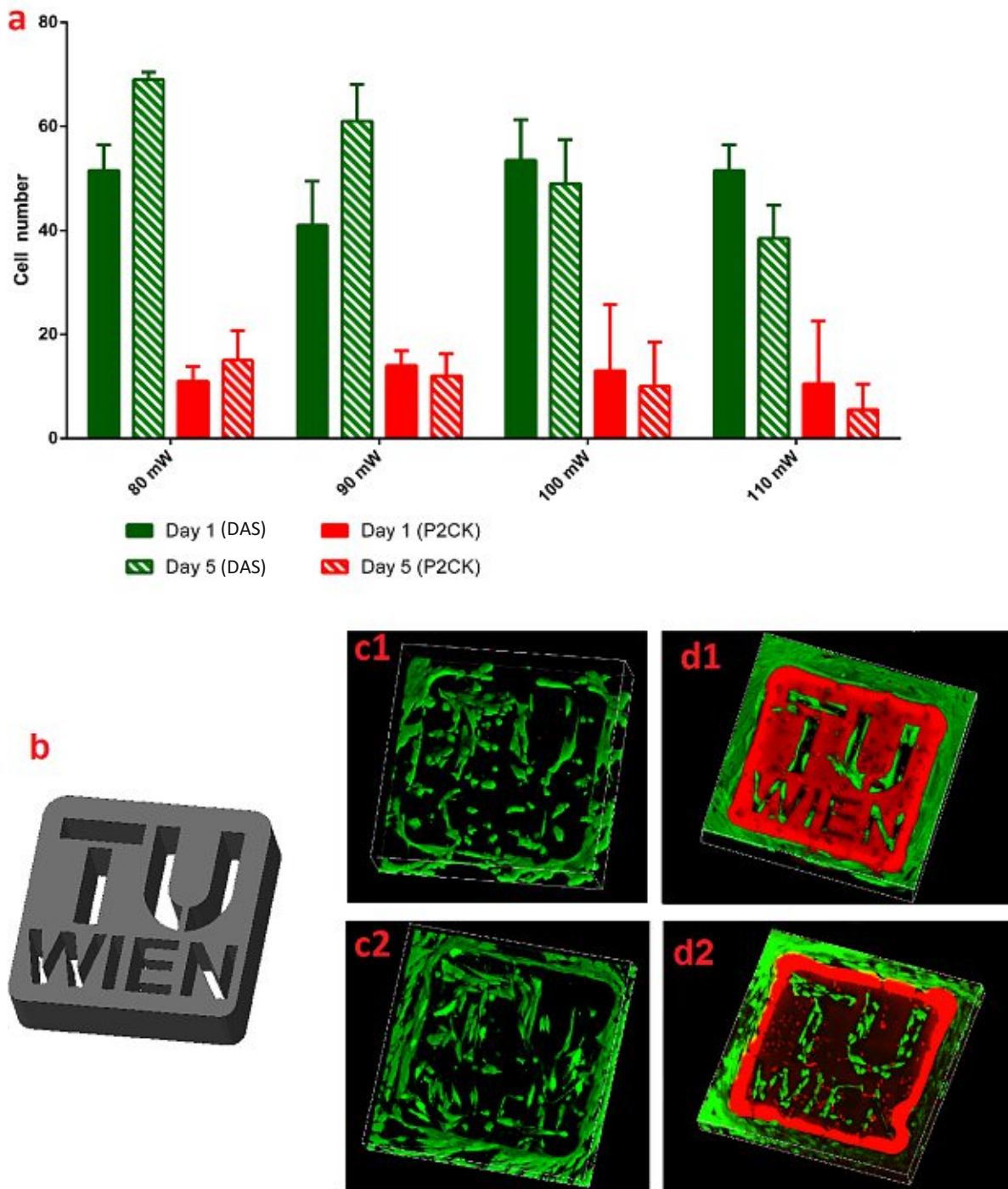


Figure 4. Survival and proliferation of ASC/TERT1 cells in 2PP-produced GeIMOD hydrogel constructs. (a) Number of cells within the 3D printed hydrogel cubes at day 1 and day 5. The



application of DAS as 2PI resulted in higher initial higher cell survival and increased proliferation when compared to P2CK. (b) CAD image of printed TU Wien logos, dimensions 500x500x125  $\mu\text{m}$  (c1) TU Wien logo produced at 80 mW using 2 mM DAS 24 h after 2PP structuring (c2) TU Wien logo structured with 2 mM DAS after 5 days, with high survival and expanded morphology of the cells (d1) TU Wien logo structured with 1 mM P2CK 24h after fabrication (d2) TU Wien logo structured with 1 mM P2CK after 5 days. Cells were only growing in the void, while cells in the gel were not viable after 5 days.

### 2.1.5 Conclusion

A novel water-soluble diazosulfonate two-photon initiator DAS was compared to the well-established initiator P2CK as a reference. Due to its lower two-photon absorption cross-section, DAS had to be used at double concentration of P2CK for 2PP structuring. At this concentration DAS supports exceedingly high writing speeds up to  $1 \text{ m}\cdot\text{s}^{-1}$  and a performance generally similar to P2CK, as indicated by laser power threshold and hydrogel swelling experiments. 2D cell viability assays and 3D cell encapsulation via 2PP using adipose derived stem cells both demonstrated the biocompatibility of DAS far exceeding the reference P2CK and its potential as superior material for cell-based biofabrication.

## 2.2 Alternative Strategies Towards Improving Cell Viability During Encapsulation

Die approbierte gedruckte Originalversion dieser Dissertation ist an der TU Wien Bibliothek verfügbar.  
The approved original version of this doctoral thesis is available in print at TU Wien Bibliothek.

### 2.2.1 Introduction

Directly embedding cells via 2PP is challenging due to several reasons. First, in order to achieve a stable structure, it is necessary to apply the appropriate photoinitiator and polymer concentration and relevant laser powers, although increasing these factors can create a hostile environment for the cells which in turn could lead to poor cell survival. There are several different approaches that could improve cell viability upon direct cell embedding. Some of the approaches, discussed in detail in chapter 2.1 and 2.3, include the use highly biocompatible two-photon photoinitiators and hydrogels, which allow the processing of the bioink under mild conditions. The other approaches that were tested to improve the bioprinting efficacy are antioxidants, enzymes, co-initiators and photosensitizers.

Increased levels of reactive oxygen species (ROS) can induce apoptosis and necrosis in cells, and are thought to be one of the main pathogenic mediators in various diseases.<sup>76–79</sup> By using antioxidants and enzymes, the cells could be protected from harmful ROS, however, their administration could be troublesome as it should not interfere with the reactive species needed primarily for structuring. Several different antioxidants and enzymes were tested. Ascorbic acid (Vitamin-C) and Trolox (soluble analogue of Vitamin E) are two of most well-known water soluble antioxidants that could decrease direct and indirect oxidative stress inside the cells.<sup>80–84</sup> Previous study showed that pre-treatment with N-acetylcysteine (NAC) and reduced glutathione (GSH) prior to the UV encapsulation of MG63 cells could increase both proliferation and viability of the cells compared to the untreated cells.<sup>85</sup> GSH is a small molecular weight thiol molecule in cells and it plays an important role in protecting the cells against ROS and also can act as a substrate to several other antioxidant enzymes.<sup>84,86,87</sup> NAC on the other hand has the ability to act as a precursor of reduced GSH, also in some cases NAC can act as a direct antioxidant for some oxidant species such as NO<sub>2</sub>.<sup>88–90</sup> Gallic acid (GA) is a phenolic compound that can be found in several plants. The treatment of human peripheral blood lymphocytes with 50 μM GA protected the cells from H<sub>2</sub>O<sub>2</sub> induced lipid peroxidation and apoptosis, however when human promyeloid leukaemia cells were treated with 0.3 mM of the same substance the cells underwent apoptosis.<sup>91–93</sup> The down-stream targets of heme oxygenases is bilirubin and biliverdin and they are known to have reducing properties and are recognized as potent antioxidants.<sup>94</sup> Finally, catalase (CAT) is the most commonly used enzyme used



for the decomposition of  $\text{H}_2\text{O}_2$  into water and oxygen, however previous study have shown that CAT could reduce proliferation of cells when non-toxic levels of ROS were present possible due to interfering with signalling cascade which rely on the regulation by  $\text{H}_2\text{O}_2$ .<sup>95–97</sup>

Another approach is to use co-initiators, crosslinkers or photosensitizers to improve the printing process by reducing the needed laser power or by increasing the possible writing speed and essentially increase the efficiency of the process. Co-initiators can be employed in photopolymerization when type II PI are used, as their mechanism of action involves the abstraction of an electron or hydrogen atom from a co-initiator and in turn this molecule is responsible for initiating the polymerization.<sup>98</sup> Crosslinkers can also be introduced to the different hydrogel formulation as their role is to form intermolecular links between the polymer chains. Photosensitizers energy is transferred from light to oxygen by the PS to generate ROS, which later on can be utilized for polymerization but these ROS can cause damage to the cells as well.<sup>99</sup> However, these substances could also have drawbacks as they are often cytotoxic which makes their application limited for cell encapsulation.

## 2.2.2 Aim

The aim of the following experiments was to test several different antioxidants, enzymes, co-initiators and photosensitizers on cell viability and on 2PP output.

## 2.2.3 Experimental

### 2.2.3.1 Cell Viability Assay

The effect of the antioxidants and enzymes were tested using different cell lines including ASC/TER1, L929, MC3T3 and MG63 cells with their corresponding cell culture media (EGM-2 10% FCS for ASC/TERT1, and DMEM high glucose 10% FBS for the rest). For the cell viability assay, 5000 cells per well were seeded in a 96-well plate and were left to adhere overnight. The next day 100  $\mu\text{L}$  substance/well was added in dark for different time points followed by a 10 min UV treatment in the case of light exposed samples. The UV irradiation was introduced approximately after 20 min of adding the substances unless stated otherwise. Afterwards the cells together with substances were placed back to the cell culture incubator for 24 h, unless it was stated otherwise. Finally, Presto Blue Assay was applied for 1 hour according to the

previously described protocol in Chapter 2.1.3.3. The relative fluorescence was measured by plate reader. (excitation: 560 nm, emission: 590 nm). The relative fluorescence of each sample is compared to the mean of relative fluorescence of control samples, ANOVA with Dunnett's multiple comparisons test was performed (\*\*p < 0.01; \*\*\*p < 0.001 ; \*\*\*\* p < 0.0001) The error bar stands for standard deviation (SD).

## 2.2.4 Results and Discussion

### 2.2.4.1 Ascorbic Acid

Several different concentrations of ascorbic acid (0.5-2 mM) were tested in the presence or absence of Li-TPO-L and UV irradiation. The treatment of cells with ascorbic acid above the concentration of 0.5 mM lead to decreased cell survival even in the non-light treated samples. In the presence of the PI Li-TPO-L, the lower concentrations of ascorbic acid showed no significant improvement of cell viability after the addition of the PI, while 1 mM and 2 mM ascorbic acid further decreased the cell viability compared to the PI control (**Figure 5**). All concentrations of ascorbic acid showed improved cell viability upon UV treatment in the samples which did not contain

the PI compared to the only UV treated control, however it did not provide sufficient protection for the cells when 2.23 mM Li-TPO-L was added to the samples (**Figure 6**).

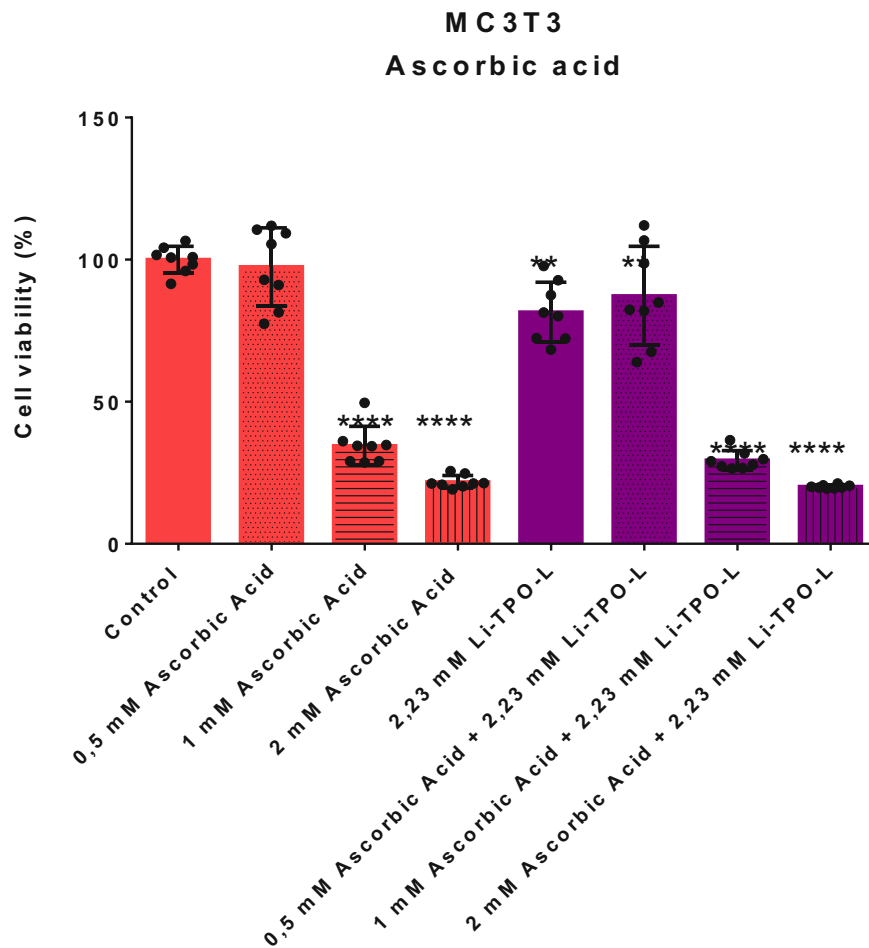


**Figure 5. MC3T3 cells treated with different concentrations of ascorbic acid with or without Li-TPO-L.**

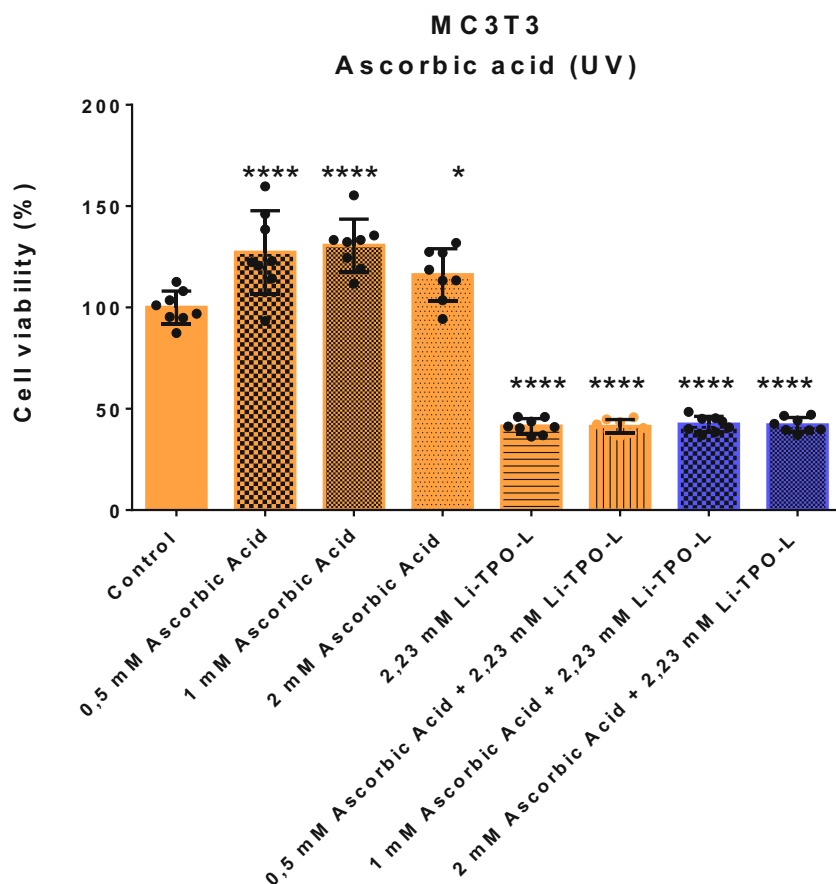


**Figure 6.** MC3T3 cells treated with different concentrations of ascorbic acid with or without Li-TPO-L followed by UV light irradiation for 10 min. The substances were then left for 24 h before PrestoBlue cell viability assay was performed.

#### 2.2.4.2 Trolox

Different concentrations of Trolox were tested using MC3T3 mouse fibroblast cells in the presence of 2.23 mM Li-TPO-L concentration. The treatment time of the antioxidants were 24 h. The cells under normal conditions (not UV treated) showed increased metabolic activity under all measured conditions including the control cells treated only with Li-TPO-L. We hypothesize this could be due hyperactivity of the cells (**Figure 7**). However, all the applied concentrations of Trolox resulted in lower survival than the control when the cells were UV-treated. In the presence of the PI, Trolox did not improve cell viability (**Figure 8**).

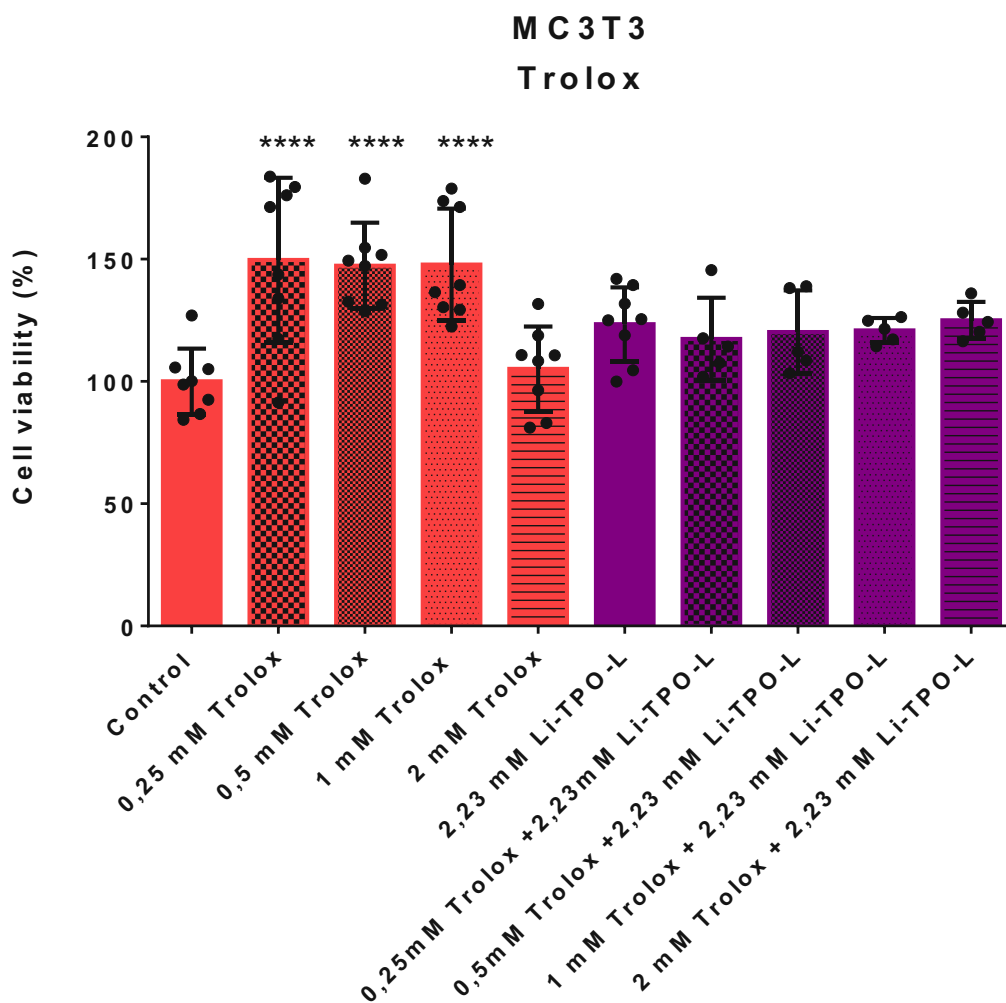


Figure 7. MC3T3 cells treated with different concentrations of Trolox and Li-TPO-L.

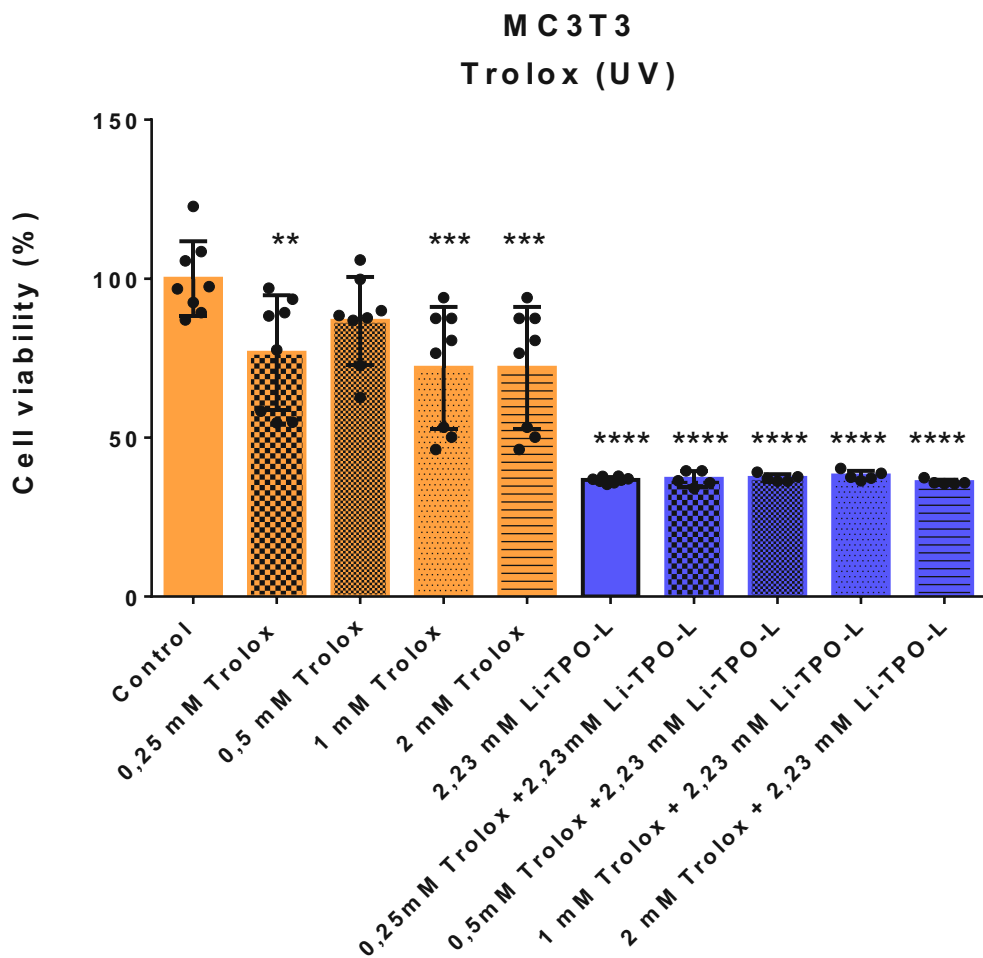


Figure 8. MC3T3 cells treated with different concentrations of Trolox and Li-TPO-L followed by 10 min UV treatment.

### 2.2.4.3 NAC and GSH

Human osteosarcoma cell line MG63 cells were pre-treated with different concentrations of NAC and GSH and the combinations of both for 20 min. Afterwards, the cells were washed and different concentrations of Li-TPO-L were added followed by UV treatment. The pH of the solutions was adjusted to 7.4 by sodium hydroxide. GSH treatment alone decreased cell survival in the samples without PI and did not improve viability of the cells when different concentrations of Li-TPO-L were added (**Figure 9**) and the same trend was visible for NAC (**Figure 10**). The combination treatment showed some improvement compared to the samples treated with the components alone, however it failed to significantly improve the cell viability (**Figure 11**).

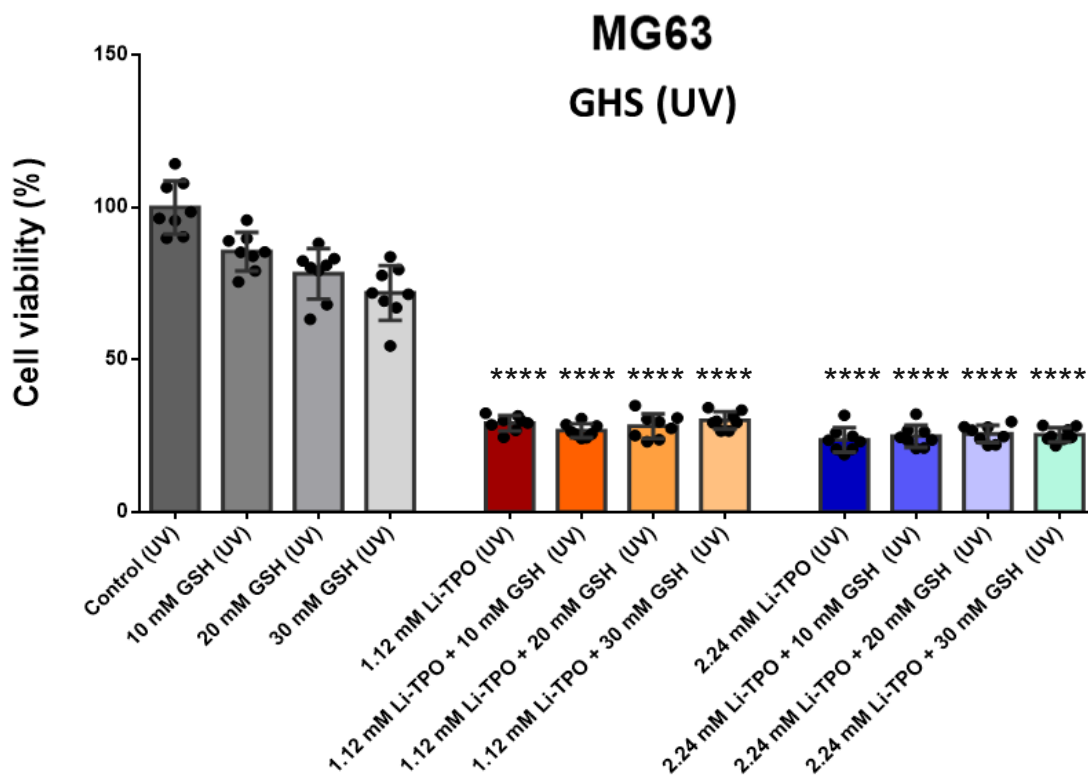


Figure 9. GSH pre-treatment of MG63 cells with different concentrations for 20 min followed by 10 min UV treatment.

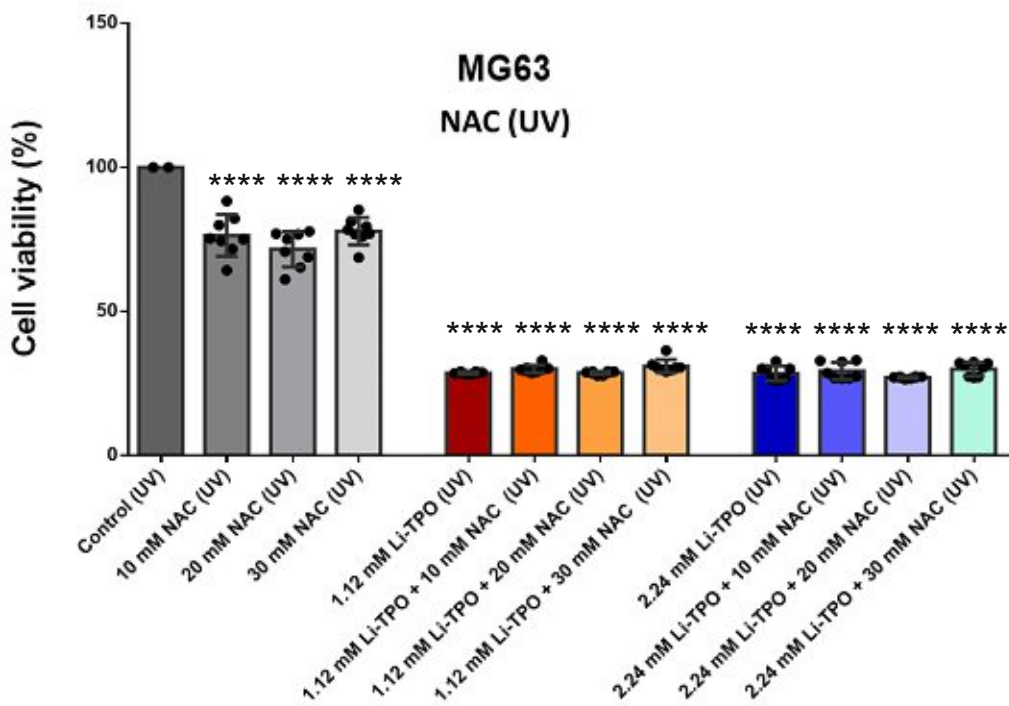


Figure 10. NAC pre-treatment of MG63 cells with different concentrations for 20 min followed by 10 min UV treatment.

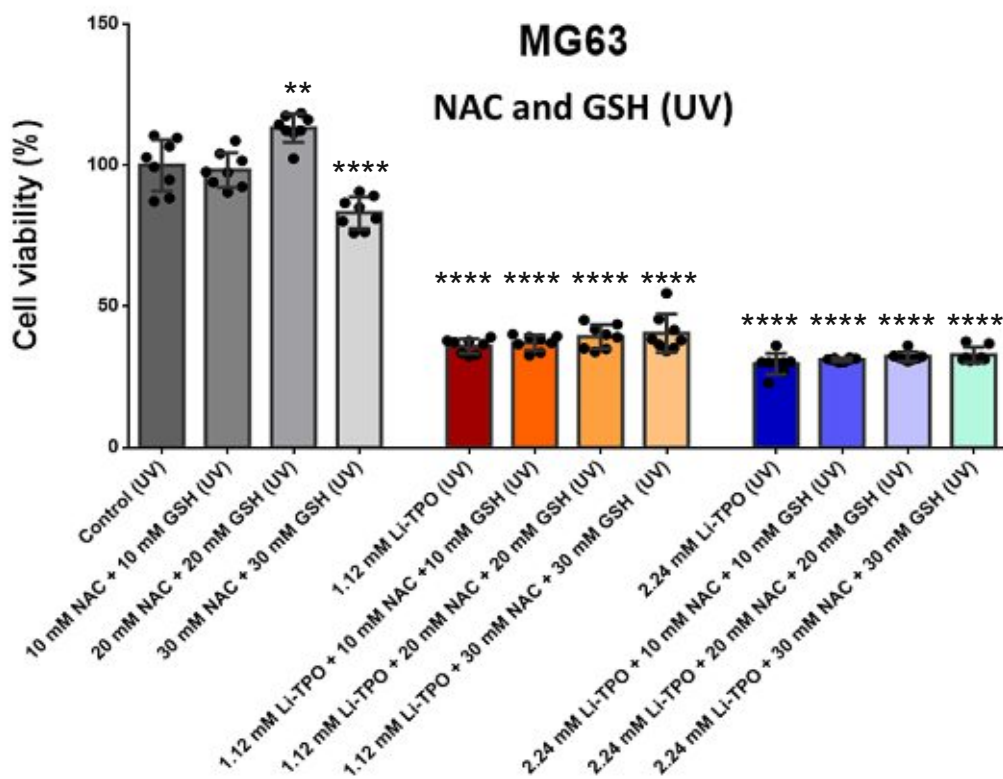


Figure 11. Combination treatment of MG63 cells with different concentrations GSH and NAC for 20 min followed by 10 min UV treatment.



2.2.4.4 Gallic Acid

ASC/TERT1 cells were treated with several different concentrations of GA for 20 min followed by 10 min of UV irradiation on one plate without PI and the substances were removed after 3 h. GA was generally badly tolerated by cells above 1 μM concentration (Figure 12). However, the cells showed increased cell viability in the UV treated samples compared to dark conditions. We hypothesize that this could be due to capturing the ROS generated by the UV irradiation instead of interfering with intercellular ROS required for intercellular signalling and other cell mechanisms (Figure 13).

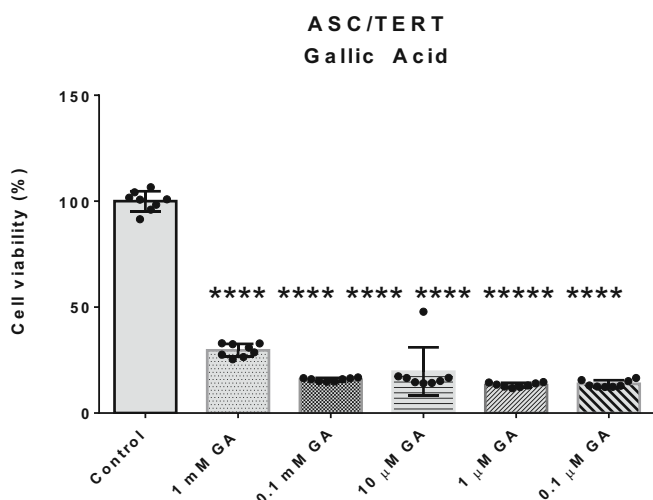


Figure 12. ASC/TERT1 cells treated with different concentrations of GA.

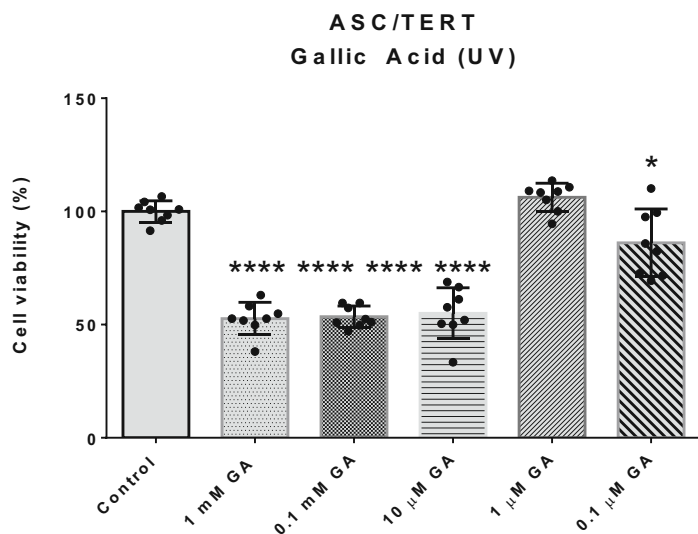


Figure 13. ASC/TERT1 cells treated with different concentrations of GA followed by UV treatment.

#### 2.2.4.5 Catalase

Different concentrations of CAT were tested on both MG63 and ASC/TERT1 cells and were left on the samples for 3 h. CAT significantly improved cell survival in both cases when cells were treated with 1.12 mM Li-TPO-L followed by a UV-treatment after 20 min of addition (**Figure 14** and **Figure 15**), however it failed to significantly improve cell survival when higher concentration of the PI was added. Furthermore, CAT at a concentration of 5 μM was also tested for 2PP in order to evaluate if the enzyme interferes with the radicals employed for the structuring. 100 x 100 x 100 μm cubes were printed using 10% Gel-MOD-97 hydrogel together with 1mM P2CK. The

structures were imaged with bright-field microscopy. The 5  $\mu\text{M}$  CAT did not alter the structuring threshold of the hydrogel (Figure 16).

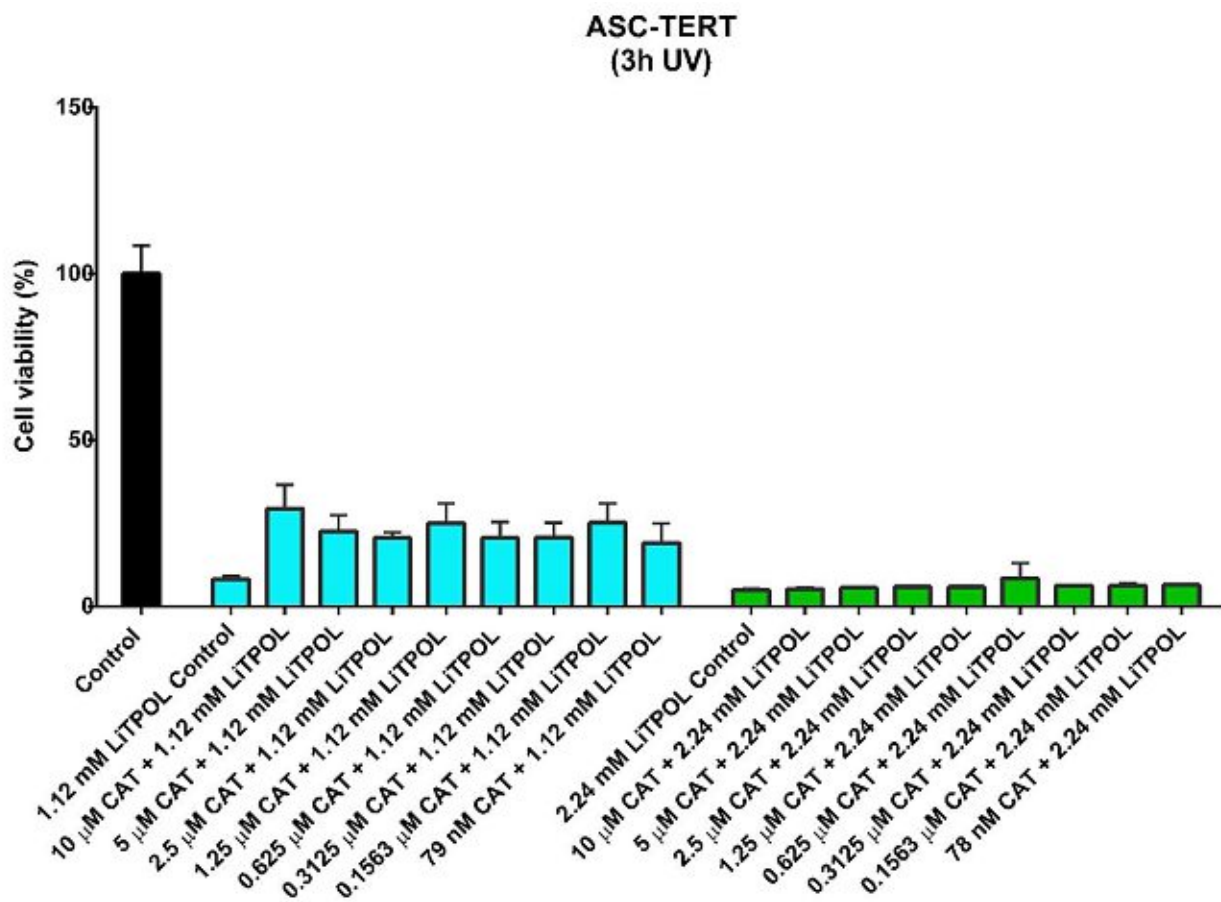


Figure 14. ASC/TERT1 cells treated with different concentrations of CAT.

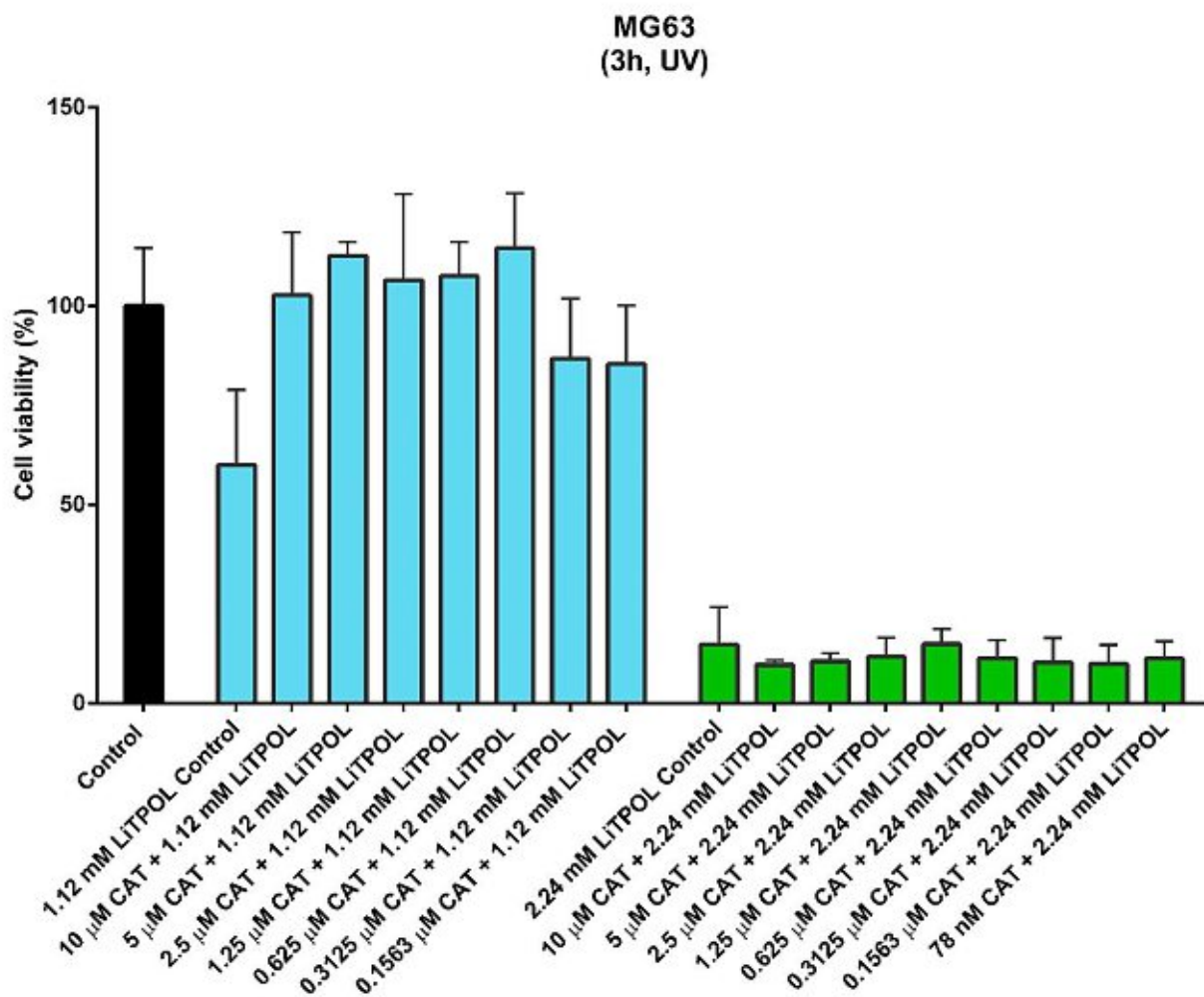


Figure 15. MG63 cells treated with different concentrations of CAT.

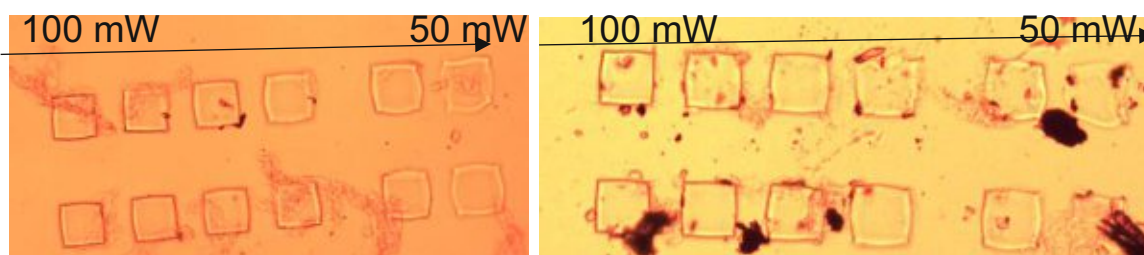


Figure 16. Left image: Cubes produced using 10% GelMOD-97 supplemented with 1 mM P2CK, right image: Cubes produced with additional 5 μM CAT (Printing parameters: 100x100 μm cubes, 1000 mm/s, 10xNA0.3 objective, hatch: 0.3, dz:0.8, bottom to top, 100-50 mW)

#### 2.2.4.6 Crosslinkers and Co-Initiators

The toxicity of different thiolated crosslinkers such as tri-thiol crosslinker, ethoxylated-trimethylolpropane tri-3-mercaptopropionate (ETTMP), and di-thiol crosslinker DTT,

co-initiator methyldiethanolamine (MDEA) and triethanolamine (TEA) were tested for both structuring and cell viability.

ETTMP has been utilized as a crosslinker for the polymerization of thiol-acrylate polymers based on PEG, and other thiol-ene crosslinked networks.<sup>100,101</sup> DTT has been successfully employed in numerous applications as a crosslinker, including the crosslinking of co-polymers of PEG and poly( $\epsilon$ -caprolactone), norbornene-modified gelatin, modified-Pluronics among other.<sup>102–104</sup> In one study a thiol-containing polyurethane was employed as photoinitiator together with MDEA and was used for the photopolymerization of trimethylolpropane triacrylate.<sup>105</sup> TEA has been previously shown to be a sufficient co-initiator for safranin-T dye for the photopolymerization of acylamide.<sup>106</sup> Furthermore, TEA has also been utilized to efficiently crosslink methyl methacrylate using the dye thionine, while when TEA was absent, the photopolymerization was unable to proceed.<sup>107</sup>

MG63 cells were treated with the substances for 3 h at room temperature since the 2PP process is performed at this temperature and the maximum printing time was set to never exceed 3 h. ETTMP was eminently toxic, while cells tolerated MDEA, TEA and DTT at much higher concentrations as well (**Figure 17, Figure 18 and Figure 19**). The highest biocompatible concentrations of each were tested for structuring with 10% GelMOD-95 with 1m M P2CK and 24 h after printing pictures were taken of the developed structures. The application of DTT resulted in increased structuring integrity and lower 2PP threshold compared to the control (**Figure 20**), while the MDEA and TEA did not show any improvement compared to the control (**Figure 21**).

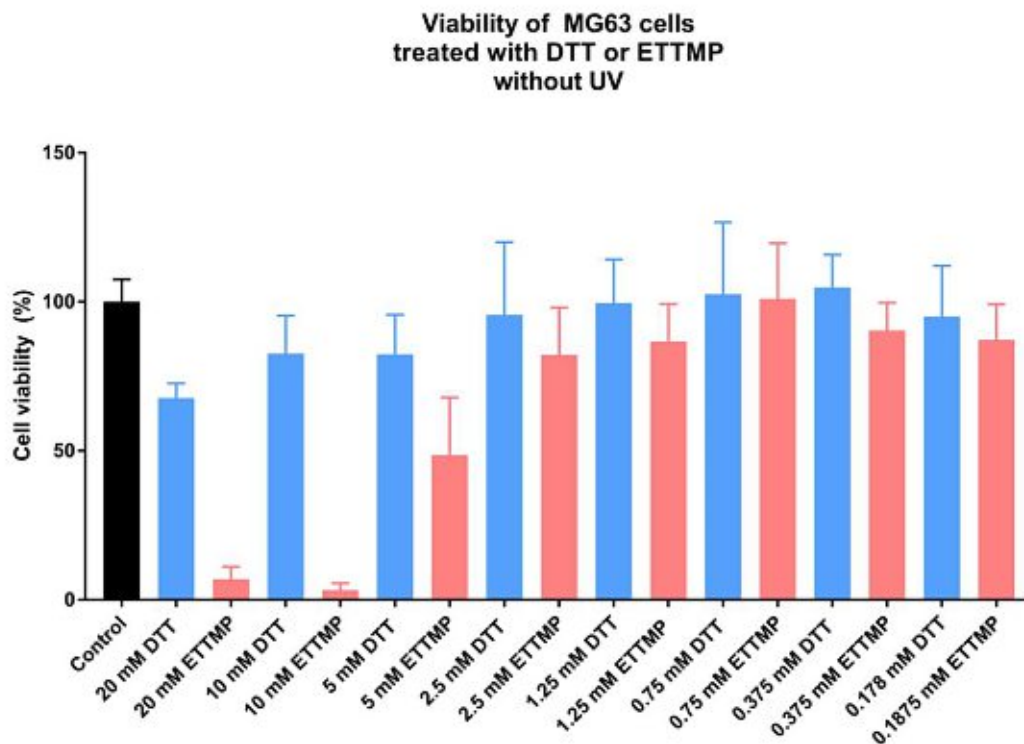


Figure 17. MG63 cells treated with different concentrations of DTT and ETTMP.

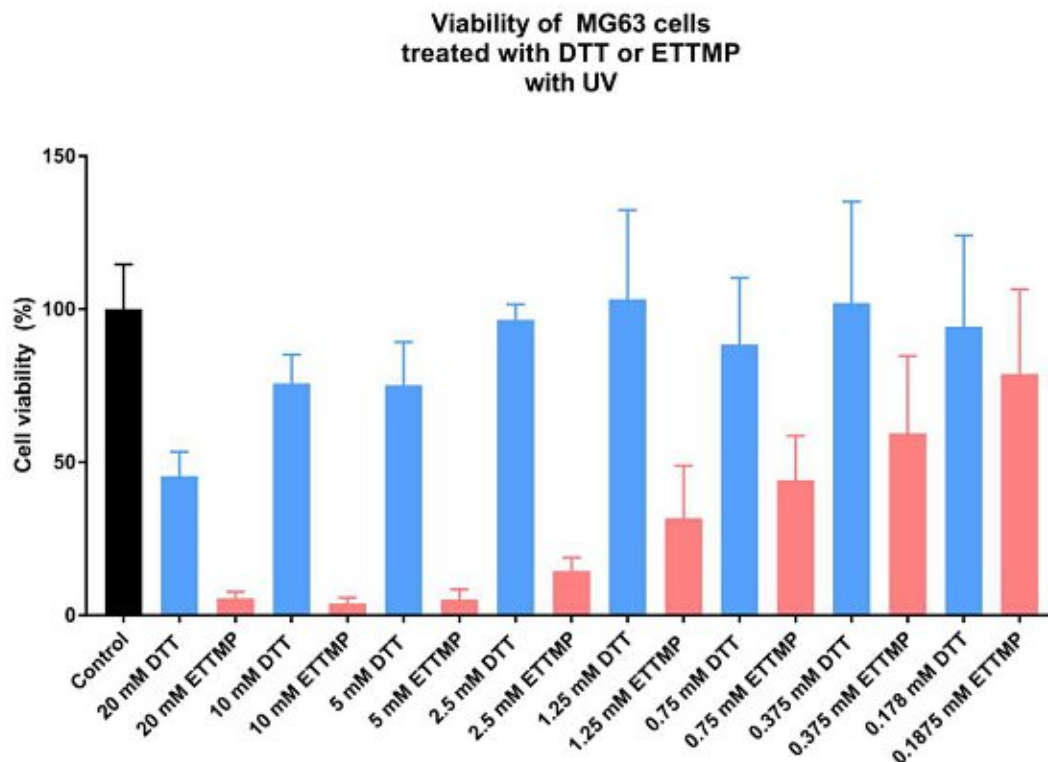


Figure 18. MG63 cells treated with different concentrations of DTT and ETTMP followed by 10 min UV irradiation.



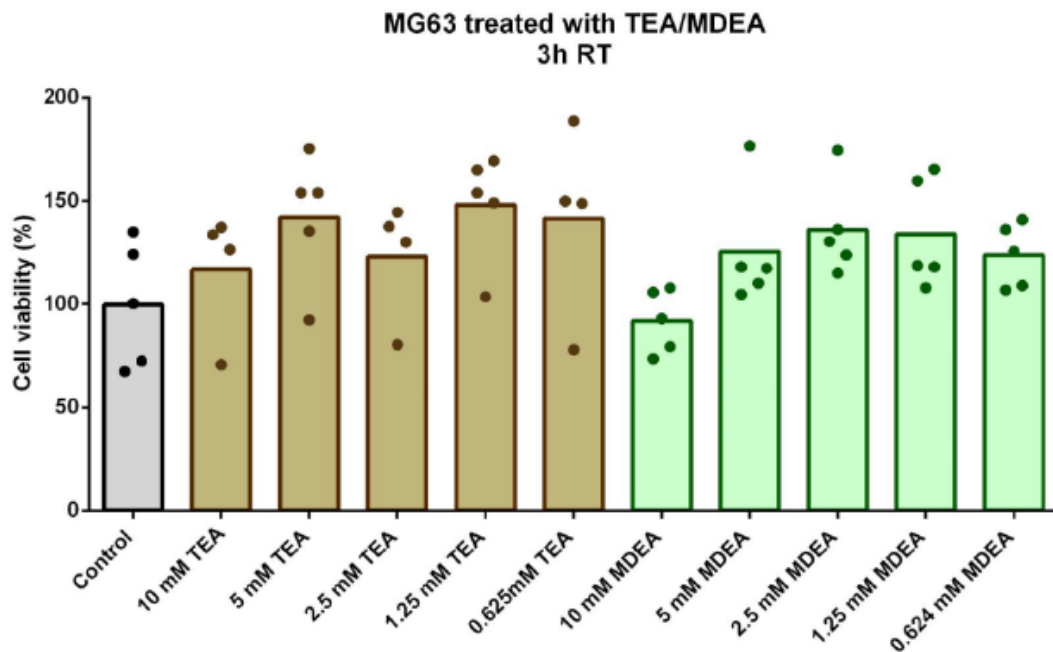
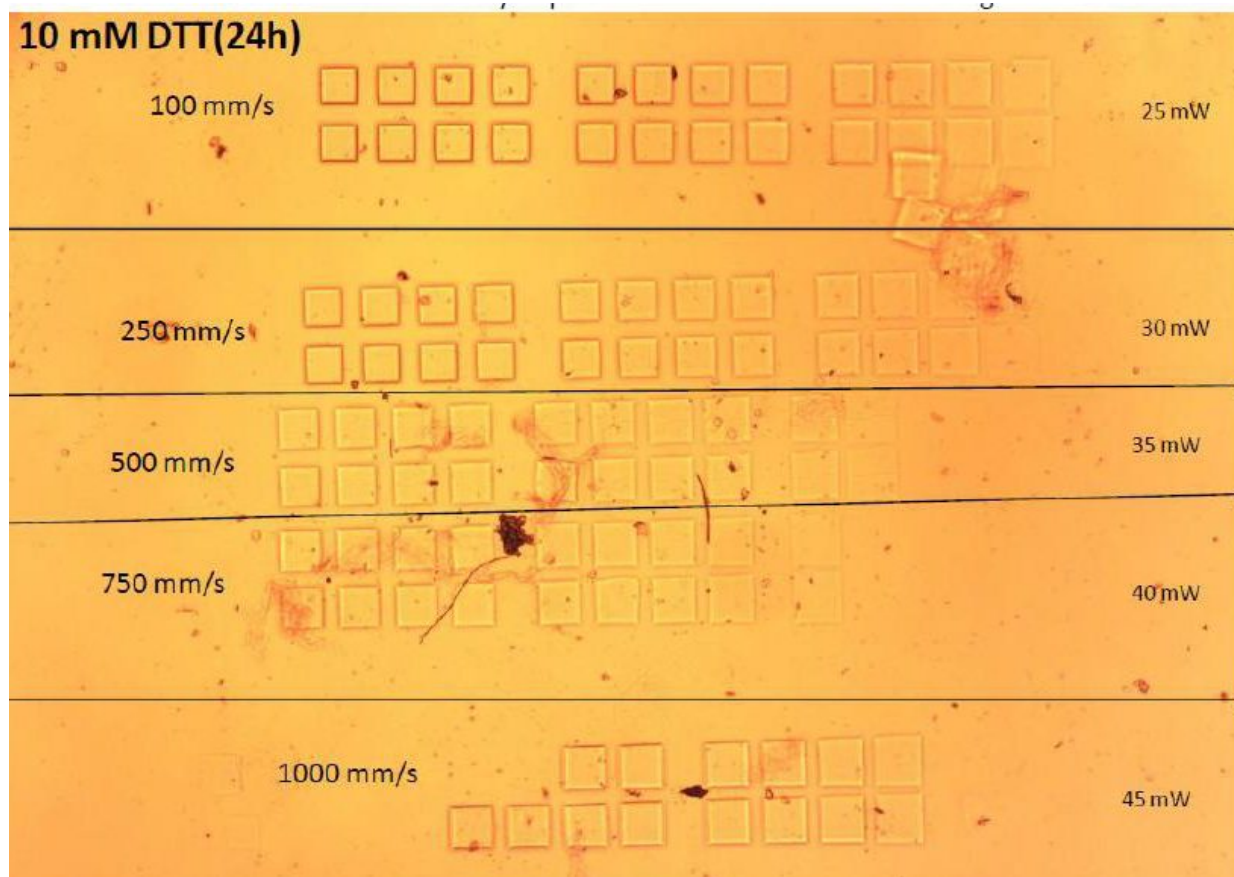


Figure 19. MG63 cells treated with different concentrations of MDEA and TEA.



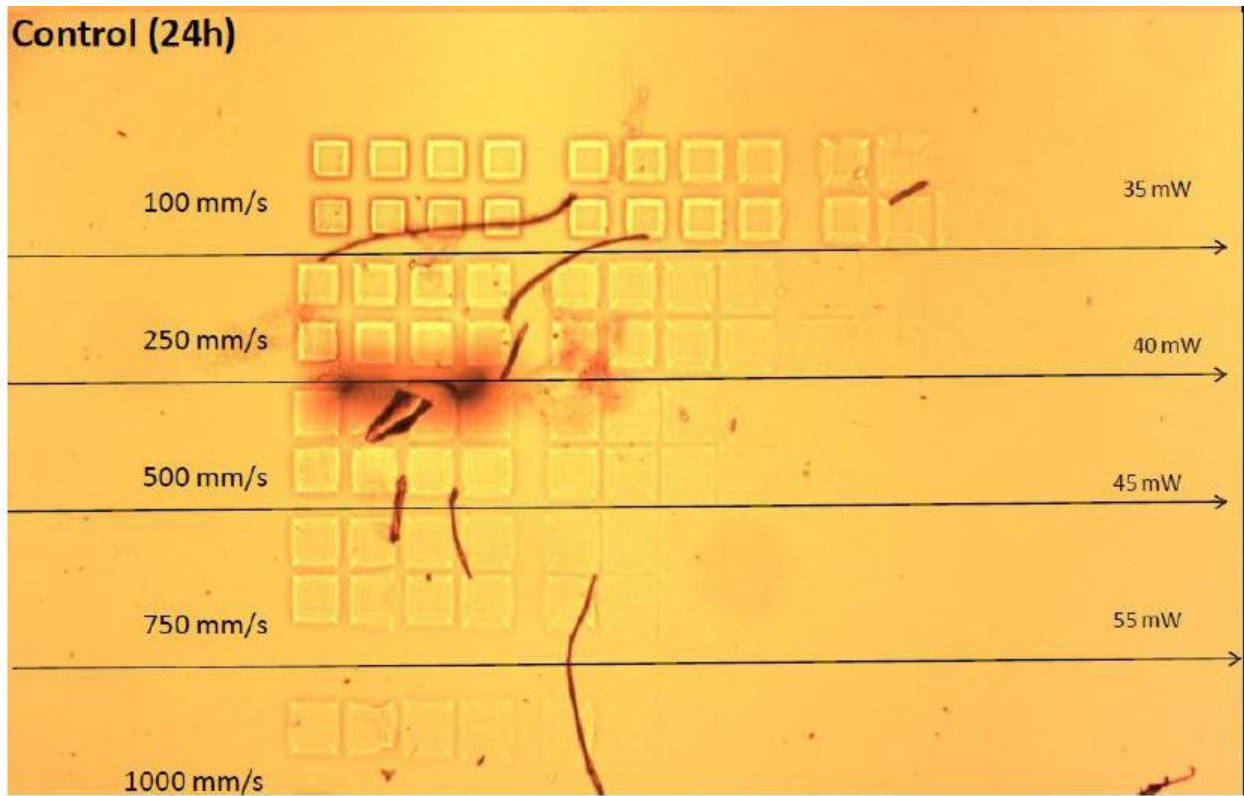
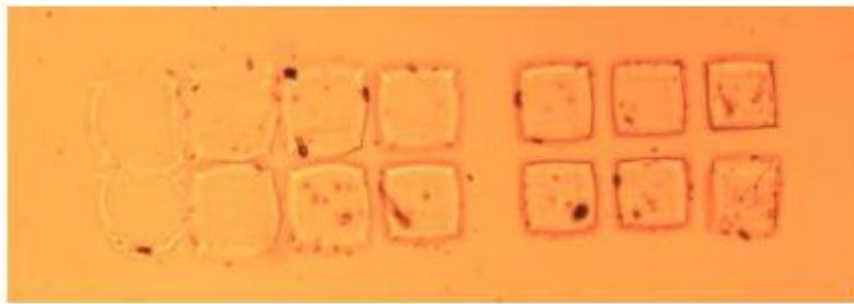


Figure 20. 100x100  $\mu\text{m}$  cubes printed with or without 10 mM DTT (10x.0.3 objective, hatch: 0.3, dz:0.8, bottom to top). The power (in mW) needed to achieve the threshold at a certain writing speed is indicated at the right side of the picture.



(10 mM TEA)



(2,5 mM MDEA)



**Figure 21. Structuring with TEA and MDEA and co-initiators using the following parameters. 10% GelMOD-97 supplemented with 1 mM P2CK (100x100 µm cubes, 100 mm/s, 10xNA0.3 objective, hatch: 0.3, dz:0.8, bottom to top, 10-100mW)**

## 2.2.5 Conclusion

Several different substances with known antioxidant properties were tested on different cell lines to evaluate their capacity to improve cell survival upon UV irradiation. Ascorbic acid improved the viability of the UV-treated cells compared to the control, however it failed to increase the metabolic activity when PI was introduced to the cells additionally to the light treatment. NAC, GSH and GA did not show any improvement in cell viability when applied together with Li-TPO-L and UV light. Catalase was the only tested substance which showed significant improvement in cell viability and it also did not affect the integrity of the structuring when it was tested in a 2PP setup. Additionally, several different crosslinkers and co-initiators were tested. DTT and TEA was well tolerated by cells up to 10 mM, MDEA up to 2.5 mM while even 0.18 mM ETTMP was toxic to the cells in the presence of UV light. However, when tested for structuring MDEA and TEA did not improve the printing threshold, while DTT decreased the 2PP threshold by 10 mW.

## 2.3 Thiol-Gelatin-Norbornene Bioink for Laser-based High-Definition Bioprinting

This chapter is published and contains text from publication

Dobos A, Van Hoorick J, Steiger W, Gruber P, Markovic M, Andriotis O G, Rohatschek A, Dubruel P, Thurner P J, Van Vlierberghe S, Baudis S and Ovsianikov A **2019** Thiol–Gelatin–Norbornene Bioink for Laser-Based High-Definition Bioprinting *Adv. Healthc. Mater.* 1900752

DOI:10.1002/adhm.201900752

The synthesis of Gel-NB was carried out by J. Van Hoorick (University of Ghent).

The python-based degradation program was written by W. Steiger (TU Wien).

The AFM measurement were carried out by O. Andriotis (TU Wien).

### 2.3.1 Introduction

The field of 3D bioprinting has demonstrated a considerable progress within the recent decade, with new or refined technologies and materials reported constantly.<sup>18</sup> However, until now, the low resolution of conventional technologies remained one of the main unconquered frontiers in 3D bioprinting.<sup>26,108</sup> Indeed, since most of 3D bioprinting methods rely on depositing the material with the cells, their resolution is few tens of micrometres at best and thus is not sufficient to recreate complex geometries, intrinsic architecture of the ECM or to change the material properties on the subcellular level. Lithography-based approaches can overcome this limitation by locally crosslinking the material containing living cells instead of depositing it to create 3D geometries.<sup>35</sup> In particular, two-photon polymerization (2PP) is capable of spatial resolution well into sub-micrometre range. It is often incorrectly anticipated that 2PP has a limited throughput due to the hardware limitations resulting in an extremely low scanning speed in the order of tens to few hundred micrometres per second. However, already over 5 years ago our group has demonstrated that 2PP systems are capable of scanning as fast as 500–1000 mm s<sup>-1</sup>.<sup>109,110</sup> When it comes to bioprinting, the main bottleneck for 2PP was availability of biocompatible and highly reactive material, supporting high-speed processing of cell-containing materials at moderate laser powers.

Radical thiol-ene click reaction, based on the remarkably efficient reaction of thiols with non-homopolymerizable carbon-carbon double bonds, leads to a step-growth polymerization and network formation, via repeated addition of thiyl radicals to double bonds and chain transfer reactions by hydrogen abstraction.<sup>59</sup> Thiol-ene reactions can be performed under mild conditions and can result in a highly biocompatible hydrogel. Since no homo-polymerization occurs between the norbornene groups, it will only react with thiols in a stoichiometric ratio resulting in a single orthogonal covalent bond unlike (meth)-acrylate/amide-based hydrogels, which often form heterogeneous networks due to the formation of kinetic oligo(meth)acrylate chains.<sup>59</sup> Both natural and synthetic polymers have been functionalized with either thiol or “ene” moieties, including hyaluronic acid (HA), gelatin and polyethylene glycol (PEG).<sup>58,103,111–114</sup>

Direct embedding of human mesenchymal stem cells (hMSCs) into gelatin-norbornene hydrogels (Gel-NB) was reported previously via UV-polymerization and resulted in

higher cell survival when compared to standard GelMOD hydrogels.<sup>103</sup> In another report, matrix metalloproteinase degradable poly(ethylene glycol)-based (PEG-based) thiol-ene hydrogels also proved useful for the encapsulation and differentiation of hMSCs into osteogenic, chondrogenic and adipogenic lineage.<sup>115</sup> Thiol-ene click reactions can also be applied to alter the properties of the hydrogels after crosslinking without changing the base composition, as demonstrated by using unreacted norbornene functionalities on a partially crosslinked HA-norbornene gel to introduce secondary functionalities using thiol-ene photo-grafting, thereby either locally changing the mechanical properties of the hydrogel or introducing localized functionalities after polymerization.<sup>111</sup>

Several different thiol/ene modified materials have been successfully employed with 2PP, including thiol-ene modified poly(vinyl alcohol), gelatin vinyl ester and Gel-NB.<sup>113,114,116</sup> However, direct embedding of cells during 2PP processing while maintaining cell viability has only been achieved with GelMOD bioinks.<sup>53</sup>

### 2.3.2 Aim

The present work focuses on the characterization of 3D printed Gel-NB based bioinks and the direct embedding of cells via 2PP. After optimization of polymer, crosslinker and photoinitiator concentrations, the processing window for 2PP at 720 nm was established. 720 nm processing wavelength was chosen due to the better match to the absorption properties of the used 2PI DAS.<sup>53,117</sup> The mechanical properties of the hydrogel were characterized via atomic force microscopy (AFM) cantilever-based microindentation, and the equilibrium swelling and enzymatic degradation by collagenase was also determined. Direct embedding of L929 mouse fibroblast cells was performed via 2PP for long-term 3D cell studies, during which cell viability, proliferation, morphology and migration of cells were addressed. In addition, the cell loading capacity of direct encapsulation into porous scaffolds with a variety of pore sizes was compared to conventional scaffold seeding. Finally, the cells were embedded within 3D structures characterized by a cross-linking density gradient and the morphology of cells within different regions was observed in the course of 3 week. To our best knowledge this is the first systematic study showing the possibility to

produce cell-embedding hydrogel constructs by 2PP technology at a relatively high throughput, paving the way to high-definition bioprinting.

### 2.3.3 Experimental

Unless stated otherwise, all chemicals and cell culture reagents were purchased from Sigma-Aldrich (St.Louis, MO, USA). All graphs were plotted using GraphPad Prism 6.

#### 2.3.3.1 *Gel-NB Hydrogel Preparation*

Gel-NB with a degree of substitution of 53% was synthesized following a previously reported protocol.<sup>113</sup> For the laser processing experiments Gel-NB was dissolved in PBS to obtain a final concentration of 7.5 wt% at 37 °C. After complete dissolution, 0.5 mM of the 2PI DAS and the crosslinker DTT at an equimolar thiol-ene ratio were added. Next, 30 µL of the obtained solution was pipetted into a silicone mold with a diameter of 6 mm and height of 1 mm placed on the methacrylated glass bottom dishes.<sup>53</sup>

#### 2.3.3.2 *Cell Culture*

L929 mouse fibroblast cells and L929 cells labelled with mCherry (provided by Ludwig-Boltzmann Institute, Vienna, Austria) were cultivated at 37 °C and 5% CO<sub>2</sub> in the incubator. The retroviral transfection of the cell line is described elsewhere.<sup>118</sup> Cells were cultured in DMEM high glucose media supplemented with 1% penicillin-streptomycin solution and 10% FBS. Upon 90% confluency, the cells were detached using 0.5% trypsin-EDTA solution and centrifuged at 170 g for 5 min followed by plating in T75 flasks (VWR, Radnor, USA)

#### 2.3.3.3 *Laser Setup*

A tunable femtosecond laser with a repetition rate of 80 MHz (MaiTai eHP DeepSee, Spectra-Physics) was operated at 720 nm. A schematic of the printer is described at **Figure 22**.

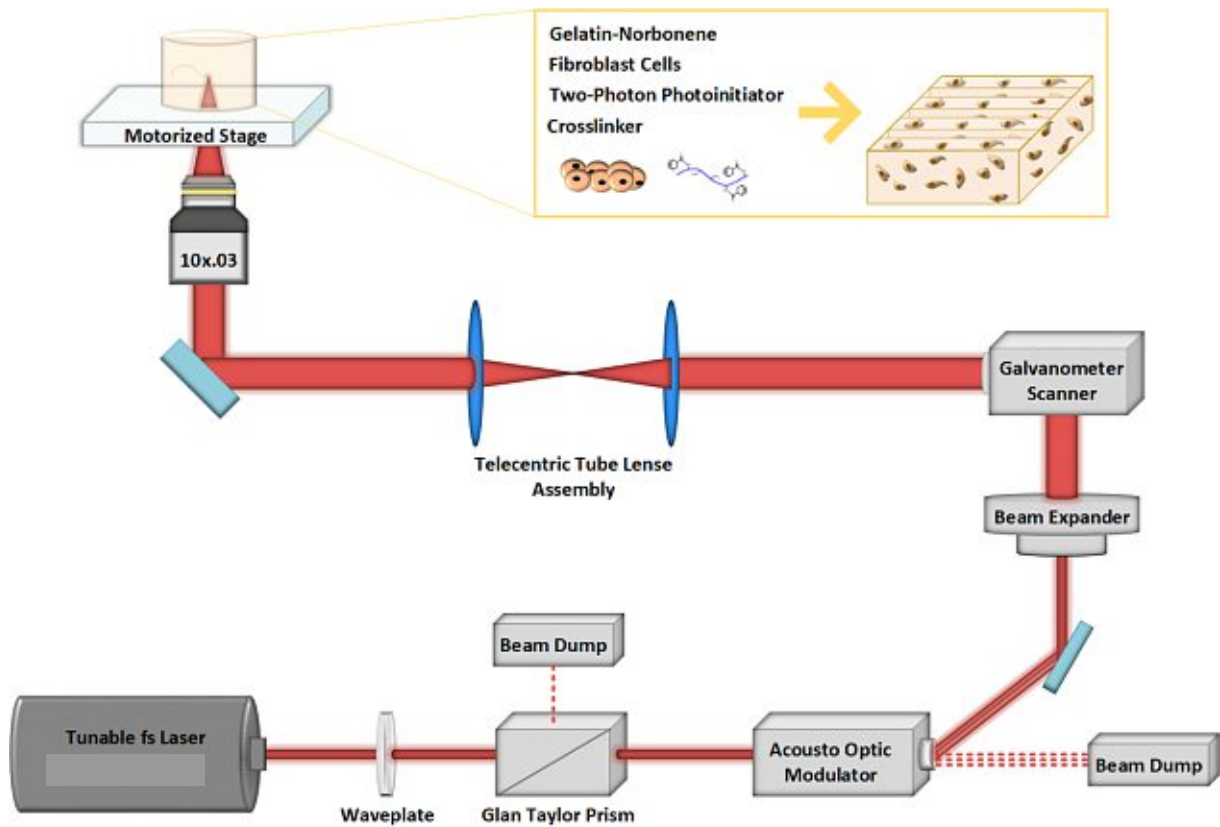


Figure 22. Schematic design of the used 2PP setup.

#### 2.3.3.4 Methacrylation of Glass Slides

To ensure proper attachment of the 3D printed hydrogel structures to the substrate, the glass surfaces were modified with methacrylate functionalities following a silanization procedure described in Chapter 2.1.3.6.

#### Structuring threshold

100 x 100  $\mu\text{m}$  cubes were printed in the above-mentioned hydrogel formulation with different laser powers (10-100 mW) and scanning speeds ranging from 100-1000  $\text{mm s}^{-1}$ . Afterwards, the unpolymerized material was washed away with PBS at 37°C and the cubes were imaged using brightfield optical microscopy (Zeiss, Oberkochen, Germany). The threshold was defined as the minimal required laser power to yield a stable structure.

### 2.3.3.5 Equilibrium Swelling

The above-mentioned 100 x 100 μm cubes were printed followed by incubation at 37°C overnight. The swelling ratio of the hydrogels was obtained semi-quantitatively, by measuring the surface area of the top of the CAD image and comparing this to the surface area of the top slice of the printed cube. The swelling was calculated by the following formula (**Equation 2**).

$$Q = \frac{A_{cube} - A_{CAD}}{A_{CAD}} * 100 \quad (2)$$

Where Q is the swelling ratio, A is the surface area in μm<sup>2</sup>.

### 2.3.3.6 Degradation Scanner

The degradation of the hydrogel was performed using collagenase from *Clostridium histolyticum*. To this end, 100 x 100 μm hydrogel cubes were structured at 1000 mm s<sup>-1</sup> using 60, 80 or 100 mW and incubated in PBS overnight at 37 °C to reach equilibrium swelling. Afterwards, a 1 mg mL<sup>-1</sup> 2000 kDa FITC labelled dextran (TdB Consultancy AB, Uppsala, Sweden) was added to the collagenase solution to make fluorescent imaging possible. The collagenase solution was added to the samples at a final concentration of 0.25 CDU/mL and time lapse Z-stacks of the cubes were recorded every 5 min using confocal laser scanning microscopy (Zeiss, Oberkochen, Germany).

The degradation scanner is an analytical tool that was developed to quantify the change in volume of a 3D structure. Using Z-stack images obtained from the LSM microscope, a python-based code reads the images for each layer. The image is separated into a grid which can be adjusted by the viewer. Translating the image data into an array of 8-bit values allows to determination of threshold intensity. This intensity value is used to discriminate between solid structures (dark areas in **Figure 23**) and surrounding liquid. For each region, the pixels which meet the criterion are summed up and multiplied using the image conversion factor (obtained with the image analysis tool from a reference structure). Knowing the surface (μm<sup>2</sup>) of a single pixel as well as the distance between each layer image allows the calculation of the volume of each structure. Adding the results for each area and each layer enables to do the calculation of the total volume of each structure at different time points until the structures were fully degraded.



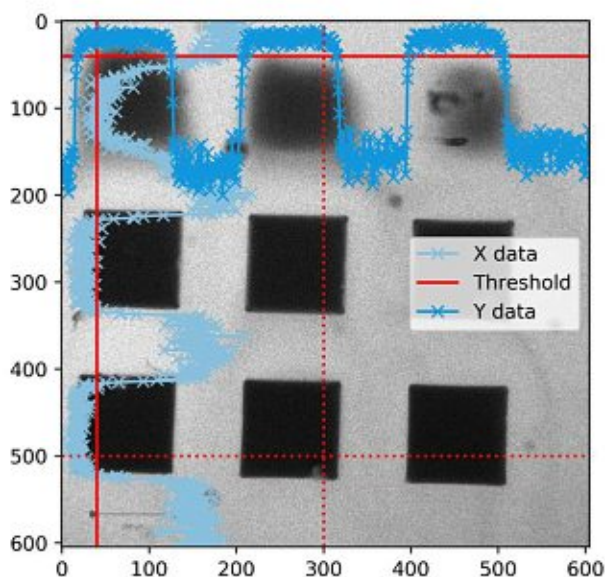


**Figure 23. Visualization of the degradation scanner. Pixels below a given threshold (solid red line) are counted as volume pixels. Knowing the layer spacing  $dz$  and the  $\mu\text{m}^2$  of a single pixel allows the calculation of the total volume of each of the nine cubes.**

### 2.3.3.7 Atomic Force Microscopy

AFM experiments were performed on a NanoWizard® ULTRA Speed AFM system (JPK Instruments AG, Berlin, Germany) equipped with an inverted optical microscope (Axio Observer.D1, ZEISS). Unless otherwise specified, AFM cantilever-based microindentation experiments were performed with the MSNL (0.01 N/m nominal spring constant, cantilever C) (Bruker, Billerica, MA, USA). Prior to mechanical assessment, the thermal noise method was used to determine the spring constant of the cantilever.<sup>119</sup> The measured spring constant of the cantilever was 0.0062 N/m. Then the cantilever was furnished with a colloidal probe made of borosilicate glass.<sup>120,121</sup> The radius of the colloidal probe was determined via atomic force microscopy imaging of a calibration grating (TGT1, NDTMT).<sup>120</sup> AFM cantilever-based indentation experiments were performed in PBS (pH 7.5) on hydrated samples and in force control with a maximum applied load of 1 nN at room temperature. One to two force volume maps were recorded per sample with a 4 x 4-pixel resolution resulting in 16 to 32 force-indentation curves per sample. The indentation modulus was estimated by analyzing the unloading part of the force-indentation curves as described previously using the Oliver-Pharr method.<sup>120,122</sup> All force-indentation data were processed in a



custom built Matlab script (2015b, The MathWorks Inc., Natick, Massachusetts, United States.)

#### 2.3.3.8      *Cell-containing hydrogels*

The cells were trypsinized and resuspended at  $1 \times 10^6$  cells per mL in 7.5 % Gel-NB supplemented with 0.5 mM DAS and DTT at an equimolar thiol-ene ratio. The hydrogel precursor solution was pipetted into the aforementioned silicone mold in glass bottom methacrylated dishes.

#### 2.3.3.9      *Cell viability*

In order to assess the cell viability after printing, L929 cells were embedded using the above-mentioned protocol in  $200 \times 200 \times 200 \mu\text{m}^3$  cubes printed at  $1000 \text{ mm s}^{-1}$  writing speed and different laser powers (40-120 mW). After printing, the structures were immersed in cell culture medium at  $37^\circ\text{C}$  for 1 h to remove the non-polymerized material. Afterwards, the cells were stained with Calcein AM/Propidium iodide live-dead staining according to the manufacturer's protocol for 30 min before LSM images were taken. After imaging, the cell culture media were changed and the staining was repeated 24 h later. The number of dead and alive cells were counted manually.

#### 2.3.3.10      *Ki-67 Immunostaining*

In order to address the effect of the different stiffnesses on proliferation, mCherry L929 cells were embedded in the above-mentioned fashion in a cube with unidirectional channels printed with different laser powers. The cells were incubated in cell culture medium for 1 week before fixation using 4% Histofix (Carl Roth GmbH, Karlsruhe, Germany) for 1 h. Afterwards, the fixed structures were washed with PBS and permeabilized with 0.5 % Triton-X in 1 wt% bovine serum albumin dissolved in PBS (PBS-BSA) for 15 min. The non-specific absorption of the antibodies was blocked by incubation with PBS-BSA for 15 min prior to the addition of primary anti Ki-67 antibodies (Abcam, Cambridge, United Kingdom) in a dilution of 1:200 overnight at  $4^\circ\text{C}$ . Afterwards, the cells were washed three times for 5 min with PBS-BSA before the addition of the Goat anti-Rabbit IgG (H+L) Superclonal™ Secondary Antibody, Alexa Fluor 488 (Thermo-Fisher, Waltham, MA, USA) for 2 h. Next, the structures were washed again two times for 5 min with PBS-BSA before the addition of DAPI (Biotium Inc, Fremont, CA, USA) in a dilution of 1:200 in PBS-BSA for 1 h. The cells were

imaged using LSM and the number of proliferating cells and cell nuclei were counted both in the crosslinked hydrogel and in the channels. As control, cells growing on glass substrate were used.

All structures were printed with a laser writing speed of 1000 mm s<sup>-1</sup>.

#### 2.3.3.11      *Power distribution*

To assess the effect of material stiffness in the achievable range, a 500 x 500 x 200 μm<sup>3</sup> cube with an inverse gaussian power distribution with laser powers ranging from 85 mW down to 45 mW was produced. The autofluorescence of the material was imaged using LSM. The fluorescence intensity of the cross-section of the cube was analysed using ImageJ. Afterwards, mCherry L929 cells were embedded in 7.5% Gel-NB hydrogels using the above-mentioned protocol and the inverse gaussian cube was structured. The cell morphology was assessed by imaging the cells in the different regions of the cube over 3 weeks.

#### 2.3.3.12      *Scaffold seeding and direct cell encapsulation*

Gel-NB scaffolds with different pore sizes (10-40 μm) were produced using 7.5% Gel-NB supplemented with 0.5 mM DAS and an equimolar thiol/ene ratio of DTT. The constructs were developed in cell culture media and incubated overnight before the seeding of mCherry L929 cells at a concentration of 1 x 10<sup>6</sup> cells per mL. The cells were left to sediment and attach for the same time as the direct encapsulation takes (approximately 1 h). The same porous structures and concentration of cells were used for direct encapsulation using the above-mentioned protocol. After printing, the constructs were immersed in cell culture media. All structures, both for direct encapsulation and seeded scaffolds, were printed using 90 mW laser power and 1000 mm s<sup>-1</sup> writing speed. Images were taken using LSM. The cells in the structure were counted manually. All cells which attached to the top and to the sides of the structures were disregarded.

### 2.3.4 Results and Discussion

A concentration of 7.5 wt% Gel-NB supplemented with 0.5 mM cleavable biocompatible diazosulfonate photoinitiator (DAS) in PBS was sufficient for producing stable structures at high writing speeds. The bifunctional low-molecular-weight

dithiothreitol (DTT) was used as crosslinker.<sup>113</sup> The concentration of thiol groups using DTT was chosen to be equimolar in respect to the norbornene functionalities present on the gelatin, since in an ideal network an excessive amount of thiols results in a higher ratio of mono-reacted thiol-groups while a lower amount results in unreacted norbornene functionalities, leading to incomplete network formation.

To establish a processing window, different laser powers and writing speeds were tested on the hydrogel formulation. The schematic design of the 2PP setup used is depicted in **Figure 22**. An array of cubes was produced with writing speeds ranging from 100 mm s<sup>-1</sup> to 1000 mm s<sup>-1</sup> and the minimal power needed to obtain stable structures, also referred to as 2PP threshold, was established for each speed. With increasing speed, the structuring threshold increased from 15 mW to 40 mW (**Figure 24a**). Remarkably high speeds can be achieved with considerably lower laser powers when compared to similar material formulations using GelMOD together with DAS or other chain-growth based gelatin derivatives.<sup>53,123</sup>

In an ideal case, if there are no irregularities in the hydrogel network due to unreacted functional groups and primary cycles (i.e. linking of different functionalities on the same gelatin chain to each other), the equilibrium swelling ratio should reach a constant value at a fixed monomer concentration.<sup>57</sup> Since the light dose has an effect on the crosslinking density, the equilibrium swelling of the samples as a function of writing speed and laser power was established. At the lower laser powers, which are close to the polymerization threshold, the swelling was higher due to a lower degree of crosslinking. In the upper average laser power range (60-100mW), the equilibrium swelling of the cubes corresponded to the expected behaviour of an ideal step-growth hydrogel network, hence the swelling ratio showed little variation between different writing speeds and powers (**Figure 24b**). Previous reports addressing the UV crosslinking showed full conversion at a thiol-ene ratio of 1:1 with Gel-NB – DTT systems, whereas gels with a 0.5:1 ratio exhibited increased swelling and decreased stiffness.<sup>113</sup> However, our results at 100 mm s<sup>-1</sup> (and to a lesser extent at 500 mm s<sup>-1</sup>) indicate an increase in swelling towards higher laser powers. Furthermore, at 100 mm s<sup>-1</sup> the swelling ratio was higher in every case compared to 500 and 1000 mm s<sup>-1</sup>. We hypothesize that this behaviour is the consequence of localized thermal effects, since at lower scanning speeds more energy is supplied per unit of time. It is known that the stability of DTT decreases drastically at increased temperatures.<sup>124</sup> Consequently, at

100 mm s<sup>-1</sup> and at high laser intensities, the thiol/ene ratio will no longer remain equimolar due to degradation of the crosslinker. Secondly, due to the high irradiation energy, a large number of DTT molecules can be coupled to the norbornene functionality very fast, resulting in a drastic increase of viscosity. Hence, the diffusion of unreacted DTT molecules towards unreacted norbornene sites would be limited, resulting in weaker network formation.<sup>114,125</sup> Finally, at high energy doses, the number of thiol radicals can be so high, that termination occurs due to combination of two thiol radicals resulting in concurrent disulfide formation, thereby again resulting in non-equimolar thiol-ene ratios.

Gelatin naturally contains amino acid sequences cleavable by matrix metalloproteinases (MMPs).<sup>126</sup> The degradation of the hydrogel caused by MMPs are mostly local events due to the short-range action of proteases. When exogenous collagenase is added at the concentration of 0.25 collagen digestion units (CDU) mL<sup>-1</sup>, surface erosion is expected to be the main process. However, proteases can also diffuse into the hydrogel causing bulk degradation to some degree as well.<sup>29,58,127</sup> To assess this enzymatic degradability, hydrogel cubes printed at 1000 mm s<sup>-1</sup> writing speed with three different laser powers were exposed to a collagenase enzyme and monitored using 3D laser scanning microscopy (LSM) every 5 min. An image analysis program developed in-house was used to determine the decrease of the volume of the structures over time (**Figure 23**) independently of the mechanism of the degradation. By changing the laser power from 60 mW to 100 mW, the hydrogel degradation time increased substantially from 10 min to 30 min, despite observing similar structure swelling behaviour and mechanical properties in this structuring range (**Figure 24c**). Due to the small dimensions of the 2PP-produced hydrogel structures, characterization of their mechanical properties is not a trivial task. However, AFM allows estimation of the indentation modulus (E) of relatively soft hydrogels on a microscale by employing cantilever-based microindentation.<sup>120</sup> The AFM results exhibited a close correlation between the stiffness of the 2PP-produced cubes and the hydrogel swelling. Structures produced at higher writing speeds (1000 mm s<sup>-1</sup>) and lower laser powers (under 60 mW) were the softest (0.2-0.4 kPa). The maximum E indentation modulus was reached at 70 mW (0.7 kPa for 100 mm s<sup>-1</sup>) before decreasing again at higher laser powers. With the faster writing speed of 1000 mm s<sup>-1</sup> E stayed constant at ~0.5 kPa above 60 mW (**Figure 24d**), indicating complete crosslinking.

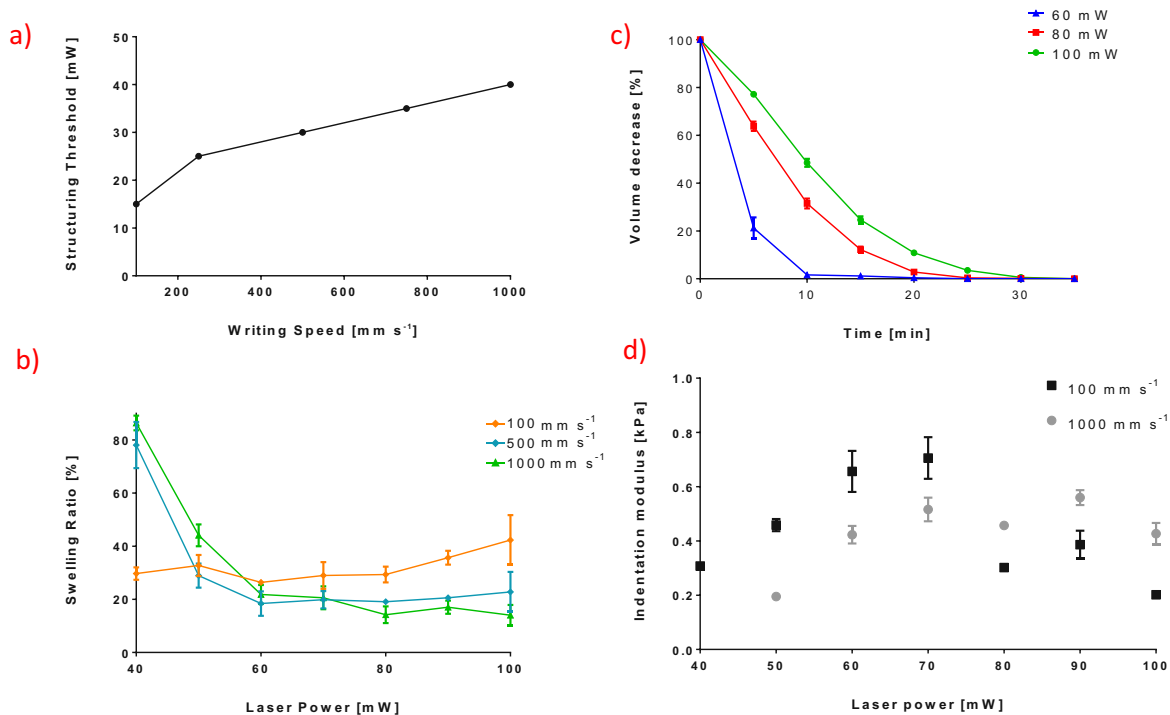


**Figure 24.** Characterization of Gel-NB hydrogels. a) Structuring threshold of a 7.5 wt% Gel-NB hydrogel. Depending on the writing speed, different laser powers are needed to fabricate stable structures. By increasing the writing speed from 100 to 1000 mm s<sup>-1</sup> the structuring threshold is increased by 25 mW. b) The swelling profile of the hydrogels shows low dependency on the writing speed or applied laser power indicating a fully crosslinked network. c) Different structuring powers (at 1000 mm/s) result in different degradation rates when exogenous collagenase (0.25 CDU mL<sup>-1</sup>) was added. By increasing the laser power by 40 mW the acquired time for full degradation was three times higher. d) Atomic force microscopy measurements of Gel-NB hydrogels, processed at different writing speeds. Stiffness of the hydrogels was light dose dependent, with elastic moduli ranging between 0.2 and 0.7 kPa.

Directing cell alignment on a surface or in a 3D hydrogel construct has been reported in literature via several different approaches. Aligning cells in 2D has been performed via soft lithography or self-assembly to position pro-adhesive proteins on glass. However, most of the 2D methods involve micropatterning on rigid surfaces, which does not properly mimic *in vivo* conditions. Micro-engineered 3D matrices provide closer resemblance to the natural cell surrounding. Direct cell encapsulation via UV-polymerization and scaffold-based approaches have both been employed in order to control cell alignment and morphology.<sup>128,129</sup> One of the main disadvantages of 3D systems is the lack of spatial control during manufacturing. Additive manufacturing approaches could provide a possible alternative to overcome this issue.

Due to the high resolution of 2PP a high-throughput production of hydrogel-cell constructs by this technology requires high scanning speeds. Using 1000 mm s<sup>-1</sup> writing speed, a 300 x 300 x 300 μm<sup>3</sup> cube could be printed in less than 10 min.

Typically, high writing speeds require high photoinitiator concentrations or high laser powers which could damage the cells. However, by using the highly reactive thiol-ene photo-click chemistry it is possible to produce structures starting from 40 mW at a photoinitiator concentration of 0.5 mM. This is a substantial improvement compared to conventional materials based on chain growth polymerization where 2 mM of the same photoinitiator and approximate twice the light dose was needed to produce stable structures using higher monomer concentrations.<sup>53,123</sup> The reproducibility of the structures was maintained at the higher scanning speeds as the produced structure corresponded well with the CAD model (**Figure 25**).

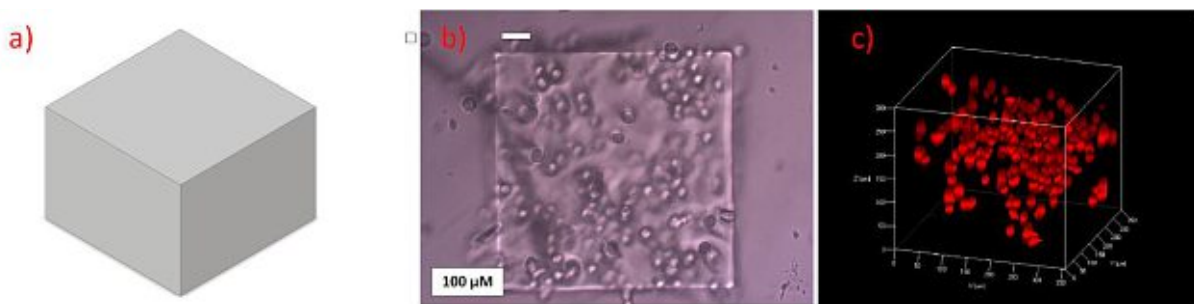


**Figure 25.** mCherry labelled L929 cells embedded in 7.5% Gel-NB hydrogel cubes. The applied laser power did not cause damage of the cells in the irradiated regions. a) CAD image of the printed cube b) Bright field microcopy image of the hydrogel-cell constructs c) LSM Z-stack showing the viable cells in the printed cube.

In order to validate the HD Bioprinting parameters and their effect on cell survival, cubes were printed from the material containing L929 mouse fibroblast cells using a laser power range from 40-120 mW. The cells were co-stained with Calcein AM / Propidium Iodide right after printing (post-printing) and after 24 h. The cell survival was close to 100 % in the structures produced using laser powers below 100 mW and not significantly different for the two time-points in the range of 40-100 mW (**Figure 26a**). However, above 100 mW a decrease of cell viability was observed and the cell survival dropped to 70 % at 120 mW.

In order to demonstrate that the cells not only survive but also maintain their proliferative capacity, cubes with uni-directional channels were produced using laser powers ranging from 50 to 90 mW. In this respect, the cells, which are encapsulated in the structure (channels) but not directly exposed to laser radiation, can be compared to the cells embedded in the crosslinked material using different laser powers (**Figure 26b**). After 1 week in culture, the cells were fixed and anti-Ki-67 antibody with a secondary antibody labelled with Alexa-488 was applied to image proliferating cells using LSM. Additionally, the cell nucleus was stained using a DAPI nuclear stain. Ki-



67 is a frequently used marker which is present during all active phases of the cell cycle but absent in quiescent cells.<sup>130</sup> The results demonstrated that 77% of the cells encapsulated in the structure channels were positive to the Ki-67 marker, which was not significantly different from the 2D control cells (83%). However, the cells embedded in the crosslinked region between 50 and 90 mW had a decreased proliferation, between 32 % and 40 % of the cells being in the active phases of the cell cycle (**Figure 26c**). The laser power within this studied range did not result in any significant differences in observed cell proliferation. Although the number of proliferating cells embedded in the crosslinked hydrogel is approximately half of the control, the cells maintain the capacity to proliferate in 2PP produced constructs (**Figure 26d**).

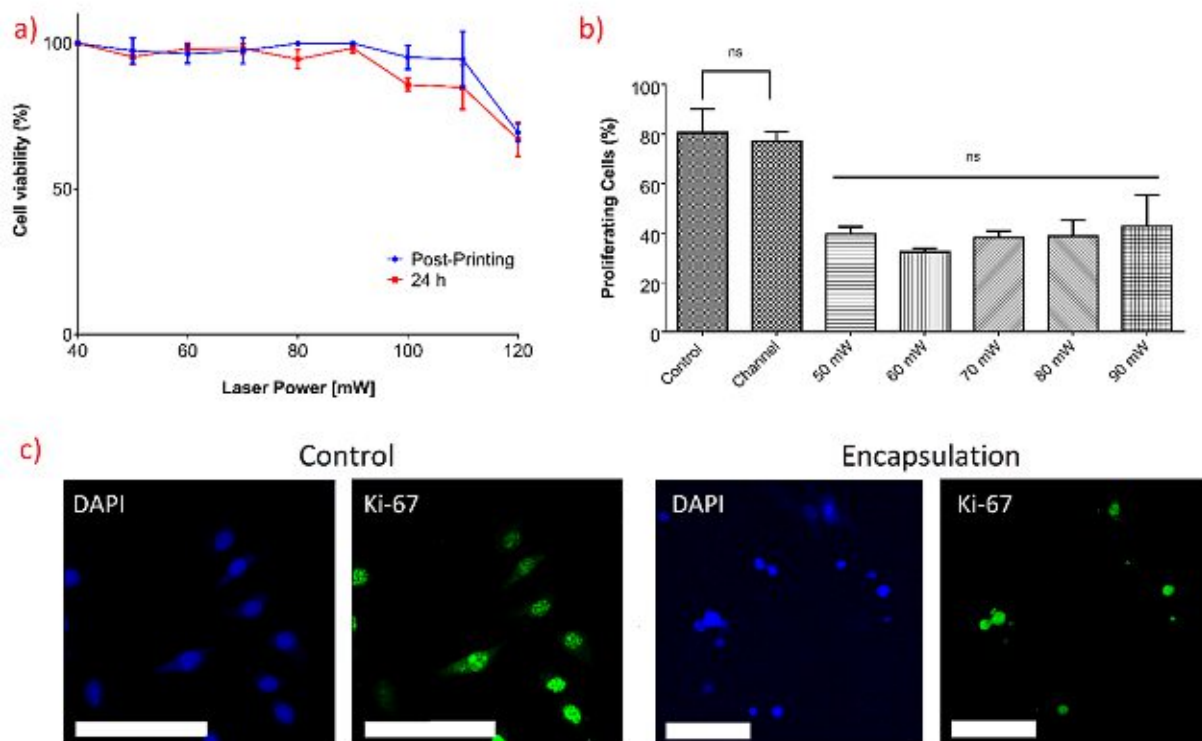


**Figure 26.** Direct encapsulation of L929 mouse fibroblasts in 7.5% Gel-NB hydrogels. a) 1 million per mL L929 cells were embedded using different laser powers (40-120 mW) at 1000 mm s<sup>-1</sup>. The cells were stained with Calcein AM/Propidium iodide to address cell viability. Cell survival was only impaired above 110 mW. b) Proliferation of cells after 1 week of encapsulation. Cells embedded in cubes printed with different laser powers and stained with anti Ki-67 antibodies, visualized using an Alexa-488 labelled secondary antibody. The cells were co-stained with a DAPI nuclear stain. The cells in the non-irradiated regions (channels) were not significantly different from the 2D control. A drop in the proliferation to approximately 35 % can be seen after encapsulation. The studied laser power does not affect the proliferation rate in the studied regions. c) Ki-67 staining of cells. The control cells (2D) show a more extended morphology after 1 week with the vast majority of the cells stained positive to Ki-67. The embedded cells show a rounder morphology with approximately 35 % of cells being in the active phase. The scale bar represents 100 μm. The statistical significance was addressed by one-way ANOVA followed by Bonferroni post-test.

Another important factor apart from cell viability and proliferation is the ability of the cells to migrate within their surrounding matrix. The morphology and migration of cells is highly dependent on the mechanical properties of their environment.<sup>131</sup> By changing the laser power it was possible to tune the indentation modulus of the hydrogel between 0.2 to 0.6 kPa. In order to demonstrate the effect of stiffness on cell morphology and migration, cells were embedded in a cube produced using an inverse Gaussian power distribution with the highest power being 85 mW and the lowest 45 mW at the centre of the cube corresponding to a stiffness of 0.6 kPa and 0.2 kPa, respectively (**Figure 27a**). The polymerized material exhibits some autofluorescence and its intensity corresponds to the applied laser power and concomitant network density (**Figure 27b**). The embedded mCherry labelled L929 cells exhibit a round morphology after one day of encapsulation. However, after 3 weeks of culture, the cells in the softest region (i.e. in the middle) are extended and start to migrate towards the stiffer outer regions, while the cells in the stiffer regions stay round even after 3 weeks (**Figure 27c**).

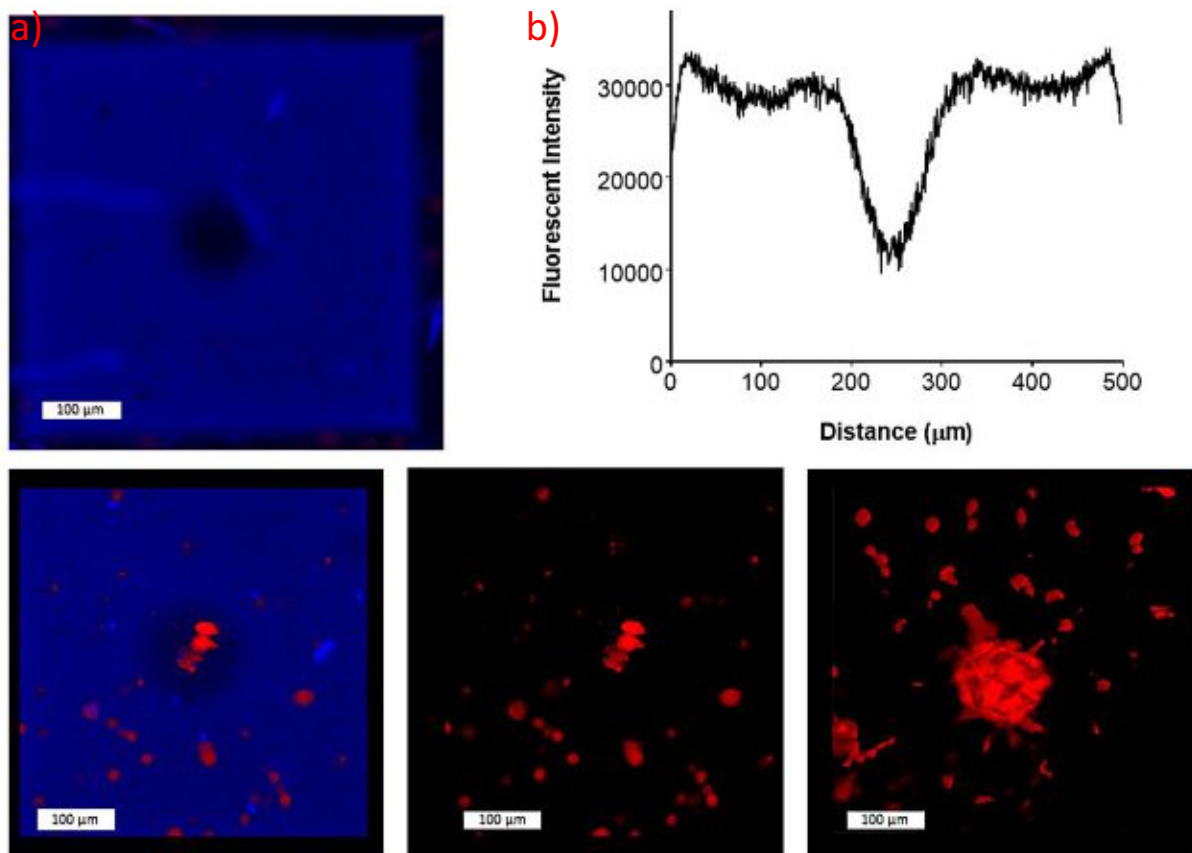


**Figure 27. Morphology and migration of embedded cells in a stiffness gradient cube. a) Cube printed with inverse gaussian power distribution between 45-85 mW. b) The autofluorescence of**



the material was analysed using ImageJ and it corresponds to the expected power distribution. c) mCherry labelled L929 cells embedded in the power gradient cube. After day 1 all cells in the matrix show round morphology while after day 21, cells in the middle softer region are more extended and are migrating towards the stiffer areas as well.

To further demonstrate the potency of the reported system, mCherry labelled L929 cells were embedded in scaffolds with different pore sizes (10-40  $\mu\text{m}$ ). As a control, the scaffolds of identical design were printed and subsequently seeded with the same number of cells (1 million per mL). After printing, the cells were manually counted. The pore size did not affect initial cell numbers in direct encapsulation, and after 7 days the cell numbers increased in all cases. As we demonstrated earlier, cells encapsulated in the channels proliferate faster compared to cells embedded in crosslinked material. Therefore, the increase in cell numbers was more pronounced in the larger pore sized scaffolds (40  $\mu\text{m}$  pore size, from 37 to 78 cells in average) in comparison to the small pore sized structures (10  $\mu\text{m}$ , from 37 to 50 cells in average) due to the larger volume of the channels relative to the crosslinked material volume (**Figure 28b**). However, the cell seeding efficiency in the control group was highly dependent on the pore size: 10  $\mu\text{m}$  pore sized scaffolds had no cells inside the structures, whereas the 40  $\mu\text{m}$  ones had approximately 18 cells per structure, corresponding to only half of the cells in the direct encapsulation experiments (**Figure 28a**).

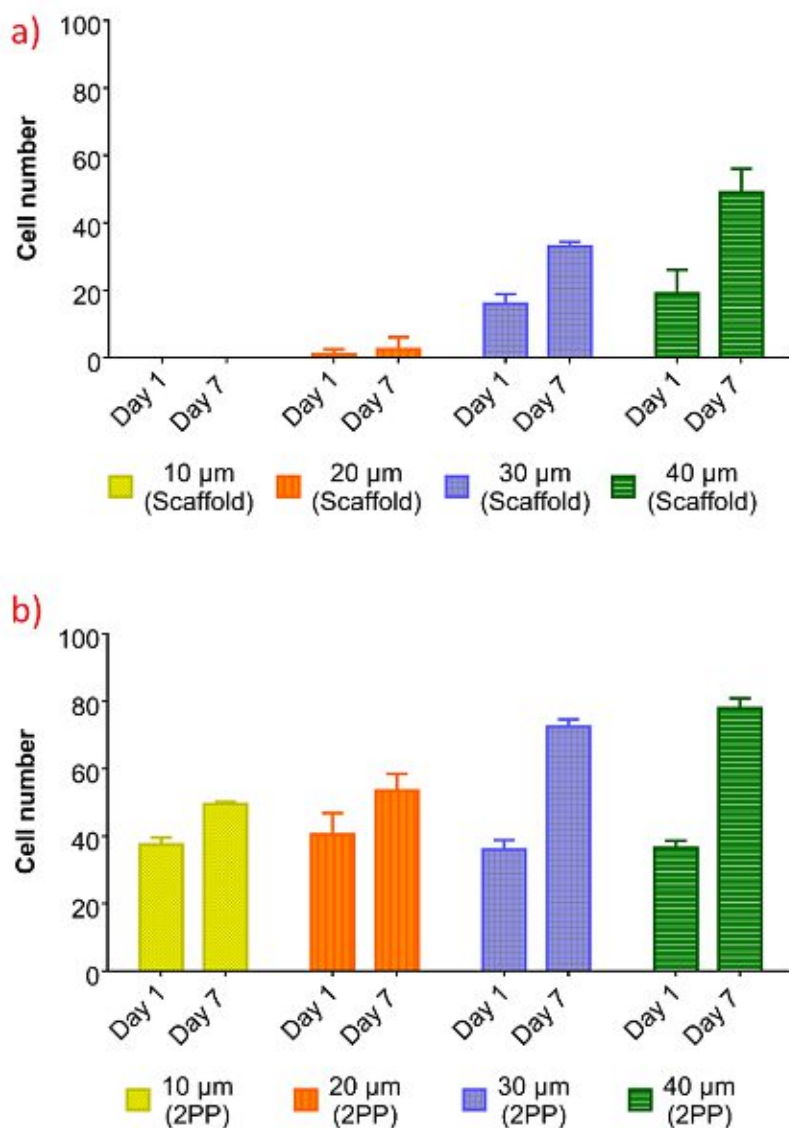


**Figure 28. Cell loading capacity of direct cell encapsulation compared to scaffold seeding. a) Cell numbers after seeding and 7 days. The smallest pore sized scaffold (10 μm) had no cells initially, while with increasing pore sizes the cell numbers increased as well (20 μm: 1 cell, 30 μm: 16 cells, 40 μm: 18 cells in average) b) Cell numbers after seeding and 7 days in direct embedded samples. The initial cell numbers were not significantly different between different pore size samples (10 μm: 37 cells, 20 μm: 40 cells, 30 μm: 36 cells, 40 μm: 37 cells in average).**

Finally, to study long term survival of cells, mCherry L929 cells were encapsulated in a Gel-NB hydrogel construct with an interconnected channel network (with a 20 μm pore size) and wall structure around the perimeter to seal off the channels. After the first week of culture, the cells in the construct remained round along the channels of the printed construct. By week 3, cells aligned along the channels and filled the available space provided by the interconnected network. By week 5, the cells also started to migrate in the crosslinked regions, possibly by partially degrading the

crosslinked material (**Figure 29**). To the best of our knowledge, this is the first time that structure degradation and controlled cell alignment is observed in structures produced via 2PP. Furthermore, the cells can be cultured at least up to 5 weeks in bioprinted Gel-NB hydrogel constructs, which makes long-term studies possible.

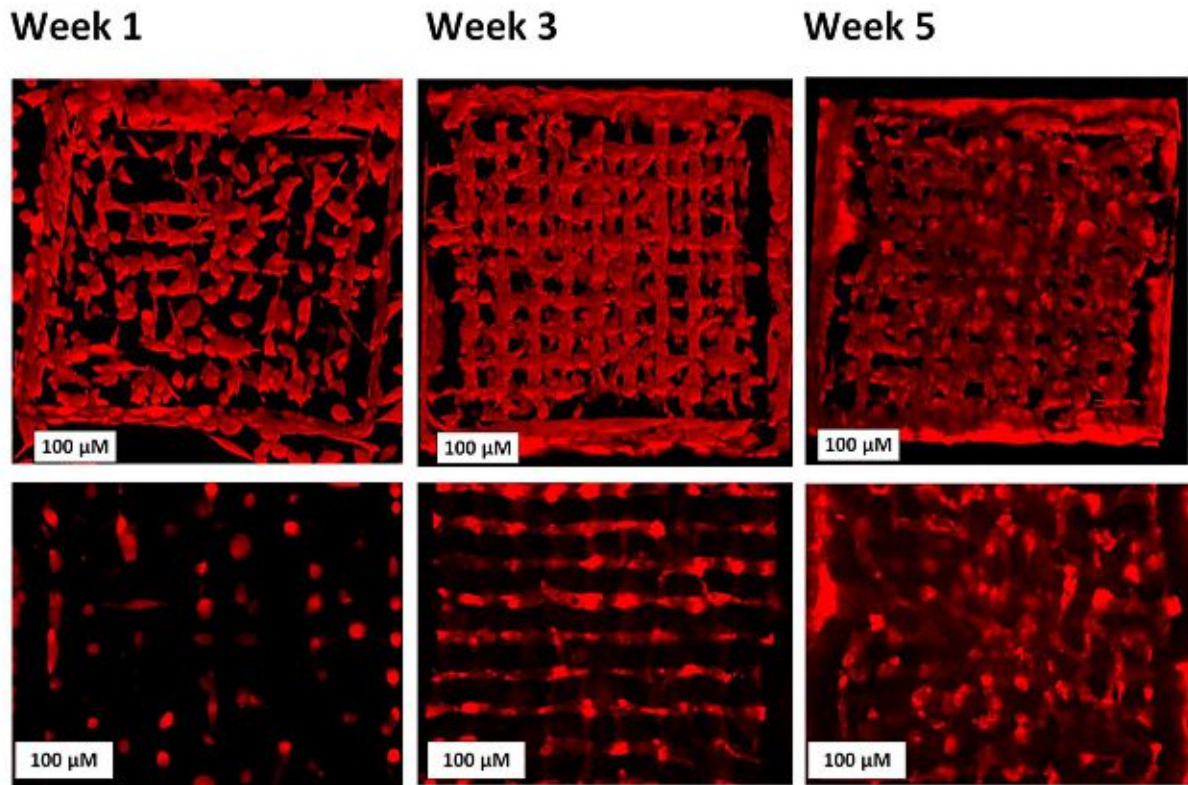


**Figure 29.** mCherry labelled L929 fibroblast cells embedded in 7.5 wt% GelNB hydrogels. The top row shows the 3D Z-stack of the fabricated hydrogels, while the bottom row displays a single layer of the structures. After one week the cells exhibited a rounded morphology throughout the structure. By week 3, the cells aligned along the fabricated channels and filled up the available space. Finally, after 5 weeks, the cells partially degraded the hydrogel and migrated into the crosslinked sections of the hydrogel as well.

### 2.3.5 Conclusion

The use of Gel-NB hydrogels with an appropriate photoinitiator enabled high-definition bioprinting. Due to the quasi-ideal behaviour and associated fast crosslinking kinetics of this material, a wide range of processing parameters (laser power and writing speed) is supported without a strong variation the mechanical properties of the produced hydrogels. Nevertheless, the degradation of the produced hydrogel constructs can be fine-tuned by varying the applied laser power. Close to the structuring threshold the properties of the cross-linked material can be controlled by only slight variations of exposure dose. This allows to produce 3D structures with controlled swelling behaviour

and gradients of mechanical properties. Our results demonstrate that within the used laser power range of up to 100 mW viability and proliferation of the cells embedded in the hydrogel did not vary. Compared to scaffold seeding a more uniform cell loading and higher cell densities can be achieved via high definition bioprinting regardless the pore size. Decoupling the possibility to produce small pores and constructs with complex high-resolution features from the cell-loading efficiency allows to design and execute systematic experiments on cell-material and cell-cell interactions in 3D for both developmental studies and disease progression models.

## 3 Applications

### 3.1 On-Chip High-Definition Bioprinting of Microvascular Structures

This chapter is submitted for publication and contains text from manuscript titled:

Dobos A, Gartner F, Markovic M, Van Hoorick J, Tytgat L, Van Vlierberghe S and Ovsianikov A On-Chip High-Definition Bioprinting of Microvascular Structures

*2020 Submitted to Biofabrication*

The voxel simulations were performed by F. Gartner (TU Wien).

### 3.1.1 Introduction

3D cell culture models that have the capacity to recapitulate the biochemical functionalities, mechanical properties and the microarchitecture of organs have been gaining increasing attention in biomedical research. These systems could provide more insight into the pathological and physiological functions of tissues compared to 2D cell cultures.<sup>128,132</sup> “Organ-on-chip” devices which integrate 3D cell culture techniques with microfluidic approaches could deliver an important platform to further improve *in vitro* organ and disease models.<sup>133,134</sup>

Several different polymers have been developed to home cells in 3D cell cultures, including nature-derived hydrogels and synthetic materials.<sup>39,128,135</sup> Natural hydrogels are physically or chemically crosslinked polymer networks which are capable of the uptake of large quantities of water without dissolving.<sup>135,136</sup> They are often derived from the non-cellular compartment of the tissues called the extracellular matrix.<sup>137</sup> Some of the commonly used ECM derived hydrogels include collagen, gelatin and hyaluronic acid.<sup>15,54,62,66,112,138–141</sup> The advantages of such materials include good biocompatibility, biodegradability and they often possess cell-responsive functionalities.<sup>39</sup> However, one of the main challenges in the use of such materials for biofabrication purposes includes the lack of control over the material properties due to the absence of (photo-)crosslinkable functional groups. Therefore, several different approaches have been developed to introduce reactive groups including (meth)acryloyl or thiol-ene functionalities to create networks following a chain- or step-growth polymerization approach.<sup>54</sup> Thiol-ene based step-growth polymerizations offer several advantages over the more traditional chain-growth hydrogels, such as the lack of oxygen inhibition and faster reaction kinetics enabling the reproducible production of 3D printed structures with high structural integrity at low light intensities.<sup>142</sup>

Although many different strategies have been developed to create biomimetic cell environments, one of the main challenges in tissue engineering and organ-on-chip devices remains the lack of vascularization in the fabricated 3D model.<sup>143,144</sup> The vast majority of tissues in the body depend on blood vessels to supply nutrients and oxygen to the cells as the diffusion limit for oxygen is approximately 100–200  $\mu\text{m}$ .<sup>145</sup> Microcirculation, based on the microvasculature, is the distal functional unit of the vascular system. The microvascular system consists of vessels with different



diameters including the arterioles ( $\pm 30\mu\text{m}$ ), venules ( $\pm 20\ \mu\text{m}$ ) and capillaries ( $< 8\ \mu\text{m}$ ).<sup>146,147</sup> Capillaries and venules are formed only by endothelial cells while arterioles also contain an additional layer of smooth muscle cells.<sup>147</sup> Tissues larger than a few hundred micrometres require the formation of new blood vessels by vasculogenesis and/or angiogenesis to supply the metabolic needs of the cells. Vasculogenesis is by definition the differentiation of a stem cell, precursor or angioblast while angiogenesis describes the process of remodelling and expansion where new vessels sprout from the already existing ones.<sup>148</sup>

There are multiple different approaches which have been developed to increase the vascularization of a tissue construct. Previous studies showed that the scaffold design including the provided pore size and degradability is crucial for the formation of a neovascular network.<sup>149,150</sup> The use of a supporting cell line co-cultured with endothelial cells also showed improved vascularization compared to a monoculture of endothelial cells. Supporting cells can be primary cells or cell lines including fibroblasts. Hepatocytes, adipose derived stem cells, mesenchymal stem cells or other cell types.<sup>151–155</sup>

There are several different ways how 3D vascular structures could be created inside the microfluidic chips.<sup>156</sup> One of the most widespread approaches are using a template (sacrificial) material, needles or rods during the channel production which could be removed at a later time point leaving a hollow channel to be seeded with endothelial cells.<sup>157,158</sup>

Bioprinting can provide a valuable toolset to engineer vascularized tissue and organ-on-chip models.<sup>159</sup> These constructs can be fabricated using two main tissue engineering approaches either using a scaffold-based or bottom-up technology.<sup>160–163</sup> In scaffold-based bioprinting, cells are either seeded or printed in a bioink matrix, while in bottom-up bioprinting usually cell-spheroids are used without any scaffold support. Although these approaches can provide a promising strategy to form neovascularized tissue models, they often lack the resolution to create channels in the microvascular range (under  $30\ \mu\text{m}$ ). To circumvent this drawback, high resolution additive manufacturing techniques including 2PP can be applied. The accuracy of the printed structures mainly depends on the voxels and their arrangement.<sup>164</sup>

### 3.1.2 Aim

The present work focuses on 2PP of microvascular structures directly on-chip using thiol-ene photo-click gel consisting of thiolated gelatin (Gel-SH) and gelatin-norbornene (Gel-NB). In order to demonstrate the ability of the employed material to support the spontaneous formation of vascular structures, a UV-induced (single-photon) encapsulation co-culture of human umbilical vein endothelial cells (HUVEC) with adipose derived stem cells (ASC/TERT1) was performed. This setting also allows to address the network forming capacity of the HUVECs spheroids compared to single cell suspension. In order to direct the alignment of HUVECs into vascular structures with various diameters resembling the diameters of the natural microvasculature, gelatin-based microvascular units were structured in the same material using 2PP. Two different approaches were explored; direct encapsulation of HUVECs spheroids into single microvascular units surrounded by the supporting cells, and the seeding of the endothelial cell spheroids into a microvascular barrier structure containing only the supporting cell line. The cell alignment was followed over 5 days via laser scanning confocal microscopy (LSM) in static and perfused culture and finally, the intercellular junctions were immunostained using an anti-VE-Cadherin stain.

### 3.1.3 Experimental

All chemicals, unless stated otherwise, were purchased from Sigma-Aldrich (Saint Luis, USA). The images were captured using a laser-scanning confocal microscope (LSM 800 Airyscan, Zeiss, Oberkochen, Germany).

#### 3.1.3.1 Cell Culture

ASC/TERT1 adipose derived stem cells (Evercyte, Vienna, Austria) were cultured in EGM-2 cell culture media (Lonza Group AP, Basel, Switzerland) supplemented with an additional 8% foetal bovine serum (FBS) to achieve 10% final concentration of FBS. Human umbilical vein endothelial cells labelled with red fluorescent protein (RFP-HUVEC) (PeloBiotech GmbH, Plantegg, Germany) were maintained in EGM-2 cell culture media supplemented with an additional 3% FBS to have a final concentration of 5%. All cell culture plastic flasks used for RFP-HUVECs were coated with quick coating solution (PeloBiotech GmbH) for 15 min before the seeding of cells. The cells



were sustained at 37 °C and 5% CO<sub>2</sub> incubator. When cells reached 90 % confluency, 0.5% Trypsin-EDTA was added for 3 min to detach the cells. The cells were then diluted with fresh cell culture media and placed in T75 flasks (Greiner Bio-1, Kremsmünster, Austria). RFP-HUVECs were used between passage 4 and 10.

### 3.1.3.2 *Two-Photon Polymerization Setup*

The setup is described in Chapter 2.1.3.5.

### 3.1.3.3 *Methylcellulose Preparation*

Methyl cellulose was sterilized by autoclaving before the addition of preheated EGM-2 medium at 60°C in the concentration of 1.2 w/v%. The solution was stirred with a magnetic stirrer for 20-30 min at room temperature, then for 2 hours at 4°C. Afterwards, the solution was centrifuged for 2 hours at 5000 g at 4°C. The supernatant was transferred to a new falcon tube and stored at 4°C. For further application, a 20 V% methyl cellulose solution in EGM-2 containing 5% FBS was used.

### 3.1.3.4 *Endothelial Cell Spheroid Formation*

Microtissues 3D Petri Dish 81-well micro-molds were used to form endothelial spheroids. 1 wt% agarose solution was prepared in sterile water and heated until it dissolved. Once it dissolved, the microtissue molds were filled up with agarose and left until it solidified. Afterwards, the agarose molds were equilibrated in PBS for at least 2 h in 12-well plates (Greiner-Bio, Kremsmünster, Austria) RFP-HUVECs were trypsinized with 0.5% Trypsin-EDTA to detach and centrifuged for 5 min at 170 g before resuspending it in 20% methylcellulose solution at a concentration of  $8.1 \cdot 10^4$  cells per 300 µL. 300 µL of cell solution was pipetted on top of each agarose mold and left to sediment for at least 15 min before the addition of 2 mL of 20% methylcellulose containing cell culture media. Spheroids were formed and used after 24 h.

### 3.1.3.5 *Synthesis of Gel-NB and Gel-SH*

The synthesis of Gel-NB was performed via reaction of 5-norbornene-2-carboxylic acid the primary amines of gelatin type B (kindly supplied by Rousselot, Ghent, Belgium) using EDC (1-ethyl-3-(3-dimethylaminopropyl)carbodiimide; NHS (n-hydroxysuccinimide; Acros, Geel, Belgium) coupling chemistry according to a previously reported protocol yielding a degree of substitution (DS) of 90% . The thiolated gelatin was prepared via reaction of the primary amines with D,L-N-acetylhomocysteine thiolactone yielding a DS of 63 % .<sup>112,113</sup>

### 3.1.3.6 *Functionalization of the high precision glass slides*

In order to improve the adhesion of the printed hydrogels on the chip, the 170 µm thick glass coverslips (IBIDI GmbH, Martinsried, Germany) were functionalised. To this end, they were plasma cleaned for 10 min. Subsequently, 10 vol% of (3-mercaptopropyl)trimethoxysilane was mixed with 85.5% ethanol and 4.5% deionized water and the plasma cleaned coverslips were submerged for 3 h at room temperature. Afterwards, the glass slides were washed three times with ethanol on both sides and were dried under nitrogen gas. Finally, they were placed in a heating chamber at 110 °C for 10 min. All functionalized coverslips were stored in ethanol until use.

### 3.1.3.7 *UV-Induced Cell Encapsulation*

Gel-SH and Gel-NB based hydrogels were prepared by dissolving them in phosphate buffered saline (PBS) in a 37 °C water bath. Once dissolved, the two components were mixed to achieve a final concentration of 5 wt% at an equimolar thiol/ene ratio. For the single cell suspension sample, RFP-HUVECs were trypsinized and resuspended in a final concentration of  $8.1 \times 10^5$  cells per mL together with a single suspension of ASC/TERT1 cell at a 1:1 ratio in respect of the cell number. The cell suspension was added to the hydrogel precursor solution together with 0.3 mM Li-TPO photoinitiator and 30 µL of the hydrogel mixture was pipetted on functionalized glass bottom dishes (IBIDI IBIDI GmbH) followed by 1 J irradiation at 365 nm.<sup>165</sup> For the spheroid experiments, RFP-HUVEC spheroids were removed from the mold and mixed with a single cell suspension of ASC/TERT1 cells in the above-mentioned concentration together with the hydrogel and 0.3 mM Li-TPO followed by 1 J irradiation at 365 nm.

Finally, EGM-2 5% FCS cell culture media was added to the hydrogel pellets. The hydrogel pellets were imaged for 5 days using LSM.

### 3.1.3.8 Dextran-FITC Perfusion

After 5 days, the cell pellets were cut in half with a scalpel and 0.5 mg mL<sup>-1</sup> 2000 kDa dextran-FITC (TdB Consultancy, Uppsala, Sweden) dissolved in cell culture media was added. The diffusion of the dextran was recorded using LSM 800 after 1 h of incubation at 37°C.

### 3.1.3.9 Voxel Simulation

Due to the nonlinear nature of 2PP, considerations regarding the shape and size of the voxel can be done with the help of the squared illumination point spread function,  $IPSF^2_{(x,y,z)}$ , which describes the intensity distribution around the focus.<sup>166</sup> To simulate the point-spread function  $IPSF^2$  for 2PP, the  $IPSF$  which describes one-photon absorption was first calculated with PSF Lab.<sup>167</sup> The simulations were done in the xz-plane for an air objective ( $n_1=1$ ) with a numerical aperture of 0.4 illuminated with a Gaussian beam propagating in z-direction with light polarized along the x direction at a wavelength ( $\lambda$ ) of 720 nm with a filling factor ( $\beta_G$ ) of 1. The coverslip was 170  $\mu\text{m}$  thick with a refractive index (RI) of 1.52 ( $n_2$ ). The simulated sample had a RI of 1.34 ( $n_3$ ). The  $IPSF^2$  was simulated for three different depths in the material. To calculate the  $IPSF^2$ , the value for each pixel of the resulting intensity profile was squared and plotted with an in-house developed python program.

The full width half maximum (FWHM) of the  $IPSF^2$  was calculated with the values of the  $IPSF$  from the PSF Lab simulations based on the FWHM of a gaussian function with

**Equation 3;**

$$FWHM_{IPSF^2} = FWHM_{IPSF} \frac{1}{\sqrt{2}} \quad (3)$$

To calculate the intensity in the focal plane ( $I_{\text{peak}}$ ), the laser pulse was assumed to be  $\text{sech}^2$  (squared hyperbolic secant) shaped and the peak intensity was calculated using

**Equation 4;**

$$I_{peak} = 0.88 \frac{P\pi(NA)^2}{R\tau_p\lambda^2} \quad (4)$$

with the average laser power (P) acquired with a powermeter, the numerical aperture (NA) of the objective, repetition rate (R) and the pulse duration ( $\tau_p$ ).

### 3.1.3.10 *Refractive Index Mismatch*

Differences in the refractive index of the immersion medium and the fabrication material lead to a shift in the depth of the focal spot. In addition, the actual voxel size will deviate from the theoretical one depending on the depth inside the sample resulting in a different size of the fabricated structure as anticipated based on the applied design. To compensate for this effect, the layer spacing was multiplied with a correction factor (c)

$$c = \frac{n_i}{n_m}$$

with  $n_i$  being the refractive index of the immersion medium and  $n_m$  the refractive index of the material.

### 3.1.3.11 *High-definition Bioprinting of Cell-Containing Constructs*

After functionalization of the glass coverslips, a self-adhesive 6 channel slide (sticky-Slide VI 0.4, IBIDI GmbH,) was mounted on the glass slide and was used immediately. The thiol-ene gelatin hydrogel was prepared by separately dissolving Gel-SH and Gel-NB in PBS at 37 °C. Once dissolved, the two components were mixed to achieve a final gelatin concentration of 7.5 wt% (1:1 thiol-ene ratio). The RFP-HUVEC spheroids were removed from the mold by pipetting and mixed with a single suspension of ASC/TERT1 cells in a 1:1 ratio to have a final concentration of approximately 81 spheroids and  $8.1 \cdot 10^5$  cells per mL ASC/TER1. Finally, 0.5 mM biocompatible diazosulphonate two-photon photoinitiator DAS was added and the bioink was pipetted on the chip (approximately 30  $\mu$ L).<sup>53</sup> After printing, EGM-2 with 5 % FBS cell culture media was added to the vessel constructs and the unpolymerized material was removed. Two days after printing, the samples were perfused with cell culture medium using a syringe pump (PHD Ultra, Harvard Apparatus, Cambridge, MA, USA) at a speed of 5  $\mu$ L  $\text{min}^{-1}$  for an additional 3 days before fixing the cells.

### 3.1.3.12 Immunostaining

At different time points after printing, the constructs were washed with PBS and fixed for 2 h with 4% Histofix (Carl Roth GmbH, Karlsruhe, Germany). Afterwards, the fixed structures were washed with PBS and permeabilized with 0.5% Triton-X in PBS for 10 min. The non-specific absorption of the antibodies was blocked by incubation in 1 wt% bovine serum albumin dissolved in PBS (PBS-BSA) for 15 min before the addition of anti-VE Cadherin antibodies (Thermo-Fisher, Waltham, MA, USA) in a 1:500 dilution for 2h at room temperature. Afterwards, the constructs were washed for 15 min with PBS-BSA before the addition of the Goat anti-Rabbit IgG Superclonal Secondary Antibody, Alexa Fluor 488 (Thermo-Fisher, Waltham, MA, USA) in a dilution of 1:1000 for 2 h. Next, the structures were washed again for 15 min with PBS-BSA before the addition of Hoechst 34850 (Invitrogen, Carlsbad, CA, USA) in a dilution of 1:100 in PBS-BSA for 1 h. The cells were imaged using the LSM 800.

### 3.1.4 Results and Discussion

Thiol-ene photo-click gelatin hydrogels already showed remarkably high processability, biocompatibility and supported the adhesion and proliferation of cells when used as a bioink for high definition bioprinting.<sup>142</sup> In order to assess the capacity of RFP-HUVEC to form preliminary vascular networks in a Gel-NB-Gel-SH hydrogel, the cells were first encapsulated via UV-induced crosslinking. To this end, (ASC/TERT1) were used in a 1:1 ratio to the HUVECs as supporting cells.

Previous studies have highlighted the importance of high initial cell loading and cell-cell contact for vascularization.<sup>168</sup> Therefore, two different settings, namely a single cell suspension and a spheroid culture of RFP-HUVECs were compared to investigate the influence of spheroid culture on network formation. The spheroids were obtained overnight after seeding the cells onto non-adhesive agarose molds and were encapsulated via UV encapsulation in 5 wt% Gel-NB-Gel-SH hydrogels at an equimolar thiol/ene ratio in the presence of 0.3 mM UV PI (i.e. Li-TPO-L) and the supporting cells. After UV encapsulation, the cells were imaged at different time points

using LSM. Due to the red fluorescent label, the RFP-HUVECS are visible without staining, while the supporting cells are not interfering with the imaging of the network. In both cases, the thiol-ene photo-click gel-NB-gel-SH showed good biocompatibility and supported cell survival and adhesion. Although the cells were characterized by a uniform cell distribution and good cell viability immediately after encapsulation, the single cell suspension didn't show any sign of interconnection between the cells after 5 days despite the fact that the cells exhibited an elongated morphology. After 5 days, the cell pellets were incubated with 2000 kDa dextran-FITC for 1 h to address whether larger molecules are able to diffuse into the hydrogel. After 1 h the signal of the FITC-dextran could only be detected up to 100  $\mu\text{m}$  from the edge of the hydrogel pellet (**Figure 30a**). The spheroid co-culture however, presented a higher degree of sprouting after 5 days of co-culture with ASC/TERT1 cells. These cells exhibited an extended morphology as well. After incubation with the dextran-FITC dye, it was possible to trace the fluorescence up to 800  $\mu\text{m}$  into the hydrogel pellet after 1 h (**Figure 30b**).

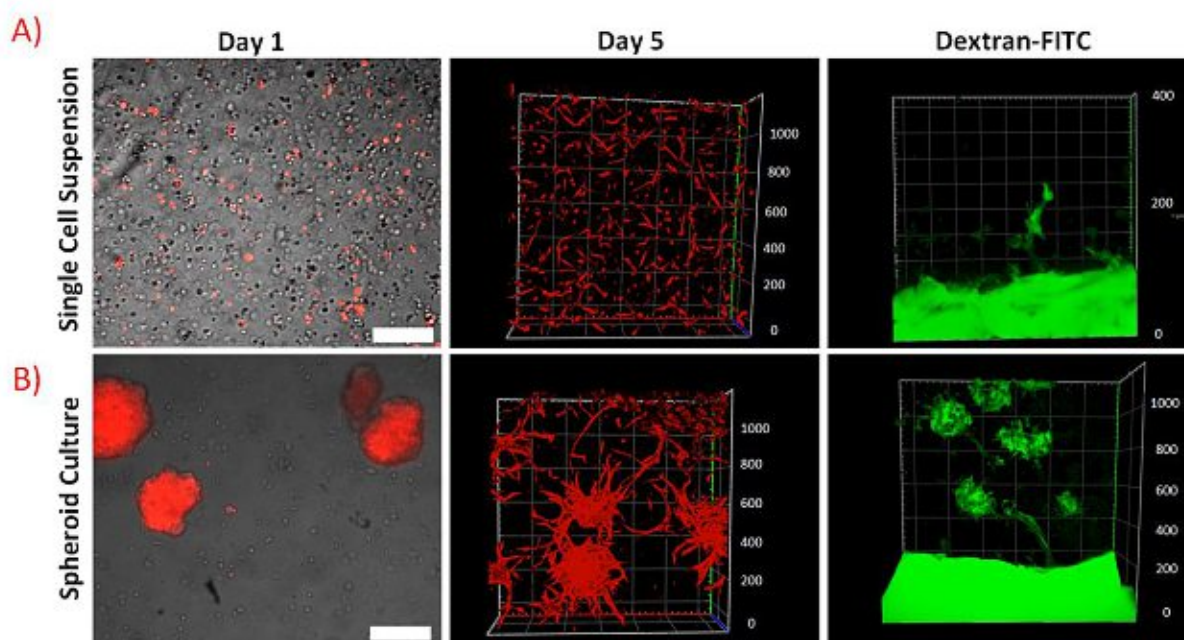


**Figure 30.** UV encapsulation of RFP-HUVEC and ASC/TERT1 cells in 5% Gel-SH and Gel-NB hydrogels. A) Single suspension of RFP-HUVECs and unlabelled ASC/TERT cells encapsulated at 1:1 ratio. The red fluorescent protein label allows the direct imaging of the cells without the need of further staining, while the ASC/TERT1 supporting cell line is only visible under bright field microscopy. After day 5 the RFP-HUVECs shows extended morphology, although the cells stayed as individual cells without the formation of a preliminary network. Upon incubation with 2000 kDa dextran-FITC, the dye was only able to diffuse into the the hdyrogel up to 100  $\mu\text{m}$  after 1 h. B) RFP-HUVECs spheroid co-culture with ASC/TERT1 supporting cells. After UV encapsulation the spheroids showed round morphology, however after 5 days the cells started to sprout from the shperoid towards each other showing a higher degree of interconnection within the hydrogel. When



incubating with 2000 kDA dextran-FITC the dye was able to penetrate the hydrogel up to 800  $\mu\text{m}$  after 1 h.

In order to fabricate reproducible organ- or tissue-on-chip models, having only microvascular network randomly distributed is often not satisfactory, as a precise positioning of the cells is also desired. However, most of the available biofabrication methods do not offer the resolution which allows the production of such small diameter round channels.<sup>26,108</sup> The accuracy of high-definition 3D printing depends on several different parameters which could be of crucial importance when producing small diameter round channelled structures.

In this respect, 2PP utilizes a femtosecond near infrared laser, where the dimensions of the polymerized volume pixel (voxel) have to be taken in account during the printing process. The shape of the voxel resembles a spinning ellipsoid with the z plane being larger than the x and y planes. The size of the voxel is dependent on the numerical aperture of the objective (NA), the refractive index of the material (RI) and the applied wavelength ( $\lambda$ ) as described by **equation 5** for the half-width-maximum (FWHM) of the voxel in the x,y-plane and **equation 6** for the z-plane.<sup>166</sup> Additionally, even a small difference between the RI of the (glass) substrate and the bioink can lead to spherical aberrations and which is mainly dependent on the difference in the refractive indices and the focusing depth.<sup>169</sup> In turn, these aberrations result in a decrease of the peak intensity in the focal plane and therefore to an inhomogeneous structuring at different printing depths.

$$FWHM_{x,y} = \frac{0.32\lambda}{\sqrt{2}NA} 2\sqrt{\ln 2} \quad (5)$$

$$FWHM_z = \frac{0.532\lambda}{\sqrt{2}} \left[ \frac{1}{RI - \sqrt{RI^2 - NA^2}} \right] 2\sqrt{\ln 2} \quad (6)$$

The spherical aberration of the voxel during structuring was modelled using PSF lab with a custom-made algorithm. **Figure 31A-C** shows the simulation of the illumination point-spread function (IPSF<sup>2</sup>) at different focusing depths. When structuring deeper



into the material the IPSF<sup>2</sup> gets distorted and its FWHM (**Table 1**) increases, showing a larger focus area which results in a lower peak intensity and photon density in the focal area.

**Table 1.** FWHM for x and z (beam propagation)-direction of the IPSF<sup>2</sup> at different depths in the bioink. The FWHM increases with higher structuring depths due to aberrations that lead to the deformation of the IPSF<sup>2</sup>.

Depth [ $\mu\text{m}$ ]	FWHM <sub>xy</sub> [ $\mu\text{m}$ ]	FWHM <sub>z</sub> [ $\mu\text{m}$ ]
0	0.731	7.628
100	0.734	7.856
400	0.903	14.949

During printing, the structures are formed by stacking of the voxels, therefore, their optimal arrangement is crucial for introducing high resolution features. The calculated voxel height of our setup is 8  $\mu\text{m}$  when using a gelatin hydrogel (RI of unpolymerized material: 1.34, NA of the objective: 0.4, structuring wavelength: 720 nm). For the voxel height compensation, a cube containing several different sized channels with diameters ranging between 10 to 30  $\mu\text{m}$  was designed (**Figure 31D**). This structure was either printed without voxel compensation (**Figure 31E**) or with a voxel compensation for 8  $\mu\text{m}$  (**Figure 31F**). As the smallest feature size of the designed CAD is almost the same size as the voxel itself, additional parameters have to be included in the software to be able to print such fine details. When slicing the object, some of the voxels would overlap and therefore block the previously printed channels. Therefore, a ratio of 0.8 was chosen, meaning that every voxel which overlaps the channel by 0.2 will be left out when processing the material. By adding this factor alone,

it was possible to print high-definition channels within the 180  $\mu\text{m}$  high cube.

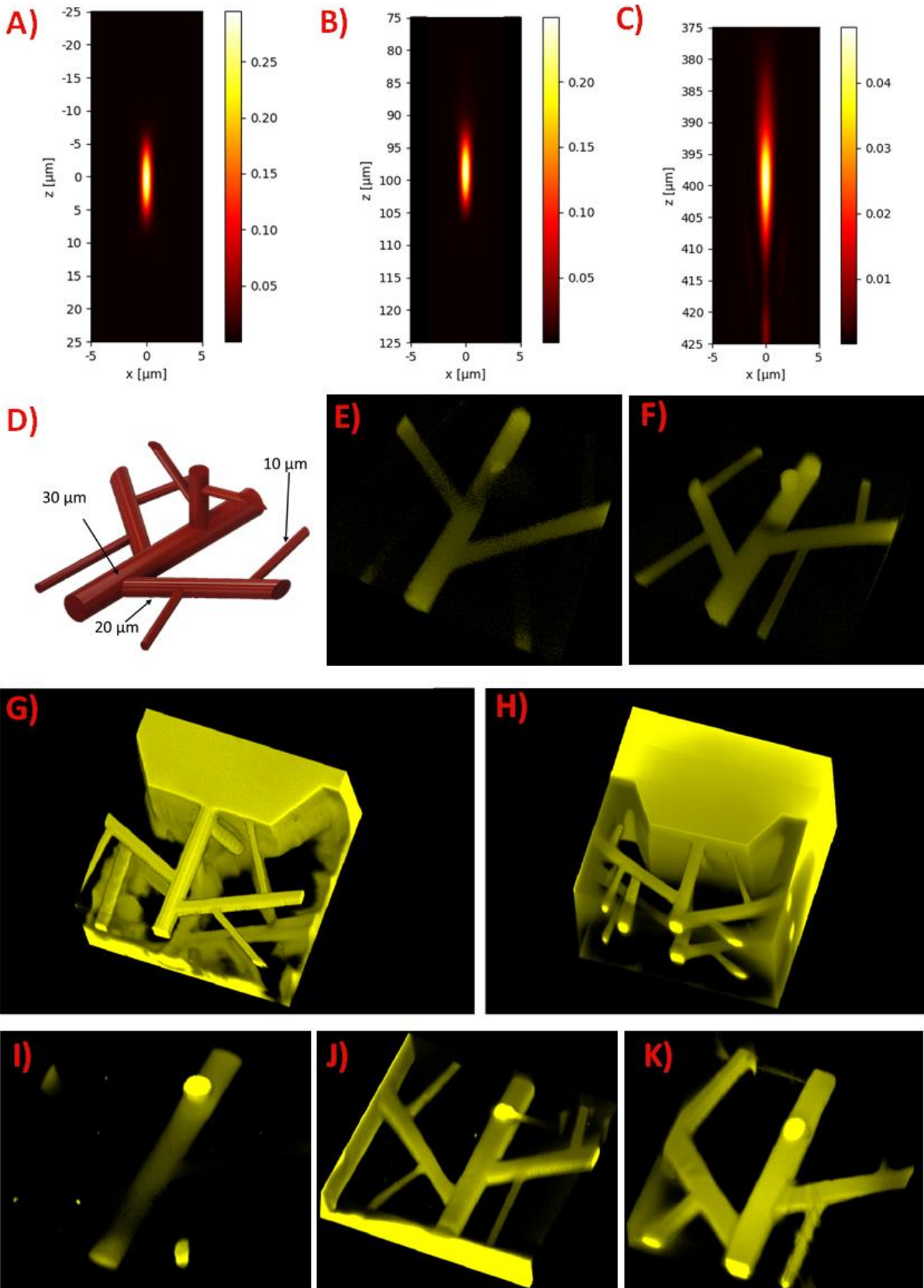


**Figure 31.** The accuracy and optimization of HD printing of small channelled structures. A-C) Simulation of the  $\text{IPSF}^2$  in the  $x,z$  plane for a  $\text{NA}=0.4$  air objective ( $n_1=1$ ) illuminated with light polarized along the  $x$  direction of a wavelength of  $\lambda=720\text{nm}$  with a filling factor  $\beta_G=1$ . The coverslip is  $170\ \mu\text{m}$  thick with a RI of  $n_2= 1.52$ . The sample has a RI of  $n_3= 1.34$ . The  $\text{IPSF}^2$  was simulated for three different positions in the material to show its distortion for increased structuring depths leading to a broader writing voxel and higher FWHM values. A)  $\text{IPSF}^2$  at the interface between coverslip and sample material at B)  $100\ \mu\text{m}$  and C)  $400\ \mu\text{m}$  depth in the sample material. D-F) Voxel compensation of the channelled structures of  $180\ \mu\text{m}$  height D) The designed CAD model containing round channels with different diameters ranging from  $10\text{-}30\ \mu\text{m}$ . E) Printed structure without voxel compensation F) with voxel compensation of  $8\ \mu\text{m}$ . G-H) Optimization of structures with a height of  $420\ \mu\text{m}$  G) Structures printed bottom-up, starting from the glass coverslip and H) same structures printed from top-down starting from the top of the microfluidic chip I-K) The effect of different layer spacings on the accuracy of the printed structure using  $70\ \text{mW}$  laser power and a voxel height of  $8\ \mu\text{m}$  I) with a layer spacing of  $0.5\ \mu\text{m}$  J) with a layer spacing of  $3\ \mu\text{m}$  K) layer spacing of  $9\ \mu\text{m}$ .

Although, the influence of spherical aberrations on voxel dimensions is negligible in smaller objects, it is more defined in higher structures as described in **Table 1**. Several previous studies indicated that by forming a physical gel before processing can improve the mechanical stability and influence the properties of gelatin-based hydrogels.<sup>54,170</sup> This phenomenon is attributed to an improved crosslinking efficiency, as upon physical gelation, interchain hydrogen bonds are formed in the gelatin backbone leading to semi-crystalline junction zones which can be partially locked by covalent crosslinks.<sup>123,171</sup>

Additionally, by printing from the cover glass into the material (bottom-up), the objective has to focus through multiple different RI material as the RI of the polymerised material differs from the unpolymerized one leading to additional refraction and diffraction of the light and further spherical aberrations, which in turn can result in a mechanically weaker and distorted structure. Therefore, the two different printing modes, bottom-up and top-down (starting from the top of the structure and printing towards the coverglass) were tested on physically gelated hydrogels using a  $430\ \mu\text{m}$  channelled structure. Our results indicated that by printing top-down, the accuracy of the structures can be improved (**Figure 31H**) when compared to a bottom-up printing approach (**Figure 31G**), possibly due to less scattering of the light and additional optical aberrations due the refractive index mismatch and because of the physical gelation, un-crosslinked material can provide support to the structures, thereby allowing top down structuring as this is not possible in liquid materials.

Previous studies has shown that the surface roughness and accuracy of the 2PP structures are highly dependent on the voxel overlap settings (layer spacing,  $dz$ ).<sup>164</sup> By increasing the overlap, surface roughness decreases thereby allowing the printing of well-defined features, however in turn it increases the structuring time and depending

on the material the density of the radicals in the focal point. By increasing the laser power, the voxel size also increases in all dimensions.<sup>172</sup> In order to test the power dependency of the overlap setting, the previously mentioned cube with different sized channels was printed at different powers (45 mW, 70 mW and 100 mW) and with increasing layer spacing from 0.5  $\mu\text{m}$  to 13  $\mu\text{m}$ . The ability to perfuse the produced channels was set as a quality threshold in regard of over-polymerization and mechanical stability. **Table 2** shows the used average powers ( $P_{\text{avg}}$ ) with calculated peak intensities ( $I_{\text{peak}}$ ) and the layer spacing ( $d_{z_{\text{th}}}$ ) at which the channels were first perfusable (not over-polymerized). Since the area within the FWHM is mainly contributing to induce 2PP<sup>164</sup>, the simulated FWHM<sub>z</sub> value at 100  $\mu\text{m}$  depth at which the intensity has fallen to half of its value, was used as reference value. For an intensity of 686  $\text{GW}/\text{cm}^2$ , z-distances between the voxels that were smaller than 25% of the FWHM<sub>z</sub> led to over-polymerization within the material, resulting in closed channels. This phenomenon was also observed at peak intensities of 1067  $\text{GW}/\text{cm}^2$  and 1524  $\text{GW}/\text{cm}^2$  for layer spacings of less than 38% and 89% of the FWHM<sub>z</sub>. When choosing small layer spacings, the number of voxels that overlap is increased and the structuring area is illuminated more often with the highly effective area around the focal spot, generating a higher number of radicals. Further, when structuring with smaller layer spacing it is possible that parts of the voxel reach into the channels. We hypothesise that these two effects lead to over-polymerization of the material within in the channels. When increasing the intensity, the voxel area that induces polymerization and the overlap region are growing which makes it necessary to increase the layer spacing. Figure 2 shows an example of over-polymerization at 70 mW with different layer spacings is visualized in **Figure31I – K** with **Figure31I** at 0.5  $\mu\text{m}$ , **Figure31J** at 3  $\mu\text{m}$  and **Figure31K** at 9  $\mu\text{m}$  overlap. By choosing the optimal layer spacing, the structuring time was reduced by 10-fold compared to previously reported protocols.<sup>53,142</sup> With a layer spacing of 0.5  $\mu\text{m}$  the CAD depicted of Figure 2D takes over 9 minutes to print, while when using a layer spacing of 5  $\mu\text{m}$  the same design takes less than 50 seconds.

**Table 2. Average powers, peak intensities, intensities at FWHM<sub>z</sub> and threshold layer spacings at different power settings.**

$P_{\text{avg}}$ [mW]	45	70	100
$I_{\text{peak}}$ [GW/cm <sup>2</sup> ]	686	1067	1524
$I_{\text{FWHM}}$ [GW/cm <sup>2</sup> ]	343	533	762
$dz_{\text{th}}$ [μm]	2	3	7

After optimization of the printing parameters of small channelled structures on chip, two different setups were created to test the vascular network formation of RFP-HUVECs. In the first setup, the single unit vessels (**Figure 32A**), were produced by embedding both the supporting cells (ASC/TERT1) and the RFP-HUVECs in the bioink containing 7.5 wt% of the Gel-NB-gel-SH hydrogel crosslinked with 0.5 mM DAS photoinitiator. During the printing process, a cube with a height of 180 μm and an internal channel structure was fabricated around the spheroid, positioning it in close proximity to the channels (**Figure 32B**). Based on the previous experiments, the printing parameters were set at a laser power of 70 mW and a layer spacing of 5 μm. In the second setting, cubes with internal channels with a height of 400 μm were printed across the whole microfluidic channel thereby creating a barrier structure using the previously mentioned bioink formulation (**Figure 32C**). In this case, only the supporting cells were embedded in the structure during the printing process, as the spheroids in the bioink are randomly distributed. Consequently, positioning them close to the channels is not possible during the printing process. However, once the printed structure was developed by washing away the unpolymerized material, the RFP-HUVECs spheroids were drop-seeded to the created barrier, thereby allowing the migration of the endothelial cells into the pre-created channels (**Figure 32D**).

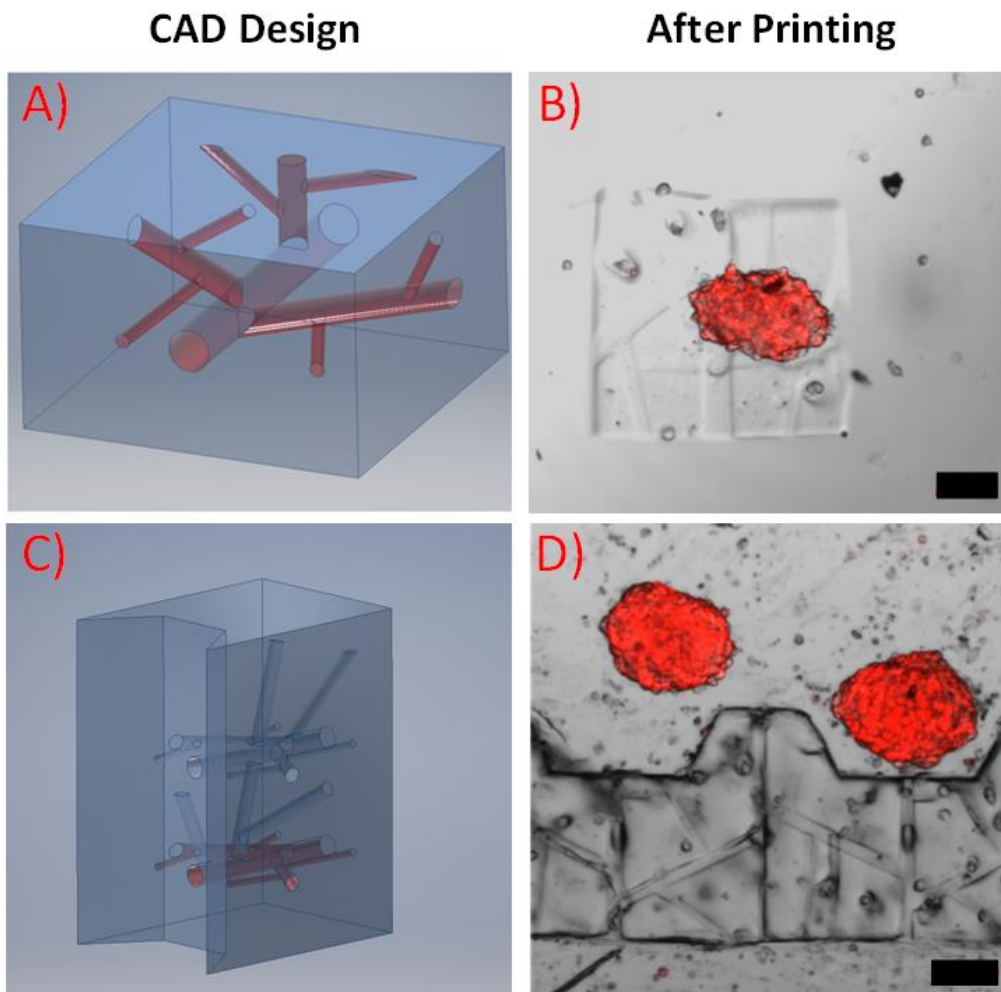


**Figure 32.** The two different chip setups tested for the vascular network formation of RFP-HUVECs. **A)** CAD design of a single unit vessel with a height of 180  $\mu\text{m}$ . **B)** The printed structure, where both the supporting cells and the RFP-HUVECs were embedded in the hydrogel. **C)** CAD design of a vessel barrier with a height of 400  $\mu\text{m}$ . **D)** Only the supporting cells were embedded during the printing procedure and spheroids were added after developing the structure. The scale bars represent 100  $\mu\text{m}$ .

The printed structures were first incubated under static condition for two days before the samples were perfused using a syringe pump at a flow rate of  $5 \mu\text{L min}^{-1}$  for an additional three days. Next, the samples were fixed and co-stained with Hoechst 34850 and vascular endothelial cadherin (VE-Cadherin). Cell adhesion molecules are very important regulators in the initiation and maturation of neovascular networks during angiogenesis.<sup>173</sup> They are responsible for the formation of intercellular junctions between the endothelial cells, which are crucial to control the diffusion and transport of molecules and the endothelial surface polarity.<sup>174</sup> Previous studies have shown that VE-cadherin is the major endothelial specific cell adhesion molecule involved in vascular morphogenesis and growth control.<sup>175</sup> Even after two days of culture, the



endothelial cells exhibited an extended morphology and were expressing VE-Cadherin at the barrier (**Figure 33, first row**) as well as the single unit structure (**Figure 33, second row**). As the endothelial cells were labelled with a red fluorescent protein, there was no need for further cell stains to visualize the cell body and morphology. The nuclear stain suggested cells both within the cube and also in the channels of the 3D printed constructs.

After day 5, the static culture vessels showed less cells in both the barrier and single unit vessels, especially in the crosslinked regions when compared to the perfused culture according to the Hoechst staining, possibly due to the lack of constant nutrient supply and removal of metabolites. Additionally, the VE-Cadherin expression was more pronounced in the perfused culture as well, although the cell morphology remained extended in the static culture as well.



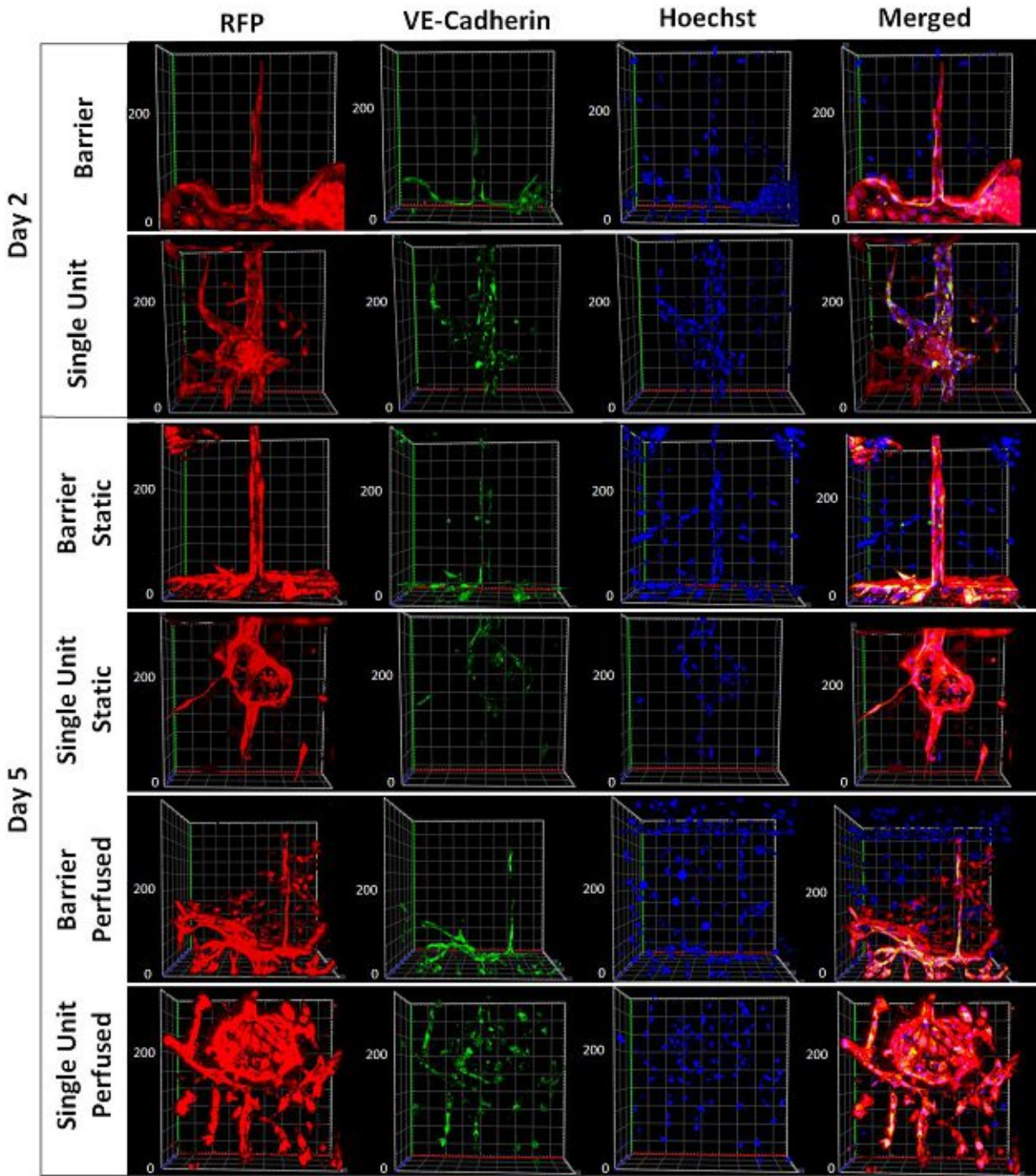


**Figure 33. Immunostaining of vascular structures under different culturing conditions. The endothelial cells are visible via the red fluorescent protein label (RFP). The cells showed extended morphology even after two days post-printing. The endothelial vascular cadherin (VE-Cadherin) staining showed intercellular junction formation in all examined samples, however after 5 days it was more pronounced at the perfused culture compared to the static samples. The cell nucleus was stained with Hoechst 34850, showing higher number of cells in the perfused culture compared to the static ones.**

### 3.1.5 Conclusion

We have demonstrated the capacity of gel-NB-gel-SH thiol-ene photo-click hydrogels to support endothelial cell adhesion and proliferation both in a single cell suspension and spheroid culture via UV encapsulation. Due to the more pronounced cell-cell interactions, the spheroid culture proved to be more efficient in network formation compared to the single cell suspension approach. A wide range of processing parameters were tested on small diameter channel structures in order to improve both the accuracy and the throughput of the printing process. The spherical aberrations caused by the refractive index mismatch and the focusing depth was modelled by a custom-made algorithm, and the effect of the voxel compensation was demonstrated. Additionally, the two different printing modes, the top-down and bottom-up approach were compared to further optimize the resolution of high structures. Different voxel overlaps and their dependency on the applied laser powers were compared both in terms of accuracy and also for the improvement of the structuring time. Finally, the capacity of 2PP to create vascular structures within a microfluidic chip was tested with two different settings, first as a one-pot method, including both the supporting cells and the endothelial cell spheroids in the bioink, and as a supporting cell scaffold barrier to drop-seed the HUVECs spheroids after developing the structures. The functionality of the formed vessels was demonstrated with immunostaining of VE-Cadherin endothelial adhesion molecules in both static and perfused culture. This chip could provide a useful tool to further study vascularization and angiogenesis and could be used to improve our knowledge about microcirculation.

## 3.2 Glioblastoma-on Chip

This chapter is based on and contains text from Marshall Plan Foundation Grant Report titled “3D Printed Blood-Brain Barrier-on-a-Chip”.

### 3.2.1 Introduction

Glioblastoma multiforme (GBM), originated from glial cells in the brain, is the most frequent brain tumour (representing 80% of primary malignant central nervous system (CNS tumours) with high mortality and recurrence rate, and median overall survival rate of 12-18 months after diagnosis.<sup>176</sup> The most commonly used therapy to treat GBM includes a surgical resection of the tumour with subsequent treatment with radiotherapy and chemotherapy using temozolomide (TMZ). However, this treatment scarcely increases the median survival rate as the removal of the primary tumour without damaging the brain is often not easy due to infiltrating cells in the healthy tissue.<sup>177</sup> Some of the other possible treatments or approaches under development include targeted therapy of the cancer, immunotherapy, antiangiogenic drugs, nanotherapy, gene therapy and electromagnetic radiation.<sup>178</sup> There are several challenges to face when developing more efficient treatments for GBM. There are only a very few available *in vitro* models of GBM to study the disease progression and develop new therapies.<sup>179</sup> Most of the preclinical studies are carried out by using rodent models, which as discussed earlier, often does not represent the human conditions efficiently. Additionally, the drug delivery strategies need to be improved as the blood-brain barrier (BBB) often poses a barrier, which prevents the intravenously or orally taken drugs to reach their target. BBB is a selectively permeable interface which separates the blood from the brain parenchyma. BBB is composed of brain endothelial cells in the cerebral microvasculature. The BBB is characterized by tight junction which leads to the formation of a capillaries which are up to 100 times tighter than peripheral microvessels. On the other side of the capillary different glial cells such as astrocytic glia cell and pericytes are present.<sup>180</sup> Their influence on the BBB has been demonstrated by implanting astrocytes to other sites with leaky vessels and they induced the tightening of the endothelium.<sup>181</sup> Between the endothelial cells and the astrocytes, a basement membrane with embedded pericytes can be found which consists of extracellular matrix elements such as collagen, elastin, laminin, fibronectin and proteoglycans.<sup>182</sup> This barrier has an important role to protect the brain from possibly toxic substances while maintaining the exchange of nutrients, gases, and metabolites between the blood and brain. Small molecules can diffuse through the barrier without restrictions while larger molecules need to be transported across the membrane.<sup>183</sup> Therefore the modelling of the BBB is highly important for screening

potential drug candidates for the treatment of diseases of the CNS including GBM and to study the *in vitro* drug transport across the BBB.<sup>184</sup> The disruption of the BBB can be found in multiple diseases including stroke, multiple sclerosis, encephalitis, brain tumours, and Alzheimer's Disease.<sup>185</sup>

*In vitro* BBB models can provide valuable tools to study the physiological function and disease progression. These microfluidic based designs can implement physiologically relevant pressure and shear stress. Most of the chip designs used for BBB models in literature are based on polydimethylsiloxane PDMS devices incorporated with porous transwell membranes. Booth et al. used a co-culture of mouse endothelial cell line b.End3 together with C8-D1A astrocytes on a 10  $\mu\text{m}$  thick polycarbonate membrane with 0.4  $\mu\text{m}$  pore size, and they found that the trans-endothelial electrical resistance (TEER) exceeded the monoculture of endothelial cells when co-culture was used and the tight junction formation was clearly visible.<sup>186</sup> Griep et al. used a similar PDMS device together with a transwell membrane with smaller pore size (8 $\mu\text{m}$ ) coated with collagen and seeded with human brain endothelial cells (hCMEC/D3).<sup>187</sup> Kim et al. presented a collagen-based microvasculature model using microneedles and 3D printed frames. The created hollow tubes were seeded with bEnd.3 mouse cell line to create the BBB. They were able to cultivate the cells for 14 days.<sup>188</sup> A modular approach where the endothelial and the neuronal chambers can be cultivated separately and assemble at a later time point was demonstrated by Achyuta et al.<sup>189</sup> Ma et al. and co-workers fabricated BBB chips employing low-stress silicon nitride membranes with 400  $\mu\text{m}$  pores produced by either a lithographic stepper or an electron beam lithography system and was further modified by spinning collagen type I onto the membrane to improve cell attachment. This membrane was later seeded with primary rat astrocytes on one side and immortalized brain capillary endothelial cell line SV-HCEC on the other side to study the contribution of the different cells to the resistance of the fabricated membrane.<sup>190</sup> Brown et al. has designed a NeuroVascular Unit (NVU) to recapitulate the function of the BBB. The NVU was produced by three PDMS layers separated with polycarbonate membrane with 0.2  $\mu\text{m}$  pore size. The membranes were coated with laminin prior cell culture use. Primary human brain-derived microvascular endothelial cells (hBMVEC), primary astrocytes and pericytes and human induced pluripotent stem cells (hiPSCs) differentiated into human cortical glutamatergic neurons were used throughout the experiments. They were able to maintain cell



viability on the chip for over 2 weeks of culture. They compared the effect of different cell culture media and flow to improve to tight junction formation of the endothelial cell layer and examined the transport of different sized molecules across the membrane.<sup>191</sup> Deosarkar et al. has employed a PDMS device and replaced the standard polycarbonate membranes by producing a series of 3  $\mu\text{m}$  pores along the vascular channels to create a dynamic neonatal BBB on a chip. Neonatal rat brain capillary endothelial cells (RBEC) and primary cultures of neonatal rat astrocytes were seeded on the fibronectin coated device and were cultured for 5 days. Their results showed that the permeability of their chip was significantly lower compared to conventional transwell BBB models.<sup>192</sup> Wang et al. differentiated hiPSCs into microvascular endothelial cells and co-cultured them together with rat primary astrocytes. They have evaluated the transport of several different sized molecules and drugs such as caffeine, cimetidine, and doxorubicin.<sup>193</sup>

Although there are multiple relevant BBB models available in literature to study drug transport through the BBB, only a very few GBM-on-chip devices were reported which could be used to evaluate the efficiency of the possible treatments. M. Akay and co-workers have produced brain cancer chips using two U-87 and primary, tumour-derived human GBM cells to create high throughput drug-screening platforms.<sup>194,195</sup> Ayoso et al. used U-251 GBM cells encapsulated into a collagen hydrogel inside a SU-8 device resin via photolithography, however, these first approaches did not provide an endothelial layer to mimic the complexity of the BBB.<sup>196</sup> A recently published GBM-on-chip from Yi et al. employed bioprinting to create a highly biomimetic model. Patient-derived GBM cells were used to form spheroids and were embedded in brain decellularized ECM (BdECM). After the GBM cells were printed, a vascular bioink containing HUVECs embedded in BdECM were printed around the GBM to establish a vessel barrier. They have found that the patient specific cells produced different responses to the different drugs and drug combinations.<sup>197</sup>

### 3.2.2 Aim

The goal of the project was to establish a physiologically relevant blood-brain-barrier model and create a glioblastoma-on-a-chip device. A microfluidic chip using a medical grade mold material and the printing of a biodegradable and biocompatible membrane via 2PP was established. Different cells, both on the “blood” and the “brain”

compartments of the chip can be drop-seeded and perfused with their corresponding media separately. The formation of an endothelial monolayer and the cell viability of the cells in the “blood” compartment was addressed using live/dead staining, and immunohistochemical stainings using vascular endothelial cadherin (VE-Cadherin) and zona occludin-1 (ZO-1) for the visualization of adherens and tight junctions. Additionally, the diffusion of different sized water-soluble molecules (FITC-albumin, 4 kDa FITC-dextran, fluorescein and riboflavin) was tested on the 3D printed membrane additionally to the contribution of cells on the diffusion rate. The biocompatibility of different materials for GBM spheroid encapsulation was also tested. The spheroids were treated with different drugs and their viability was evaluated by live-dead, apoptosis and proliferation staining. The schematic representation of the chip is depicted in (Figure 34).

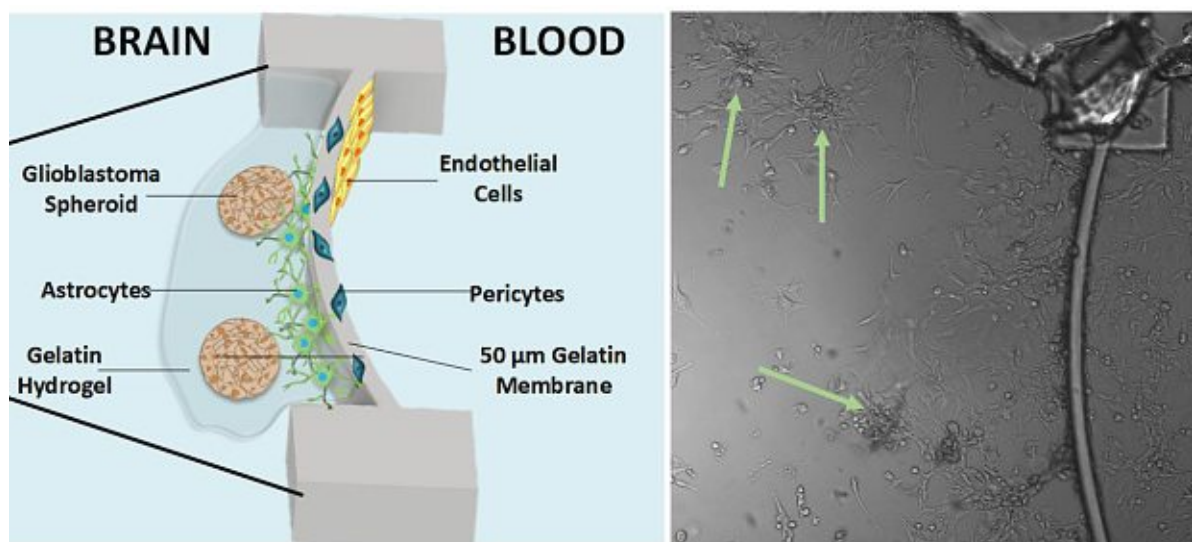


**Figure 34. GBM-on-chip.** On the left side the schematic image of the setup with the different cell types. On the right side the created chip, the green arrows are pointing at the glioblastoma spheroids.

### 3.2.3 Experimental

All materials and chemicals are from Sigma Aldrich (St. Louis, Missouri, USA) unless stated otherwise. Graphs were plotted using GraphPad Prism 6.

#### 3.2.3.1 Glass Functionalization

The glass slides were functionalized with thiol groups according to the previously mentioned protocol described in Chapter 3.1.3.6.



### 3.2.3.2 *Microfluidic Chip Production*

The microfluidic chip was produced by adhering two previously functionalized glass slides, one with a thickness of 1 mm and one high precision 170  $\mu\text{m}$  thick (Ibidi GmbH, Martinsried, Germany) together with a double sided tape with two different heights (referred to as mold material) (Provided by the Lab-on-a-Chip Systems in Bioscience Technology group at TU Wien) (Adhesive Research, Glen Rock, Pennsylvania, USA). The glass slides were functionalized with thiol groups according to the previously mentioned protocol. The mold material is a medical grade double-sided pressure sensitive adhesive tape with the height of approximately 140 or 81  $\mu\text{m}$ . The adhesive tape was cut according to the CAD to create the X shaped microfluidic chips using an XY plotter (Camm-1 GS-24, Roland DG, Hamamatsu, Japan). The connections for the ports were created by drilling the holes into the thick glass cover slide prior to the chip assembly using a micro drill (TBM220 Typ 28128, Proxxon GmbH, Radingdorf, Germany). The protecting foil was removed from the adhesive tape and the two glass slides were bonded together. As connectors, 20-gauge bund needles were glued onto the glass using a two-component epoxy glue (Klebfix, Dip-tools, Stuttgart, Germany). For additional strength and isolation two component dental glue (Twinsil, Picodent, Wipperfürth, Germany) was applied.

### 3.2.3.3 *Material Synthesis*

Gel-NB with a DS of 90% and 53% was synthesized according to a previously reported protocol (Chapter 3.1.3.5).

### 3.2.3.4 *Laser Setup*

The detailed description of the used setup is described in Chapter 2.1.3.5.

### 3.2.3.5 *Cell Culture*

Several different primary cells and cell lines were used for the testing of the printed barrier model. For the preliminary studies using the 81  $\mu\text{m}$  mold, HUVECs and RFP-HUVECs were used at the “blood” compartment of the chip to create an endothelial cell layer on the membrane. The cells were cultivated in EGM-2 media supplemented with 5% FBS. 50B11 nociceptive dorsal root ganglion sensory neuronal line (provided by University of California) were used on the “brain” compartment of the chip for the preliminary experiments. The cells were maintained in neurobasal cell culture media

with 10% FBS. For the GBM-on-chip construct using the 140  $\mu\text{M}$  mold, human blood brain barrier endothelial cell line (hCMEC/D3) (provided by Prof. Neuhaus from the Austrian Institute of Technology, Vienna) were used at the “blood” compartment of the chip. The cells were cultivated in endothelial cell medium (Lonza Group AP, Basel, Switzerland) (Promocell, USA) supplemented with 5% FBS and used between passage 25-40. Human primary astrocytes (provided by Austrian Institute of Technology) were used on the “brain” compartment of the chip and maintained astrocyte media (ScienCell, Carlsbad, USA) with 2% FBS (ScienCell, Carlsbad, USA), 1% of penicillin/streptomycin (ScienCell, Carlsbad, USA) and 1% astrocyte growth supplement (ScienCell, Carlsbad, USA). Human primary pericytes (provided by Austrian Institute of Technology) were maintained in pericyte media (ScienCell, Carlsbad, USA) with 2% FBS (ScienCell, Carlsbad, USA), 1% of penicillin/streptomycin (ScienCell, Carlsbad, USA) and 1% pericyte growth supplement (ScienCell, Carlsbad, USA). U-87 glioblastoma cell line was maintained in Eagle’s minimum essential media (EMEM) media supplemented with 2mM glutamine, 1% non-essential amino acids, 1mM sodium pyruvate, 1% penicillin-streptomycin and 10% FBS. All cells were cultivated at 37 °C and 5% CO<sub>2</sub> incubator. Upon 90% confluency, the cells were detached using accutase solution and were centrifuged at 170 g for 5 min before plating them onto T75 flasks. The flasks were coated with quick coat solution for the endothelial cells, and poly-D-lysine solution for the primary astrocytes and pericytes.

#### 3.2.3.6 *3D Printing of the Barrier-on-Chip*

For the barrier printing, Gel-NB with a degree of substitution of 90% was dissolved in PBS in a 37 °C water bath to obtain a final concentration of 7.5 wt %. After it completely dissolved, the hydrogel was supplemented with 0.5 mM of 2PI DAS and DTT at an equimolar thiol-ene ratio were added at last. For direct embedding of human primary pericytes different concentrations of cells (1 or 2 million per mL) were added to the bioink. Finally, the obtained solution was pipetted into the assembled microfluidic chips, and was left to form a physical gel at room temperature for 15 min or were placed in 8 °C prior printing. Once the gel was formed, a membrane was printed according to the CAD to create a barrier between the two chambers of the X chip using a laser power of 75 mW and a writing speed of 1 m s<sup>-1</sup> with a hatch of 0.5  $\mu\text{m}$  and layer spacing of 2  $\mu\text{m}$ . The samples were developed by placing the microfluidic chips into a 37 °C incubator. After 15 min incubation, the unpolymerized material was removed by a

vacuum pump, and PBS or cell culture media were added to the two different chambers of the chip. The integrity of the printed structures was tested by adding 2000 kDa FITC-dextran (TdB Consultancy, Uppsala, Sweden) to one side of the chip, which should not diffuse into the material, therefore the fluorescence should be restricted to the chamber where it was added.

#### 3.2.3.7 *Cell Seeding*

After the membrane barrier was printed and developed, it was equilibrated in cell culture media for at least 2 h prior to the cell seeding. First, the cells for the brain compartment of the chip were detached by accutase and the cells were centrifuged for 5 min at 170 g before resuspending it in the concentration of 1 million per mL. The cells were seeded onto the membrane and were left to adhere for 1 h. For the “blood” compartment endothelial cells were drop-seeded onto the membrane and were left to adhere for 1 h. The diffusion of different molecules was tested 2 days after seeding.

#### 3.2.3.8 *FITC-Dextran Diffusion*

The integrity of the printed membrane was tested with 2000 kDa dextran-FITC (TdB Consultancy, Uppsala, Sweden) dissolved in PBS at a concentration  $0.5 \text{ mg mL}^{-1}$ . The diffusion of 70 kDa FITC-dextran, 4 kDa FITC-dextran, FITC-albumin (0.66 kDa), riboflavin (0.38 kDa) and fluorescein (0.4 kDa) molecules using the same concentration were recorded using LSM 800 at 37 °C. ImageJ software was used analyze the fluorescence intensity in the different compartments of the chip.

#### 3.2.3.9 *Degradation of the hydrogel membrane*

The degradation of the membrane was performed using collagenase from *Clostridium histolyticum*. The printed membrane was incubated in PBS overnight at 37 °C to reach equilibrium swelling. Afterwards, 1 CDU/mL collagenase solution was added and time lapse Z-stacks of the membrane degradation was recorded with LSM.

#### 3.2.3.10 *Live-Dead Staining and Immunostaining*

In order to assess the cell viability after drop-seeding, the cells were stained with Calcein AM/Propidium iodide (PI) live-dead staining according to previously mentioned protocol (Chapter 2.1.3) and was added to the microfluidic chip. The cells were imaged using LSM 800. The number of dead and alive cells was counted manually.

For the immunostaining, the cells on the chip were fixed with 4% Histofix (Carl Roth GmbH, Karlsruhe, Germany) for 1 h at different time points. Next, the cells were washed with PBS twice. The permeabilization was accomplished by incubating the samples with 0.5% Triton-X dissolved in PBS for 15 min. As a blocking solution in 1 wt% bovine serum albumin was dissolved in PBS together with 0.05% Tween-20 (PBS-BSA-Tween20). After permeabilization, the non-specific binding was blocked by incubating the cells with PBS-BSA-Tween20 for 15 min before the addition of anti-ZO-1 antibody (Thermo-Fisher, Waltham, MA, USA) at the dilution of 1:200 overnight at 8 °C. Afterwards, the constructs were washed three times before the addition of the secondary antibody labelled with Alexa Fluor 647 (Thermo-Fisher, Waltham, MA, USA) in a dilution of 1:1000 for 1 h. Next the structures were washed with PBS-BSA for 15 min before the addition of anti-VE Cadherin antibody (Thermo-Fisher, Waltham, MA, USA) in a dilution of 1:200 overnight at 8 °C. Afterwards, the constructs were washed three times with PBS-BSA before the addition of the secondary antibody labelled Alexa Fluor 488 (Thermo-Fisher, Waltham, MA, USA) in a dilution of 1:1000 for 1 h. Next, the structures were washed again for 15 min with PBS-BSA before the addition of DAPI in a dilution of 1:500 in PBS-BSA for 1 h.

#### 3.2.3.11 *Glioblastoma Spheroids*

Microtissues 3D Petri Dish 256-well micro-molds were used to form glioblastoma spheroids. The agarose was prepared according to previously described protocol (Chapter 3.1.3.4). U-87 cells were detached with accutase and centrifuged for 5 min at 170 g before resuspending it in cell culture media at different concentrations. 300  $\mu$ L of cell solution was pipetted on top of each agarose mold and left to sediment for at least 15 min before the addition of 2 mL of cell culture media. Spheroids were formed and used after 48 h.

#### 3.2.3.12 *GBM-on-chip Assembly*

Gel-NB with a DS of 53% were dissolved in PBS to achieve a final concentration of 5 wt%. Spheroids were removed from molds and were centrifuged and resuspended in approximately 2 molds per 100  $\mu$ L of hydrogel solution. The hydrogel was supplemented with 0.3 mM Li-TPO-L and equimolar concentration of DTT and was pipetted to the brain compartment of the chip. The UV gel was exposed to UV light for 5 min and afterwards fresh media was added. The glioblastoma spheroids were added

to the chip after 2 days of seeding of endothelial cells and astrocytes. The control hydrogels without BBB the spheroids were encapsulated in the hydrogel without the printed membrane in an 8-well chamber.

### 3.2.3.13 *Glioblastoma treatment*

24 h after assembling the GBM chip different types of treatments were tested. temozolomide (TMZ), roscovitine (RV), and the combination of both in concentration of 100  $\mu$ M each were added to the blood compartment of the chip. Both of the drugs were dissolved in DMSO at 10 mM concentration. After 24 h the drugs were removed and fresh media was added for another 24 h before the samples were stained.

### 3.2.3.14 *Ki-67 and Caspase Staining*

24 h after treatment the cells were incubated with Image It live caspase stain (Thermo-Fisher, Waltham, MA, USA), according to the protocol of the manufacturer for 3 h prior to fixing the cells and spheroids on the chip. Afterwards, the cells were permeabilized by using 0.5 % Triton-X dissolved in PBS for 15 min. After permeabilization, the non-specific binding was blocked by incubating the cells with PBS-BSA-Tween20 for 30 min before the addition of anti-Ki-67 antibody at the dilution of 1:250 overnight at 8 °C. Finally, the nucleus of the cells was stained with DAPI in a dilution of 1:500 in PBS-BSA for 1 h.

## 3.2.4 Results and Discussion

Most of the currently available BBB models almost exclusively rely on the use of PDMS devices. PDMS is a polymer widely used in soft lithography to produce a mold of the mold which can later be bound to glass surfaces after plasma treatment. The main advantages of PDMS include that it is transparent at the 240 nm – 1100 nm range and has a low autofluorescence allowing the optical imaging of the device, it is biocompatible and gas permeable, and has a relatively low cost.<sup>198,199</sup> However, it is known that PDMS can absorb certain small molecules and incompletely crosslinked PDMS could leach into the created channels which could alter the results of the experiments.<sup>200,201</sup> Our aim was to employ a pressure sensitive adhesive double-sided tape to cut out the desired geometry and adhere it in between glass slides. This medical grade film has a height of 81  $\mu$ m or 140  $\mu$ m and contains an inert, non-migratory acrylic adhesive to ensure the attachment to the glass. An X geometry was

cut out of the adhesive film in order to have separated compartment after printing of the membrane. The high precision 170  $\mu\text{m}$  thick glass bottom of the chip allows both the high-definition 3D printing of the barrier directly on the chip and also the optical imaging of the chip afterwards. The holes for the ports were drilled into the top glass microscope slide (**Figure 35a**). Once the chip is assembled, the reservoirs and connectors can be glued onto the top glass using a dual component, water resistant epoxy glue which cures at room temperature in 1 h (**Figure 35b**). Two different components were used, for the blood compartment a bunt needle was glued to allow the perfusion of the system, while for the brain compartment, which needs to be cultured under static environment, a closable reservoir was attached to maintain sterile cell culturing condition and enable easy media exchange.

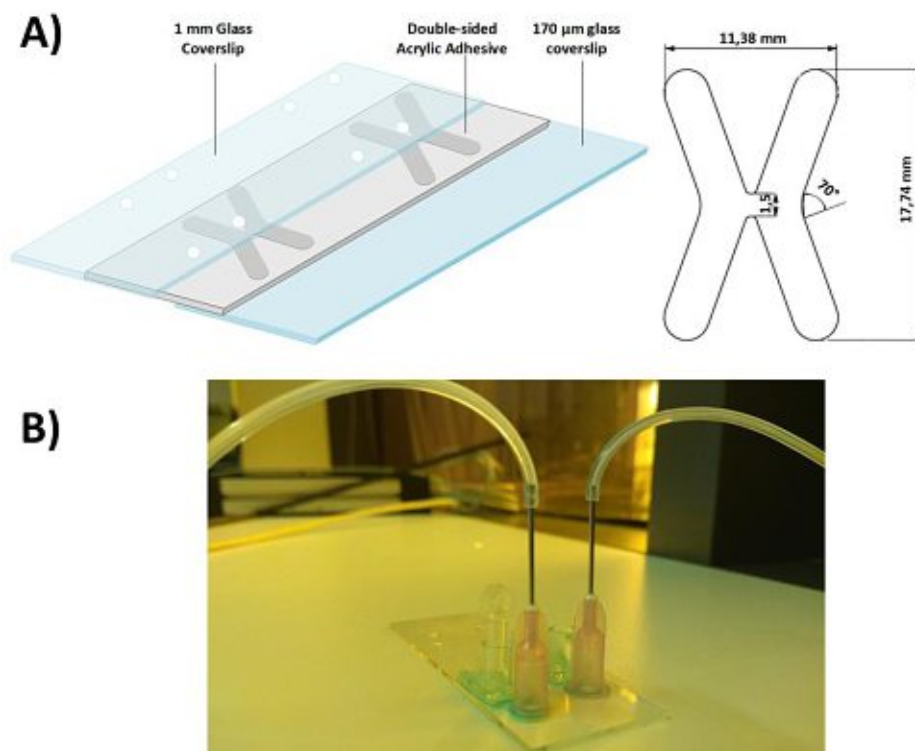


**Figure 35. Microfluidic chamber design. A) Schematic design of the microfluidic chamber with the diameters of the adhesive mold B) the assembled chip with the reservoir and connectors.**

The production of PDMS based BBB usually require a multi-step chip assembly process in which polycarbonate membranes with large pore sizes are implemented. One of the main engineering challenges in such a process is the reproducible and high throughput production of the microfluidic devices, and to ensure that the membrane is tight and not leaking which is especially crucial for creating barrier models. HD bioprinting of membranes directly on the chip could reduce the time and effort needed



to produce these microfluidic devices. Once the mold is assembled the channels can be filled up with the photosensitive monomer solution together with a 2PI and the barrier can be printed according to a CAD. The unpolymerized material can be removed by a simple washing step. This technology also allows the processing of naturally derived hydrogels to avoid the use of plastic membranes in the device. HD bioprinting of hydrogels using gelatin based thiol-ene photo click hydrogel Gel-NB has been demonstrated previously using a diazosulfonate based 2PI.<sup>142</sup> These hydrogels have excellent biocompatibility both as bioink and as scaffold material as demonstrated in chapter 2.3. Furthermore, it is fully biodegradable, and it is possible to achieve different stiffnesses depending on the applied laser power. For the BBB model a C shaped structure was designed. The high-throughput production of the membrane was ensured by a high writing speed of  $1 \text{ m s}^{-1}$  resulting in that a single membrane can be produced under 2 min. The membrane can be fully degraded by external collagenase in 30 min allowing the temporary support of cells while allowing the cells to remodel the barrier (**Figure 36**).

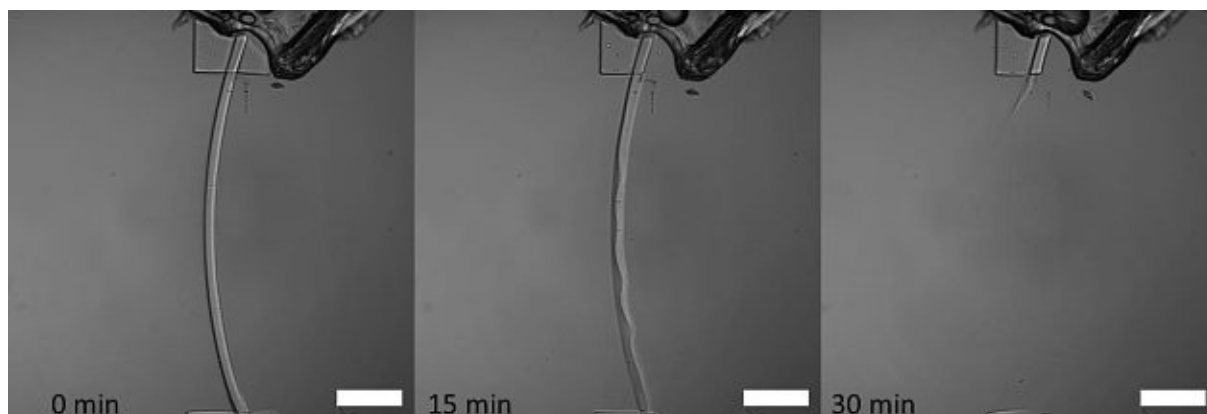


**Figure 36.** Degradation of 3D printed membrane using  $1 \text{ CDU mL}^{-1}$  collagenase. The scale bar represents  $200 \mu\text{m}$ .

Pericytes *in vivo* can be found in vessels embedded in the basement membrane. In order to mimic the *in vivo* conditions, human primary pericytes were directly encapsulated into the bioink during printing for the  $140 \mu\text{m}$  membrane (**Figure 37a**). The effect of the different laser powers on cell viability was established by printing  $300 \times 300 \times 300 \mu\text{m}$  cubes using laser powers ranging from 50 to 100 mW and cells were observed with live-dead staining after 24 h and 5 days post-printing. Cell viability was only impaired at 100 mW, under that there was no significant difference between different laser powers and different time points (**Figure 37b**).



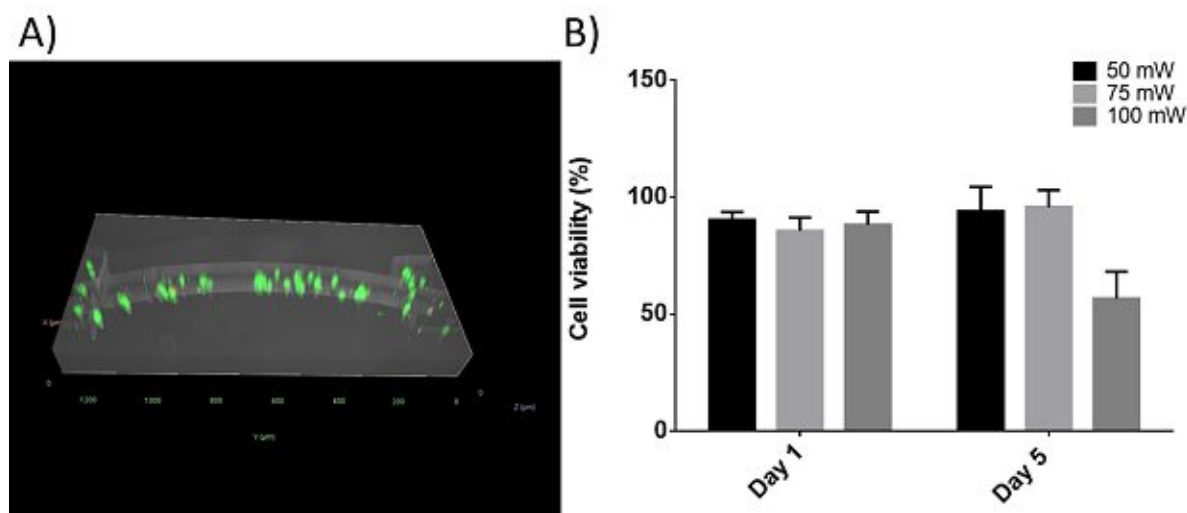


**Figure 37. Viability of human primary pericytes after encapsulation. A) Cells encapsulated in the barrier. B) Viability of cells at different time points when exposed to different laser powers.**

The BBB comprises of two main cell types, vascular endothelial cells on the blood side of the barrier and glial cells in the brain side adjacent to it. For this study, human blood brain barrier endothelial cells (hCMEC/D3) were used on the blood compartment and on the brain compartment astrocytes were added. At different time points (day 2 and day 5) the cells were stained using Calcein-AM and propidium iodide live-dead staining and the cells were imaged with confocal laser scanning microscope. The live cells stain green, while the dead cells can be visualized in red. The results show that after two days the cells were forming a monolayer on both sides of the membrane and they maintained their cell viability. Cells maintained high cell viability and extended morphology after 5 days (**Figure 38**). These results indicate that the bioprinted Gel-NB hydrogel barrier supports cell adhesion and proliferation without the need of any additional coating and can be used directly after fabrication.

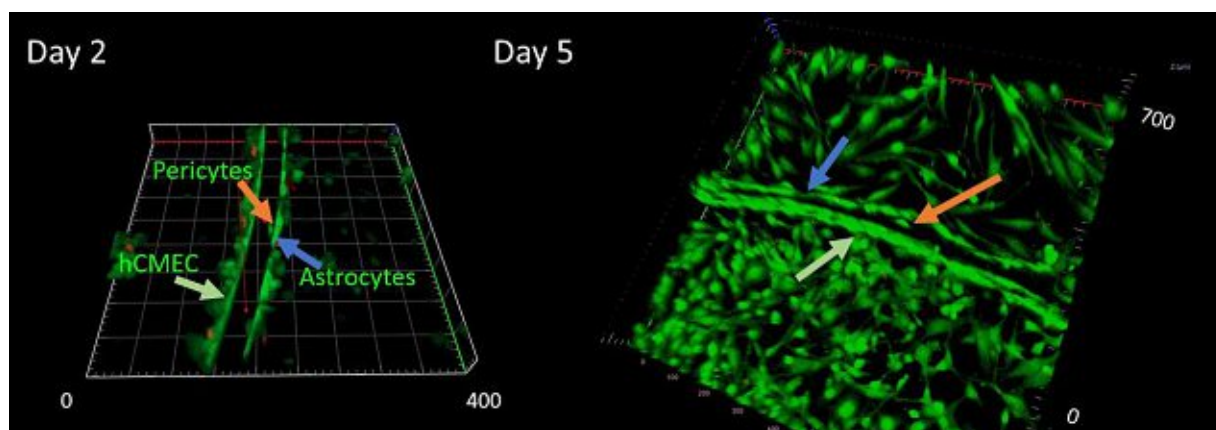


**Figure 38. Seeding of cells on the membrane. The red arrow indicates the embedded pericytes, the green arrows the seeded hCMEC cells and the blue arrow the astrocytes.**

The permeability of the membrane was characterized by tracking the diffusion of different sized molecules across the barrier. For this use, fluorescent substances with molecular weights ranging from 0.38 to 150 kDa were applied and the fluorescence intensity in the two different compartments were imaged every 5 min. For the preliminary tests the 80  $\mu\text{m}$  height chip was used and approximately 500 x 500  $\mu\text{m}$  was the area of interest in both sides of the membrane. Our results showed that approximately 2% of the large molecular weight dextrans (150 kDa and 70 kDa FITC-Dextran) were able to cross the barrier after 1 h. However, almost nearly 8% of the FITC-Albumin was able to penetrate the membrane, although the molecular weight of FITC-Albumin (66 kDa) is comparable to the 70 kDa dextran. This could be explained by the hydrodynamic radius of the substances, which can be measured via several different methods, such as light scattering. Polysaccharides such as dextran have larger hydrodynamic radii than the globular proteins for instance albumin. Previous research showed that the hydrodynamic radius of FITC-albumin is  $5.4 \text{ nm} \pm 0.1$ , while 70 kDa FITC-dextran is around 6 nm, therefore it could pass through the barrier faster.<sup>202,203</sup> The brain to blood ratio of 4 kDa FITC-dextran was nearly 0.4, while the small substances such as fluorescein and riboflavin reached 0.9 and 0.8, respectively (**Figure 39**). The 2000 kDa FITC-dextran with a hydrodynamic radius of  $19.50 \pm 1.29$  nm were unable to enter the hydrogel, suggesting that the pore size of the hydrogel was smaller than 20 nm.<sup>204</sup>

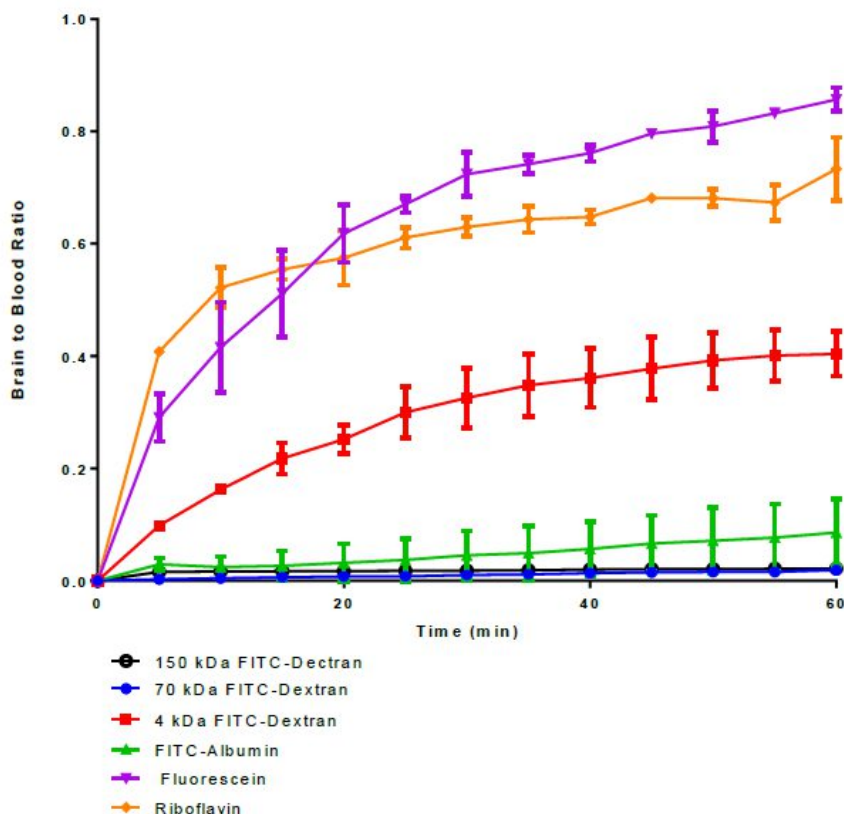


**Figure 39. Permeability of the 80  $\mu$ M membrane to different sized molecules. Small molecules such as riboflavin and fluorescein diffused through the membrane quickly. Larger molecules (4 kDa, FITC-albumin, 70 and 150 kDa FITC-dextran) diffused through the membrane in a reduced rate. All experiments were performed in triplicates.**

The area of interest for the high membrane (140  $\mu$ M) was approximately 2 x 2 mm from the membrane in both compartments. Three different setups were tested, the 3D printed membrane alone, the acellular BBB (containing the 5% UV hydrogel used for the encapsulation of glioblastoma spheroids) and the cellular BBB (hCMEC and astrocytes seeded to their appropriate compartment of the chip additionally to the UV hydrogel).

Our results showed that nearly 4% of the FITC-Albumin were able to penetrate the membrane after 1 h. The brain to blood ratio of 4 kDa FITC-dextran was nearly 0.1, while the smaller substances such as fluorescein and riboflavin reached 0.4 and 0.37, respectively.

The presence of an additional 5% hydrogel decreased the diffusion rate of all tested molecules; however, it was only significant for the smallest tested molecules (riboflavin and fluorescein). The influence of endothelial cells on the diffusion of different sized

molecules were evaluated using the previously mentioned fluorescent substances. hCMECs and astrocytes were seeded onto the membrane and were cultivated for 2 days prior to the experiments. Afterwards, the fluorescent substances were pipetted into the blood compartment of the device and the fluorescent signal was recorded every 5 min at 37 °C for 1 h. The cells decreased the permeability of the membrane to all the tested substances.

A previous *in vivo* study introduced 10 (w/v)% sodium fluorescein to the animal models and was left to circulate for 10 min. Afterwards, the brain tissue was homogenized and the fluorescence levels were normalized against the serum concentration.<sup>205</sup> Their results showed an uptake ratio of fluorescein of approximately 0.05 which is comparable to concentration measured in our system with the cellular BBB (blood to brain ratio of 0.04), while the acellular BBB and the membrane alone both had higher diffusion *in vitro*, 0.06 and 0.12, respectively after 10 min meaning that the presence of the 5% hydrogel decreased the diffusion of fluorescein by half already. However, it is important to note that the fluorescence in the *in vivo* model was analyzed in the brain tissue homogenate, while our system only looks at the accumulation of the fluorescent dye next to the membrane.

In another *in vivo* study, 4 kDa FITC-dextran was injected into the tail vein of mice and was left to circulate for 5 min. Afterwards, the animals were sacrificed and blood was collected as a control. The brain was extracted and the fluorescence of FITC-dextran in the cerebrum was compared to the control. Their results showed a ratio was between 0.001 and 0.0013.<sup>206</sup> Our results with cells present had comparable diffusion with a mean ratio of 0.0011 after 5 min, while the barrier alone had a ratio of 0.02 which is 20 fold higher than the *in vivo* results.

Albumin is a highly water-soluble globular protein which is commonly found in the blood plasma. Previous studies have shown that albumin does not enter the brain parenchyma and stays inside the brain microvessels.<sup>207,208</sup> Our results have shown that although albumin was detected in the brain compartment of the chip, due to the presence of the cells the diffusion of FITC-albumin was 2.5-fold decreased compared to the membrane alone reaching 0.016 brain to blood ratio after 1 h.

Riboflavin is a water-soluble vitamin, also known as B2. The uptake mechanism of riboflavin into the brain has been unclear. A previous study which employed

immortalized rat brain endothelial cells (RBE4) to study the uptake of riboflavin hypothesized that riboflavin uptake is transported via carrier mediated transport system and is dependent on several different factors including sodium levels and temperature.<sup>209</sup> Our results have shown that without cells the diffusion of riboflavin is comparable to fluorescein which has a similar size. However, the diffusion of riboflavin was not decreased significantly in the presence of cells which could be attributed to the possible active transport through the membrane (**Figure 40**).

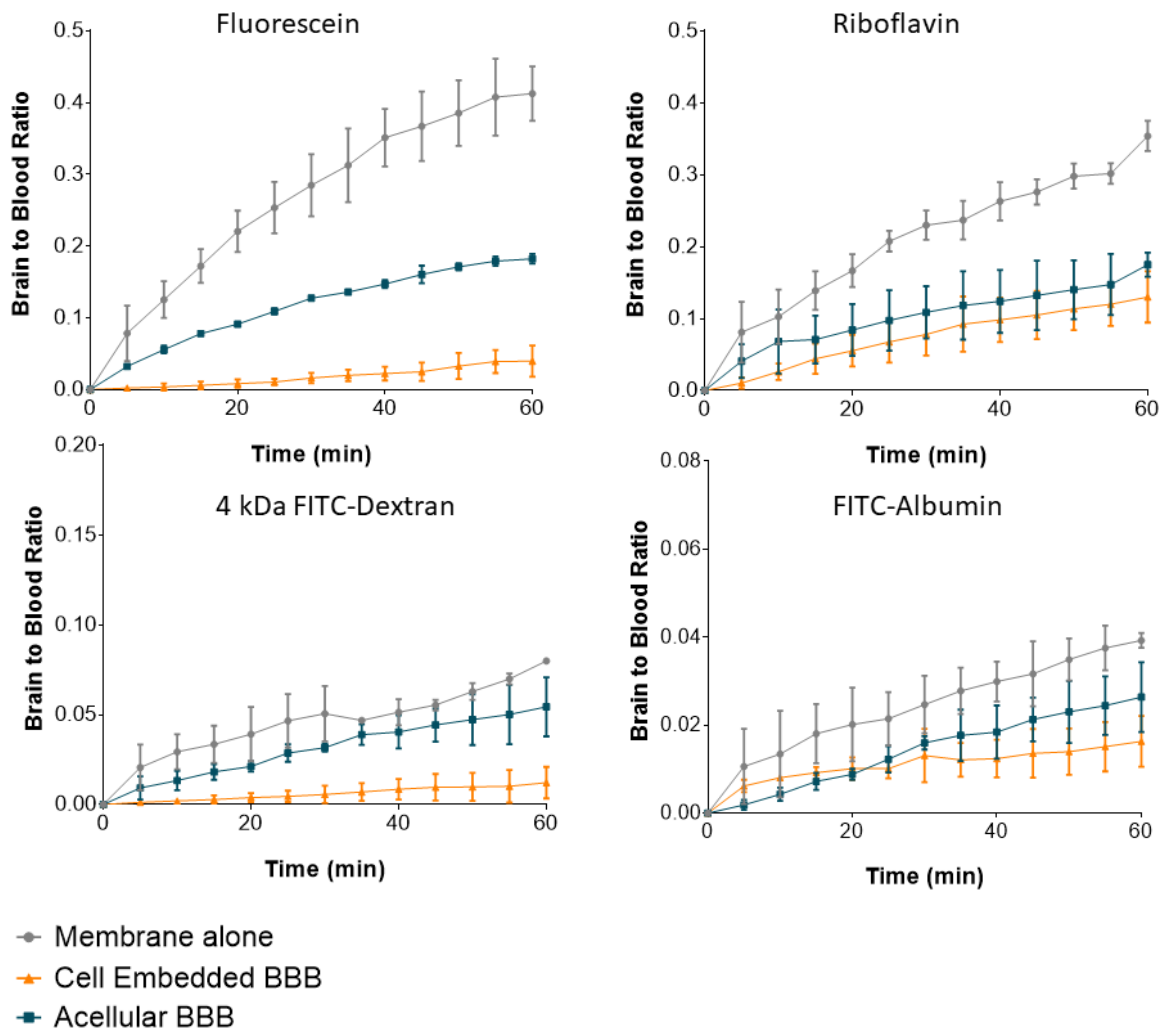


**Figure 40.** Diffusion of different sized molecules through the BBB construct. The membrane alone (grey line) represents the 3D printed hydrogel membrane, the acellular BBB (blue line) is the printed membrane together with the UV hydrogel, while the cellular BBB (orange line) contains the hCMEC and the astrocytes as well additionally to the UV hydrogel. The presence of hydrogel decreased the diffusion of small molecules (riboflavin and fluorescein) by approximately 60 %. The presence of cells further decreased the diffusion of all tested molecules. Albumin diffusion decreased by 50%, 4 kDa dextran by 75%, fluorescein by 90% and riboflavin by 15% in the presence of cells compared to the acellular BBB.

In comparison when HUVECs were used on the membrane instead of the more specific BBB cells, the permeability showed higher values. However, it is important to note, that the area of interest and the chip height of the two constructs differ (80  $\mu\text{M}$  for the HUVECs and 140  $\mu\text{M}$  for the hCMEC cells) and only one cell type was present in this case. Our system with HUVECs showed a blood to brain ratio of 0.15 after 10 min which is approximately 4 times higher than in the previous model. Our results for the 4 kDa FITC-dextran with HUVECs had ten-fold higher diffusion with a mean ratio of 0.013 after 5 min, while the membrane alone had a ratio of 0.1. Earlier studies show that the healthy BBB is largely impermeable to 70 kDa FITC-dextran *in vivo*. Our results after 1 h presented a fluorescence brain to blood ratio of less than 0.006 in the presence of cells, over three-folds less than the membrane alone. Studies using BBB-on-a-chip models exhibited similar finding to our results using a monoculture of endothelial cells and incubating them with 4 kDa and 70 kDa FITC-dextran. However, the increased barrier function was described when co-culture of the cells were used (**Figure 41**).<sup>186</sup>

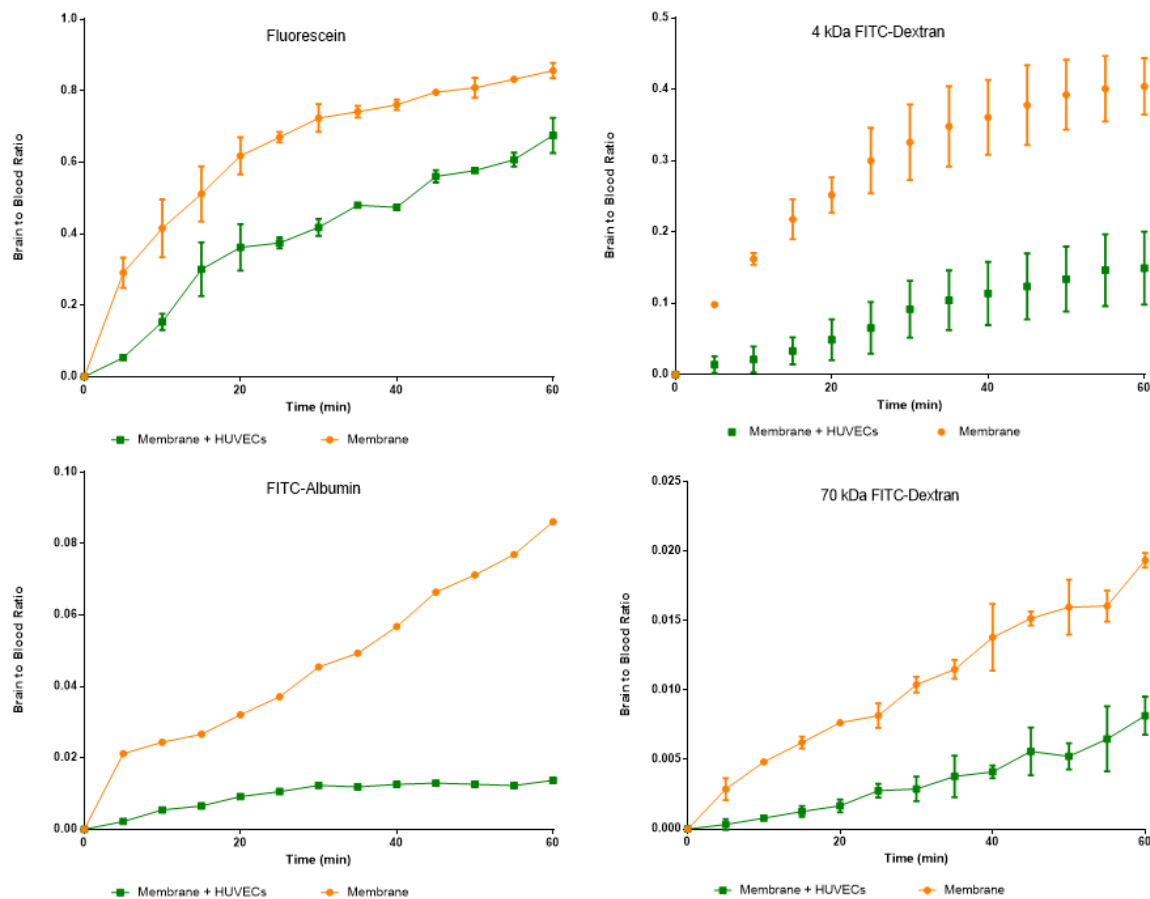


**Figure 41. Diffusion of different sized molecules (70 kDa and 4 kDa FITC-dextran, fluorescein and FITC-albumin) across the membrane in the presence and absence of cells. The presence of cells decreased the permeability of the membrane in every case, by 25 % for 4 kDa, 70 kDa dextran, and fluorescein, and approximately 80 % for FITC-albumin.**

After the contribution of the HUVECs alone was established, 50B11 cells were seeded onto the brain compartment of the chip. The cells were incubated and the diffusion of riboflavin was tested at different time points. Our results have further shown that after one day the diffusion of riboflavin is higher than after 3 days, possibly due to low cell numbers and immature intercellular junction formation. After 5 days the permeability of the system increases again and additionally the standard deviation between samples are increased, possibly due to decreased cell viability under static condition over an extended period of time (**Figure 42**).



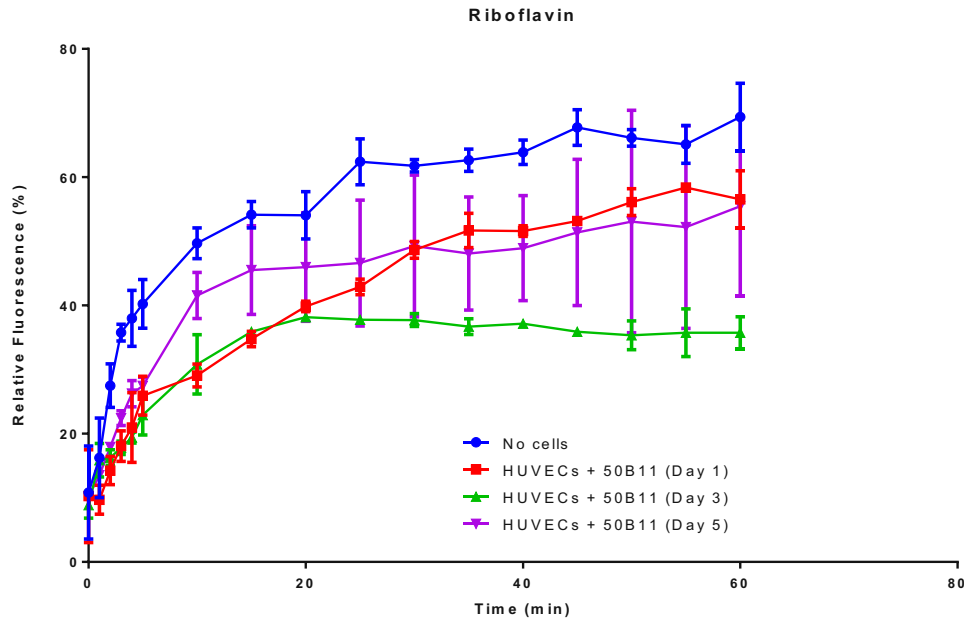


**Figure 42.** The transport of riboflavin across the BBB in presence of HUVECs and 50B11 cells at different time points (n=4)

Endothelial cells within the BBB are characterized by the formation of intercellular junctions which are of crucial importance for the adhesion and signalling between adjacent cells to maintain the function of the vessels. These junctions could be organized into three different groups; gap junctions allow the diffusion of small molecular weight substances, adherens junctions, and tight junctions which are critical in order to establish a barrier function. All of these dynamic junctions are formed by different proteins expressed on the endothelial cells. hCMECs and astrocytes were seeded onto the membrane and were cultured under static conditions for 2 days and 5 days. Afterwards the cells were stained for VE-Cadherin (adherens junction, green) and ZO-1 (tight junction, red). Finally, the samples were stained additionally with 4',6-diamidino-2-phenylindole (DAPI, blue), a stain which binds to the denine–thymine rich regions in DNA, therefore can be used as a nuclear stain. Cells showed expression of ZO-1 and had low expression of VE-Cadherin (**Figure 43**).

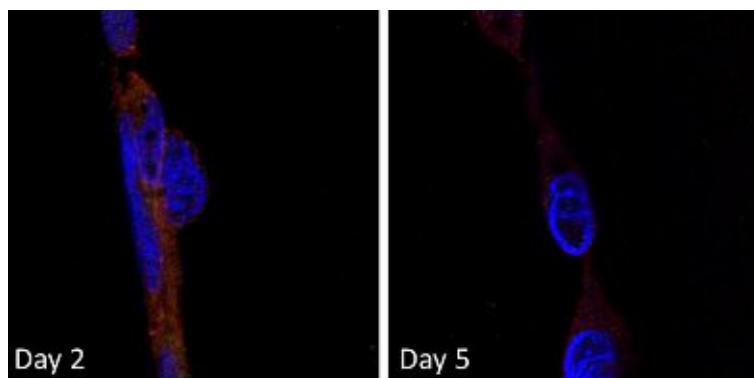


Figure 43. Immunostaining of hCMEC cells after 2 and 5 days.

Finally, the GBM-on-chip was assembled by introducing U-87 spheroids to the brain compartment of the chip. First, the effect of different materials was tested on the viability of the cells. Spheroids of the diameter of approximately 100  $\mu\text{m}$  (100 cells per spheroid) were created by using agarose molds and were encapsulated in 5% Gel-NB (DS53) or 5% GelMOD (DS63) hydrogels via UV irradiation. Although the spheroids were viable in both materials tested, the cells in Gel-NB showed more extended morphology after 5 days, while in GelMOD-63 the spheroids maintained a primarily round shape (Figure 44).

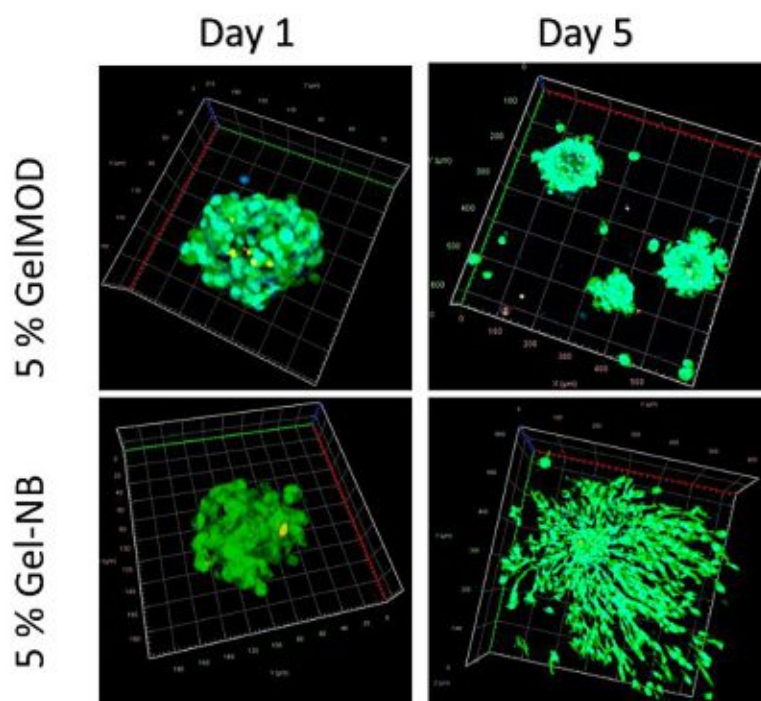
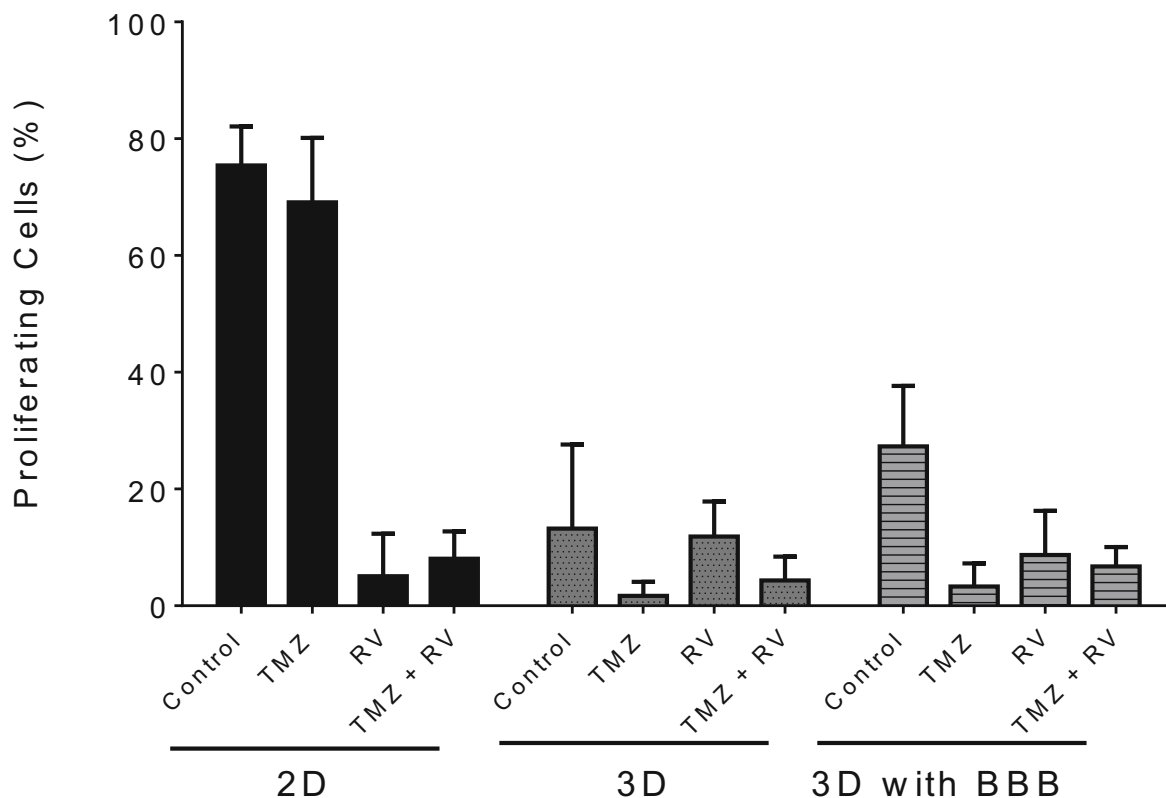


Figure 44. Live-dead staining of UV encapsulated of U-87 spheroids. Two different materials were tested, the 5% GelMOD-63 and 5% Gel-NB (DS53) for 2 and 5 days.

After establishing the optimal conditions of the glioblastoma cells, the spheroids were encapsulated in the brain compartment of the chip using 5% Gel-NB hydrogel according to the schematic depicted in **(Figure 34)**.

After the spheroids were encapsulated, different treatments were tested on the GBM spheroids. As control a 2D monolayer of cells and 3D spheroids encapsulated in 5% Gel-NB hydrogel without the BBB were used. After the encapsulation the cells were treated with 100  $\mu\text{M}$  TMZ or RV or the combination of both for 24 h. To the control cells 1% DMSO were added to the cell culture media to ensure that the effect of the drug is not attributed to the solvent as both TMZ and RV were dissolved in DMSO. After 24 h the cells were washed and were left to recover overnight before Ki-67 and Caspase staining was performed. In 2D, the proliferation of U-87 cells were not significantly affected by 100  $\mu\text{M}$  TMZ resulting in a mean proliferation of 69% of the cells compared to the control (75%). On the other hand, RV had a significant effect both alone (5% of proliferating cells) and in combination with TMZ (8% proliferating cells) on cell viability, however it was not statistically significant compared to RV alone. Under 3D culturing conditions, the control spheroids without BBB had approximately 13% and the 3D model with BBB approximately 27% of proliferating cells which could be due to the proximity of the co-culture BBB and the smaller volume of hydrogel compared to the 3D encapsulated spheroids. The TMZ treatment showed significant decrease in the proliferation rate compared to the 2D culture, however in the case of BBB samples the cells showed approximately 10 times the amount of proliferation (3%) compared to the 3D culture without BBB (0.3%) We hypothesize that this could be due to the BBB as the membrane with cells limits the diffusion of the TMZ into the brain compartment. Furthermore, the presence of the BBB reduced the effect of the combination treatment as well **(Figure 45)**.



**Figure 45. Proliferation of U-87 cells treated with TMZ, RV and the combination of both in 2D, 3D and GBM-on-chip calculated by the Ki-67 positive cells.**

Additionally, to the proliferation of the cells, the apoptotic cells were also stained using Image-IT live caspase stain. The 2D samples the cells treated with RV or the combination of RV and TMZ showed the highest number of apoptotic cells (red) and least amount of proliferation (green). The same tendency was visible for the 3D control and the 3D BBB model as well (**Figure 46**).

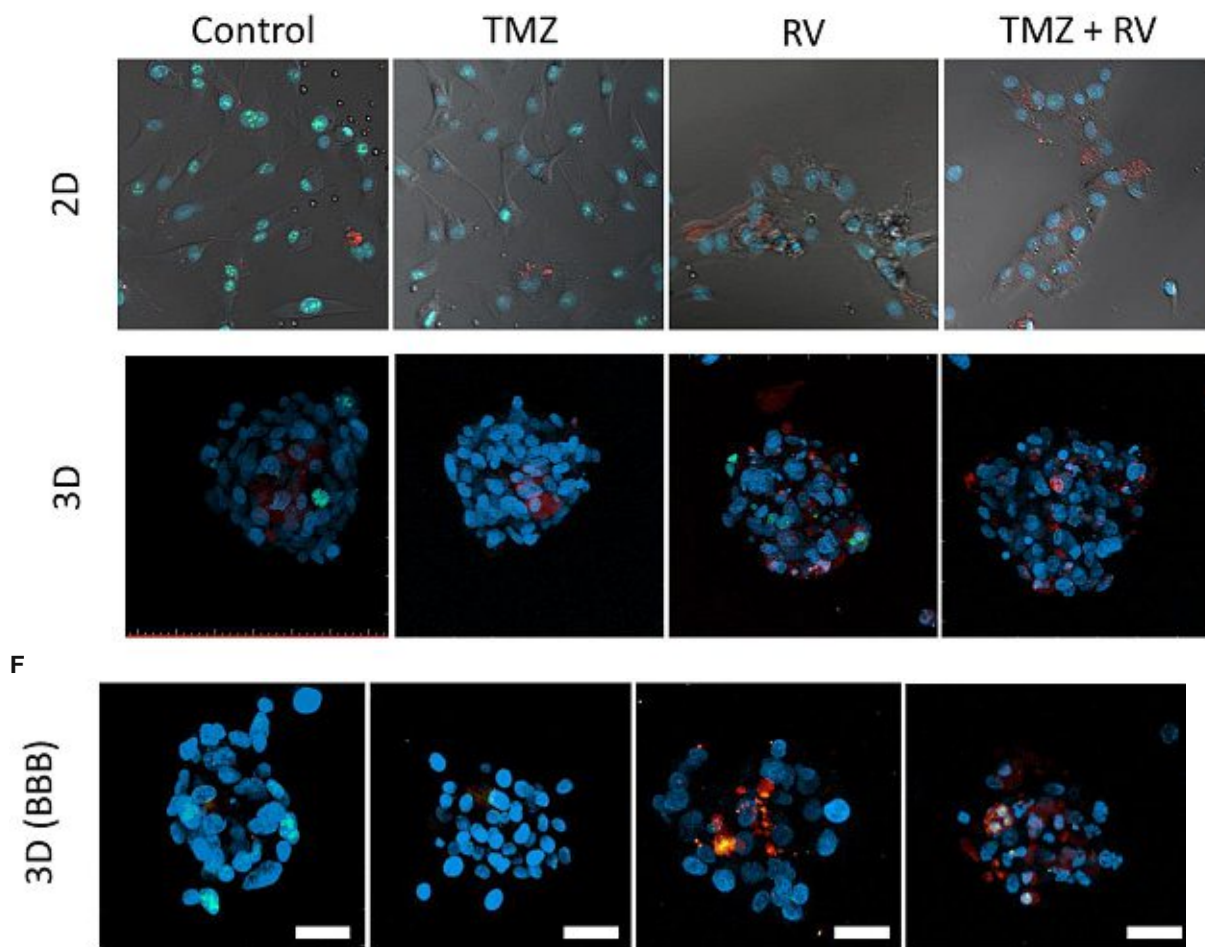


Figure 46. Caspase and Ki-67 staining of the treated U.87 spheroids using three different setups, 2D monolayer culture, 3D culture embedded in 5 % Gel-NB hydrogel and spheroids on the chip. The green signal is the Ki-67 positive cells, the red is the apoptotic cells and blue is the DAPI representing the cell nucleus. The scale bar represents 20  $\mu\text{m}$ .

### 3.2.5 Conclusion

In this project we have demonstrated the fabrication of a novel a GBM model on a chip. A medical grade biocompatible pressure sensitive double-sided tape was used instead of PDMS to produce the mold which can be mounted on high precision glass slide to enable the direct HD bioprinting of the membrane and the optical imaging of the channels. The fast and high-throughput production of hydrogel barriers while maintaining the high resolution of the structures were achieved via 2PP. The BBB was printed directly on the chip without the need of additional assembly step and the residual material could be removed via a single washing step. The membranes can be seeded with different cells without the need of additional coating steps. Both the endothelial cells and astrocytes cells showed good viability and monolayer formation

after 2 day of seeding, and the embedded pericytes maintained their cell viability after embedding in the bioink. The membrane was characterized by the diffusion of different sized molecules across the membrane and it showed a size dependent perfusion rate of the different fluorescent substances. When the membrane was seeded with cells the diffusion rates decreased in all cases. Immunostaining of the cells suggested the formation of tight junctions even after 48 h of cells seeding. We hypothesize that our model can be further enhanced by the introduction of shear stress as literature suggest that endothelial cell survival and the intercellular junction formation is enhanced upon perfusion.<sup>187</sup> Additionally, perfusion could provide a continuous removal of metabolites thus increase the life time of the constructs. This GBM construct could enable the screening of possible drugs and therapeutics and their transport through the BBB in order to improve the currently available treatment option and delivery strategies and gain more understanding in the disease progression.

### 3.3 Screening of Two-Photon Activated Photodynamic Therapy Sensitizers Using a 3D Osteosarcoma Model

This chapter is published and contains text from publication

Dobos A, Steiger W, Theiner D, Gruber P, Lunzer M, Van Hoorick J, Van Vlierberghe S and Ovsianikov A **2019** Screening of two-photon activated photodynamic therapy sensitizers using a 3D osteosarcoma model *Analyst* with permission from Royal Society of Chemistry

**doi:10.1039/C9AN00068B**

The z-scan measurements were performed by W. Steiger (TU Wien) and D. Theiner (TU Wien).



### 3.3.1 Introduction

Photodynamic therapy (PDT) typically comprises three individually harmless components: a photosensitizing agent (PS), light, and oxygen to induce cell damage. PDT has been extensively researched for multiple clinical applications such as the treatment of cancer and several other diseases, including a therapy for posterior capsule opacification and age-related macular degeneration.<sup>210,211</sup> PDT could also provide possible alternatives to eliminate pathogenic microorganisms, such as viruses, fungi, yeast and antibiotic resistant bacteria.<sup>212</sup>

In PDT, energy is transferred from light to oxygen by the PS to generate ROS.<sup>99</sup> The PS absorbs photons of a certain wavelength and is thereby transferred into an excited state, which can dissipate its excitation energy by emission of heat or light, or by intersystem crossing to a triplet-state. There are two types of reactions that can take place once the PS is excited which can also occur simultaneously. The Type I pathway involves a hydrogen atom (electron) transfer from the excited PS to a substrate such as a molecule or the cell membrane to form radicals, which in turn react with molecular oxygen species to produce ROS such as superoxide or hydroxyl radicals. In the Type II pathway, singlet oxygen is produced directly after the PS transfers energy to molecular oxygen.<sup>213</sup> There are several different processes that could be initiated by PDT and are involved in tumour destruction. First, ROS can cause apoptosis or necrosis of tumour cells. In another mechanism singlet oxygen can damage the vasculature of tumours.<sup>213</sup> Finally, PDT can activate the immune response by membrane dysregulation of surface integrin-associated protein CD47 and damage-associated molecular patterns.<sup>214</sup>

There are several factors that have an effect on PDT efficacy such as PS localization, the administration interval, the local oxygen concentration and light exposure time.<sup>213</sup> Localization of the PS is crucial due to the short half-life (< 50 ns) and radius of action (< 40 nm) of singlet oxygen.<sup>215,216</sup> As a consequence, sensitizers which are not internalized by cells usually show poor performance in PDT even if they produce large amounts of radicals.<sup>213</sup> The wavelength and type of light delivery also have a large effect on the efficacy of PDT.<sup>217</sup> The applied wavelength influences not only the PS

absorption efficiency but also affects the penetration depth. Due to the wavelength-dependent scattering and absorption of skin, red light penetrates the skin and human tissues deeper than blue light, about 5 mm vs. 1 mm, respectively.<sup>218</sup>

In this respect, two-photon excited photodynamic therapy (TPE-PDT) offers several benefits when compared to traditional one-photon excited PDT, such as deeper penetration of tissue. Due to the non-linear absorption the PDT damage can be confined to a small excitation volume reducing collateral damage to the surrounding healthy tissue. In TPE-PDT, the PS is promoted to its excited state by absorbing two photons of a longer wavelength simultaneously during irradiation. Relaxation occurs via Type I or Type II reaction with molecular oxygen as described previously.<sup>219</sup> Due to the nonlinear behaviour of the absorption process high peak power lasers such as mode-locked Ti:Sapphire lasers with femtosecond pulse durations are required to achieve two-photon absorption.<sup>220</sup> Different photosensitizers have been developed for TPE-PDT applications, including porphyrin derivatives, ruthenium complexes, conjugated polymers, and nanoparticles.<sup>219,221,230,231,222–229</sup> The main considerations when choosing the optimal two-photon excitation photosensitizer (TPE-PS) are low dark toxicity, high two-photon absorption cross-section at a certain wavelength and a substantial triplet state quantum yield.<sup>232</sup>

Pre-clinical testing of TPE-PS presents some challenges. TPE-PDT has been tested *in vivo* using animal models to induce cancer regression in mice.<sup>233</sup> The *in vitro* evaluation of treatment efficacy usually relies on 2D monolayer cell systems. However, there is increasing evidence that this setting does not provide sufficient comparison to *in vivo* conditions as the cellular microenvironment has a pronounced effect on the response to treatment.<sup>234,235</sup> Microfluidic 3D cell cultures have been proposed previously to study classical one-photon PDT efficacy but most of these systems rely on qualitative assessment of cell viability using live-dead staining.<sup>236,237</sup> However, an *in vitro* platform for quantifying TPE-PDT efficiency using a hydrogel-based multicellular 3D cell culture has not been reported to date.

The aim of this study is to introduce a pre-screening platform of TPE-PS using a 3D osteosarcoma model together with adipose tissue-derived stem cells (ASC/TERT). Three different TPE-PS were used for testing the system, a two-photon photoinitiator P2CK, a fluorescent dye Eosin Y, and a porphyrin (TPP) (**Figure 47**). The most

extensively studied photosensitizers are in fact porphyrins, which contain four pyrrole rings with side chains with an absorption maximum usually centred around 400 nm.<sup>238</sup> Eosin Y absorbs in the visible light region (490–650 nm) and has been proposed as a photosensitizer to inactivate bacteria biofilms using PDT.<sup>239</sup> It has also been employed as a sensitizer for two-photon polymerization processes together with a co-initiator and an acrylate-based resin and for localized two-photon induced thiol-ene click reactions.<sup>240,241</sup> P2CK, a water soluble benzylidene cycloketone-based two-photon photoinitiator, has been used for two-photon polymerization of hydrogels. However its use together with cells leads to poor cell survival and considerable phototoxicity in the concentration range ( $> 1$  mM) required for the formation of stable hydrogel structures.<sup>53,72</sup> On the other hand, when used as two-photon sensitizer for cleavage of photolabile hydrogels a much lower concentration is necessary ( $< 0.5$  mM) that does not significantly harm cells outside of the focal volume.<sup>242</sup> In order to optimize a working window for the proposed TPE-PS, the irradiation wavelengths should match the two-photon absorption maximum of the used PS. The z-scan technique, introduced in 1990, has become a standard method to characterize higher order nonlinearities such as two-photon absorption (2PA) cross sections.<sup>243</sup> Using a motorized stage, a thin sample (sample length smaller than the Rayleigh length of the focused laser beam) is moved in and out of the focal plane of a laser beam along the z-axis.<sup>243,244</sup> First, the 2PA cross-sections of the compounds in a 720-1000 nm spectral range were established using an in-house developed automated z-scan setup. Afterwards, the cellular uptake of the TPE-PS were visualized using laser scanning confocal microscopy (LSM). The efficacy of the PS excited at their optimal wavelength was quantified via Presto Blue metabolic activity assay using a 3D model of osteosarcoma cells encapsulated in a gelatine-based hydrogel. Finally, to show the precision of the irradiation, ASC/TERT cells, co-cultured together with osteosarcoma (MG63) spheroids, were visualized after selective two-photon irradiation of spheroids only in the presence of the PS using LSM.

### 3.3.2 Aim

The aim of this study is to introduce a pre-screening platform of TPE-PS using a 3D osteosarcoma model together with adipose tissue-derived stem cells. Three different

TPE-PS were used for testing the system, a two-photon photoinitiator P2CK, a fluorescent dye Eosin Y, and a porphyrin (TPP) (**Figure 47**). The most extensively studied photosensitizers are in fact porphyrins, which contain four pyrrole rings with side chains with an absorption maximum usually centred around 400 nm.<sup>238</sup> Eosin Y absorbs in the visible light region (490–650 nm) and has been proposed as a photosensitizer to inactivate bacteria biofilms using PDT.<sup>239</sup> It has also been employed as a sensitizer for two-photon polymerization processes together with a co-initiator and an acrylate-based resin and for localized two-photon induced thiol-ene click reactions.<sup>240</sup> P2CK, a water soluble benzylidene cycloketone-based two-photon photoinitiator, has been used for two-photon polymerization of hydrogels. However its use together with cells leads to poor cell survival and considerable phototoxicity in the concentration range ( $> 1$  mM) required for the formation of stable hydrogel structures.<sup>53,72</sup> On the other hand, when used as two-photon sensitizer for cleavage of photolabile hydrogels a much lower concentration is necessary ( $< 0.5$  mM) that does not significantly harm cells outside of the focal volume.<sup>242</sup> In order to optimize a working window for the proposed TPE-PS, the irradiation wavelengths should match the two-photon absorption maximum of the used PS. The z-scan technique, introduced in 1990, has become a standard method to characterize higher order nonlinearities such as two-photon absorption (2PA) cross sections.<sup>243</sup> Using a motorized stage, a thin sample (sample length smaller than the Rayleigh length of the focused laser beam) is moved in and out of the focal plane of a laser beam along the z-axis.<sup>244</sup> First, the 2PA cross-sections of the compounds in a 720-1000 nm spectral range were established using an in-house developed automated z-scan setup. Afterwards, the cellular uptake of the TPE-PS was visualized using laser scanning confocal microscopy (LSM). The efficacy of the PS excited at their optimal wavelength was quantified via Presto Blue metabolic activity assay using a 3D model of osteosarcoma cells encapsulated in a gelatine-based hydrogel. Finally, to show the precision of the irradiation, ASC/TERT cells, co-cultured together with osteosarcoma (MG63) spheroids, were visualized after selective two-photon irradiation of spheroids only in the presence of the PS using LSM.

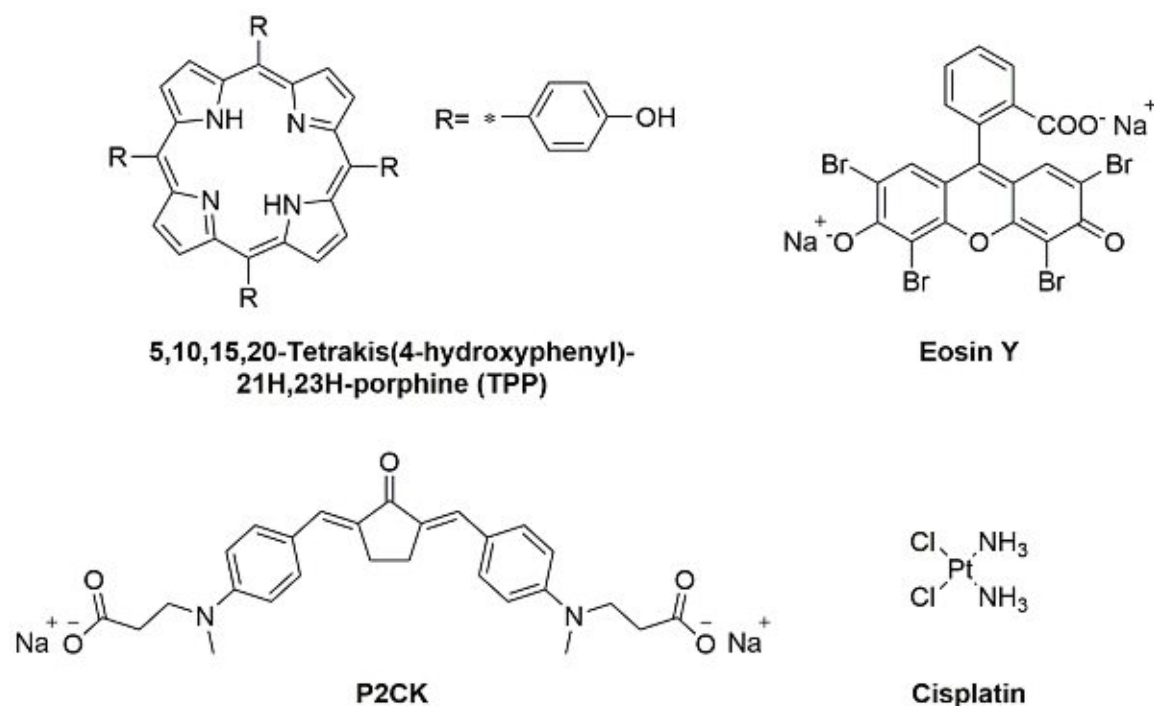


**Figure 47.** Molecular structures of the investigated two-photon photosensitizers (TPE-PS) and reference compound cisplatin.

### 3.3.3 Experimental

All chemicals and cells were purchased from Sigma-Aldrich (Saint Louis, USA) unless stated otherwise. GraphPad Prism 6 was used for graphs.

#### 3.3.3.1 Spectral scanning of photosensitizers

UV-VIS spectra were determined using a Perkin Elmer Lambda 750 spectrometer. Z-scan measurements were performed on a home-built setup powered by a high power femtosecond laser oscillator (MaiTai DeepSee, Spectra Physics, Santa Clara, USA) with a tuning range of 690-1040 nm, a repetition rate of 80 MHz and a pulse duration of 70 fs.<sup>117</sup> Using a motorized stage the transmitted signal at 25 positions along the focused beam is recorded. A beam chopper with 90 Hz rotation frequency and an on-time of 78  $\mu$ s reduces the exposure time of the sample to prevent thermo-optical effects caused by the high repetition rate of the laser.<sup>245</sup> Each z-scan setting was measured in triplicate. Stock solutions of P2CK (10 mM), Eosin Y (3 mM), and cisplatin (1 mM) were prepared by dissolving the respective PS in PBS, while 5,10,15,20-Tetrakis(4-hydroxyphenyl)-21H,23H-porphine (TPP) was dissolved in DMSO at a concentration of 10 mM. For each material four different laser powers were used to verify that heat

accumulation caused by the high repetition rate of the laser did not affect the measured 2PA behaviour.

### 3.3.3.2 Two-photon irradiation setup

The above mentioned setup was used throughout the TPE-PDT experiments with two different objectives (C-Achroplan 10x/0.3NA, and 2.5x/0.085NA, ZEISS).<sup>53</sup>

The peak intensity ( $I_{\text{peak}}$ ) of the laser for a  $\text{sech}^2$  shaped pulse is calculated by **Equation 4**.

Full width half maximum (FWHM) of the volumetric pixel (voxel) for the different objectives and wavelengths were calculated by the following equations (5) and (6) and the results can be found in (Table 3);<sup>166</sup>

**Table 3. Full width half maximum (FWHM) and the resulting volume of the voxel for the different objectives used in this study.**

<i>Objective</i>	<i>Wavelength</i> [nm]	<i>FWHM<sub>x,y</sub></i> [μm]	<i>FWHM<sub>z</sub></i> [μm]	<i>Volume</i> [μm <sup>3</sup> ]
<i>10x, 0.3 NA</i> <i>Precision</i>	720	0.9	13.2	18.9
	850	1	15.5	31.1
	960	1.2	17.5	44.8
<i>2.5x, 0.085 NA</i> <i>High-Throughput</i>	720	3.2	165.9	2672.6
	850	3.8	195.8	4397.4
	960	4.3	221.2	6335.2

### 3.3.3.3 Cell culture

mCherry-labelled MG63 osteosarcoma cells, and GFP-labelled adipose-derived stem cells (ASC/TERT1) (Evercyte, Vienna, Austria) were maintained at 37 °C and 5% CO<sub>2</sub> in an incubator. The transfection of the cells is described elsewhere.<sup>118</sup> The osteosarcoma cells were cultivated in DMEM high glucose media supplemented with 10% FCS, and 1% penicillin-streptomycin and the adipose tissue-derived stem cells



were cultured in EGM-2 (Lonza, Walkerville, MD, USA) supplemented with 10% FCS. The cells were detached using 0.5% trypsin-EDTA solution and centrifuged at 170 relative centrifugal force (RCF) for 5 min. Afterwards, cells were re-suspended in the corresponding media and reseeded in T75 cell culture flasks (VWR, Radnor, PA, USA).

#### 3.3.3.4 *Gelatin-norbornene synthesis*

Gelatin-norbornene with a degree of substitution (DS) of 90% was synthesized according to a previously reported protocol.<sup>246</sup>

#### 3.3.3.5 *Cell viability assay*

10 wt% gelatine-norbornene (GelNB, DS = 90%) stock solution was prepared in PBS. MG63 cells were trypsinized and resuspended in cell culture media (3 million cells mL<sup>-1</sup>) to achieve a final concentration of 5 wt% GelNB. Next, dithiothreitol in a 1:1 thiol-ene ratio (10 mM) and 0.15 mM Li-TPO-L was added.<sup>[40]</sup> The optimal cell number for encapsulation was chosen to be 3 million per mL based on a preliminary experiment (**Figure 48**). 15  $\mu$ L of the hydrogel-cell suspension was added to each well of a glass bottom 384-well plate (Greiner Bio-One, Kremsmünster, Germany). Encapsulation was performed by 1 Joule UV-irradiation (368 nm) (Boekel UV Crosslinker, Boekel Industries, Feasterville, USA).<sup>113</sup> In order to establish a working concentration for the PS, different concentrations of PS were added and were incubated for 4 h. TPP was dissolved in DMSO at a concentration of 1 mg mL<sup>-1</sup> and diluted to the required concentration using cell culture media. The DMSO concentration never exceeded 0.1% of the media. Afterwards, the samples were washed and incubated for 2 days to remove any residual PS. Presto Blue metabolic assay was used according to the protocol provided by the manufacturer (Invitrogen, Carlsbad, USA). The emission at 590 nm was recorded at an excitation wavelength of 560 nm using a plate reader (BioTek Synergy H1, Winooski, USA). Afterwards, the efficacy of the light treatment was established. The highest non-toxic concentration of the PS was established to be 0.6  $\mu$ M for TPP, 0.5 mM for P2CK and 0.25 mM for Eosin Y. MG63 cells were encapsulated in the previously described manner and incubated with the PS for 4 h before they were two-photon irradiated at the respective optimal wavelength, 720 nm



for TPP, 850 nm to P2CK using a 2.5x objective, with applied peak intensity of 550 GW cm<sup>-2</sup> and a laser writing speed of 4 m s<sup>-1</sup>. Afterwards, the wells were washed and the Presto Blue assay was performed. Due to the low two-photon absorption of Eosin Y and the hence insufficient output of the laser system used at 960 nm, Eosin Y was only used for cancer spheroid experiments.

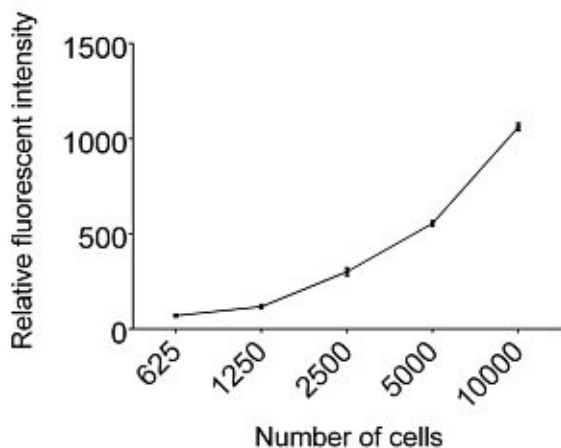


**Figure 48.** Calibration of cell numbers for the Presto Blue assay using the 384-well glass bottom plate.

### 3.3.3.6 Cellular uptake of photosensitizers

MG63 cells were seeded in a 96-well plate (5000 cells per well) and incubated overnight. The next day, solutions of the photosensitizers were added at concentrations of 0.5 mM P2CK, 0.25 mM Eosin Y, and 0.6  $\mu$ M TPP. The cells were incubated for 4 h before laser scanning microscopy (LSM, LSM 700, Carl-Zeiss, Oberkochen, Germany) images were taken using a 32x water-immersion objective (32x, 0.85 NA, ZEISS, using an excitation wavelength of 555 nm for P2CK and 488 nm for TPP and Eosin Y.

### 3.3.3.7 Cell spheroid imaging

In order to visualize that TPE-PDT can be restricted to the two-photon irradiated volume, MG63 spheroids co-cultured together with adipose-derived stem cells were used. Spheroids were produced using microtissue-molds according to a protocol described elsewhere.<sup>43</sup> 24 h after spheroids had formed, they were encapsulated

together with  $1 \text{ million mL}^{-1}$  concentration of ASC/TERT-GFP cells in 5 wt% GelNB prepared following the above-mentioned protocol. The cell containing hydrogels were incubated overnight and then imaged using LSM. Afterwards, different concentrations of PS were added for 4 h and then spheroids were irradiated through a 10x objective using a peak intensity of  $700 \text{ GW cm}^{-2}$ . After PDT treatment, the hydrogel constructs were washed and then incubated for 2 days before LSM images were taken. As a positive control,  $30 \text{ }\mu\text{M}$  cisplatin was incubated with cells for 48 h before cells were imaged using LSM.

### 3.3.4 Results and Discussion

In order to establish an optimal wavelength for TPE-PDT, the absorption spectrum for the different PS has to be determined. To this end, the two-photon absorption spectra were generated by z-scan measurements. Since the linear UV/VIS absorption maximum of Eosin Y was at 506 nm, the 2PA absorption region was estimated to be around 1000 nm (**Figure 49a**). Although, the z-scan assay did yield a change in signal at the focus at 1000 nm, this change was within the noise range of the set up and therefore did not allow reliable extraction of a two-photon absorption cross section ( $\sigma_{2PA}$ ). To overcome this limitation, the Eosin Y concentration was increased to 3 mM for further measurements. These measurements indicated an optimal two-photon absorption window for Eosin Y at around 960-1000 nm. For cisplatin, a concentration of 1 mM in PBS was sufficient to measure the nonlinear absorption. While both compounds exhibited nonlinear absorption behaviour, their 2PA were relatively low i.e. below 100 Göppert-Mayer (GM,  $1 \text{ GM} = 10^{-50} \text{ cm}^4 \text{ s photon}^{-1} \text{ molecule}^{-1}$ ).<sup>247,248</sup> The z-scan analysis of a 10 mM P2CK solution in PBS revealed an increase in  $\sigma_{2PA}$  towards 700 nm, as well as a local absorption maximum at 850 nm (405 GM). Z-scan measurements of TPP were performed using a 10 mM solution in DMSO. The results for TPP showed a 2PA cross section of 112 GM at 860 nm which decreased to 34 GM at 980 nm. At 1000 nm the signal drop was below the detection limit. The 2PA cross section increased drastically towards 700 nm where the extracted 2PA cross section was in the range of a several thousand GM (**Figure 49b**). Due to this high  $\sigma_{2PA}$  a concentration study was carried out (**Figure 50**). This was performed to test, if a variation in concentration affects the 2PA behaviour. Therefore, three additional concentrations of TPP in DMSO (0.5, 1 and 2 mM) were selected. Even at 0.5 mM the

signal drop at 700 nm was still 17%, exhibiting significantly higher 2PA activity than the other screened substances, which is due to the larger conjugated  $\pi$ -system of TPP.

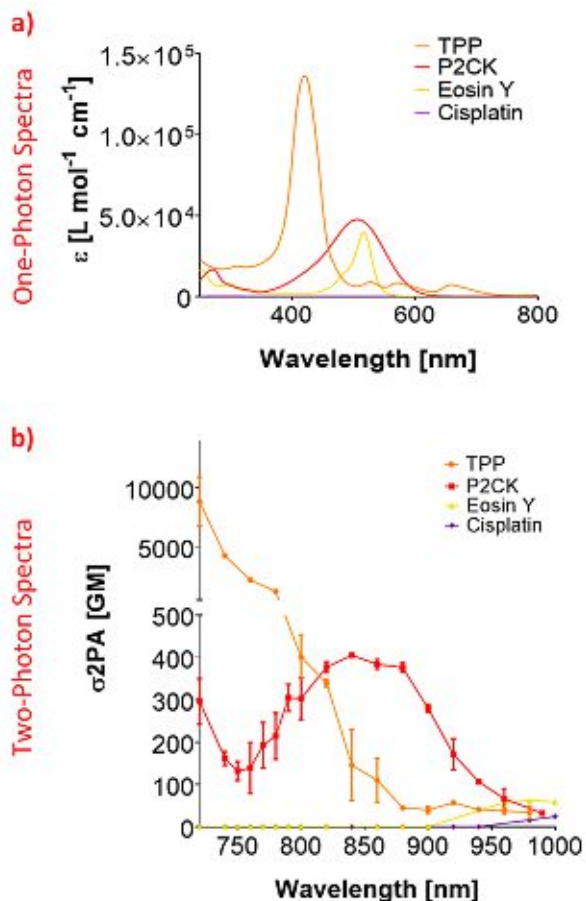


**Figure 49.** One-photon and two-photon absorption spectra of the investigated compounds. (a) UV/VIS absorption spectra. The molar absorptivity coefficient ( $\epsilon$ ) was calculated for the different substances. TPP showed the highest absorptivity with an absorption maximum at the around 420 nm ( $\lambda_{\max} = 421$  nm,  $\epsilon_{\lambda_{\max}} = 1.4 \times 10^5$  nml<sup>-1</sup>cm<sup>-1</sup>). P2CK and Eosin Y had their  $\lambda_{\max} = 506$  nm,  $\epsilon_{\lambda_{\max}} = 4.8 \times 10^4$  nml<sup>-1</sup>cm<sup>-1</sup>, and  $\lambda_{\max} = 517$  nm,  $\epsilon_{\lambda_{\max}} = 3.9 \times 10^4$  nml<sup>-1</sup>cm<sup>-1</sup>, respectively. Cisplatin had the lowest absorption. ( $\lambda_{\max} = 300$  nm,  $\epsilon_{\lambda_{\max}} = 120$  nml<sup>-1</sup>cm<sup>-1</sup>) (b) 2PA spectra of the photosensitizers. The two-photon absorption maximum of TPP can be found at 720 nm ( $\sigma_{2PA} = 8865$  GM), that of P2CK at 850 nm ( $\sigma_{2PA} = 405$  GM), Eosin Y has its maximum at 980 nm ( $\sigma_{2PA} = 62$  GM) and cisplatin has its highest  $\sigma_{2PA}$  at 1000 nm ( $\sigma_{2PA} = 25$  GM).

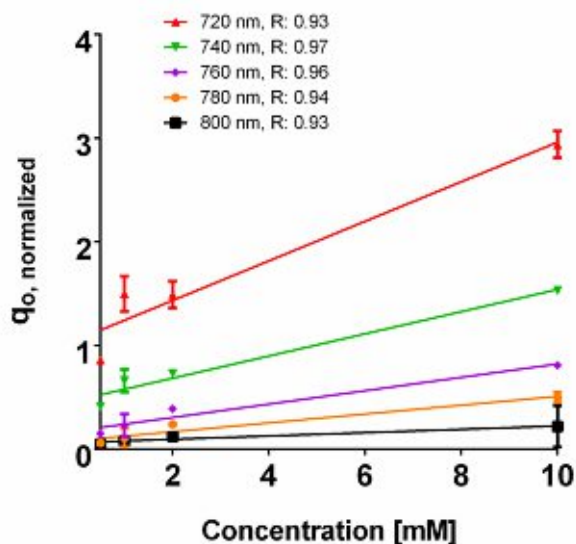
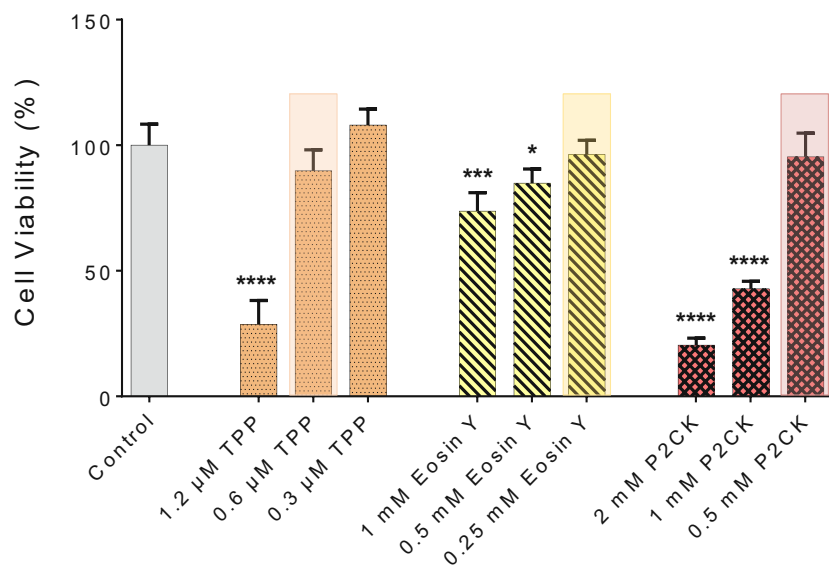


Figure 50. Concentration dependence of  $q_0$  value to the concentration of TPP.

For the *in vitro* 3D TPE-PDT experiments, MG63 osteosarcoma cells were encapsulated in 5 wt% gelatine-norbornene (Gel-NB) hydrogel supplemented with a dithiothreitol (DTT) crosslinker in an equimolar thiol-ene ratio and UV-photoinitiator Li-TPO-L (0.15 mM) in a glass bottom 384-well plate using UV-induced photopolymerization. To establish the biocompatible concentration for each PS, Eosin Y and P2CK were dissolved in cell culture media. TPP was dissolved in DMSO at a concentration of  $1 \text{ mg mL}^{-1}$  and was further diluted in cell culture media, not to exceed 0.1 % DMSO of the total volume. Different concentrations of the PS were added to the wells and incubated for 4 h. The dark cytotoxicity of PS was established by Presto Blue metabolic assay, which is based on a resazurin-based solution that is cell permeable and can be reduced inside the mitochondria of living cells. The fluorescent reaction product can be detected and quantified by a spectrometer/plate reader. The highest possible biocompatible concentration was used for the later experiments, highlighted in (Figure 51). P2CK was tolerated by the cells up to 0.5 mM, which was the highest among the substances, followed by Eosin Y with 0.25 mM whereas TPP was non-toxic in dark conditions up to 0.6  $\mu\text{M}$ .



**Figure 51. Dark toxicity of investigated PS.** Encapsulated MG63 osteosarcoma cells were incubated with solutions of the PS in media for 4 h in the dark. Afterwards, the samples were washed and incubated for 2 days. Presto Blue metabolic assay was performed to quantify the viability of the cells. The highest acceptable concentration of PS was then used for the PDT experiments, 0.3 μM TPP, 0.25 mM Eosin Y and 0.5 mM P2CK, respectively. The statistical significance was addressed by one-way ANOVA with Bonferroni post-test, with \*\*\*\* p < 0.0001, \*\*\*p < 0.001, \*p < 0.05 (n=6)

Besides the 2PA spectra of the substances, which is vital to establish the optimal working window, also the localization of the PS is of crucial importance. Since most PS are fluorescent, a confocal laser scanning microscope (LSM) can be used to determine their accumulation. The PS were incubated with MG63 osteosarcoma cells using a 2D monolayer culture to monitor the cellular uptake. Eosin Y did not enter the cell membrane, while both TPP and P2CK can be traced within the cells (**Figure 52**). These results suggest that Eosin Y might not work efficiently as a PDT agent. On the other hand, both P2CK and TPP show high potential for TPE-PDT based on their accumulation inside the cells in combination with their higher  $\sigma_{2PA}$  at relevant wavelengths.

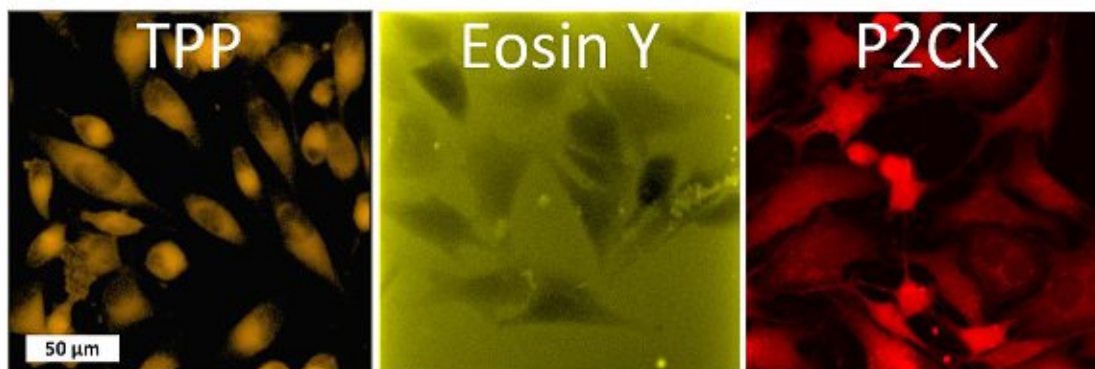


**Figure 52.** Accumulation of PS in the cells. MG63 cells were incubated with the substances for 4 h prior to imaging with a confocal laser scanning microscope. TPP and P2CK both accumulated in the cells, while Eosin Y stayed mainly in the surrounding media. Concentrations of 0.5 mM P2CK, 0.25 mM Eosin Y, and 0.6  $\mu$ M TPP were used for the localization experiments.

Once the biocompatible concentrations of the TPE-PS were established for dark conditions, MG63 cells, encapsulated in Gel-NB hydrogel using the previously described procedure, were exposed to laser irradiation in presence or absence of the TPE-PS. Each well was irradiated for 10 min using a peak intensity of 550 GW cm<sup>-1</sup> at respective wavelengths. Due to the low output of the laser in case of longer wavelengths (960 nm), only TPP and P2CK were used for quantitative assessment of the phototoxicity caused by irradiation. The wells were irradiated using a 2.5x objective with a NA of 0.085. Therefore, the volumetric pixel (voxel) is expected to be over 100-fold larger than in the case of the 10x objective, enabling a very high scanning speed of 4 m s<sup>-1</sup> and the exposure of the whole well at the same time (**Table 3**). This permits the simple comparison of different compounds using Presto Blue Assay, rendering the high throughput screening possible. Control wells which were only treated with 720 nm and 850 nm laser light in the absence of PS did not differ in cell viability compared to the non-irradiated controls, but both 0.5 mM P2CK and 0.6  $\mu$ M TPP exhibited significant phototoxicity on the cancer cells, leading to a viability of 27% and 15%, respectively (**Figure 53**). In case of P2CK this could be translated to a 65% and for TPP a 75% decrease in cell viability upon irradiation with their optimal wavelengths when compared to the dark conditions.



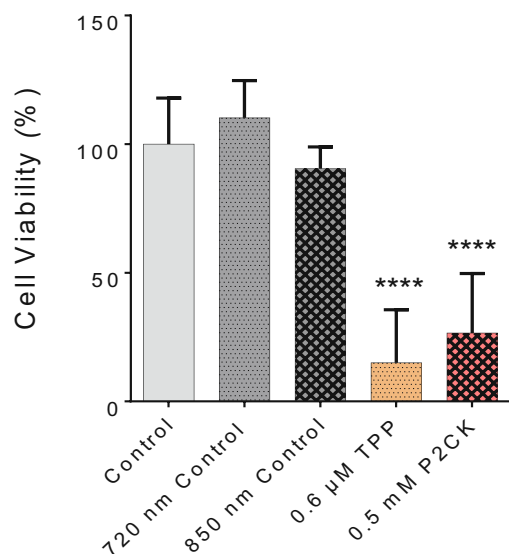


**Figure 53. Phototoxicity of PS.** The control sample was not irradiated, while the TPP sample was irradiated with 720 nm and the P2CK sample with 850 nm laser with a peak intensity of  $550 \text{ GW cm}^{-2}$  and a scanning speed of  $4 \text{ m s}^{-1}$ . Irradiation time per well was 10 min. The statistical significance was addressed by one-way ANOVA with Bonferroni post-test, with \*\*\*\*  $p < 0.0001$ .

One of the main advantages that TPE-PDT has to offer in comparison to conventional PDT is that the cellular damage can be reduced to the highly localized irradiated region, while conventional PDT can cause cell death in the surrounding tissue as well. The precision of the irradiation is dependent on the spot size of the laser, which is reliant on the numerical aperture of the objective. As a result, the irradiated volume can be kept relatively small when using a 10x objective with 0.3 NA (**Table 3**). As a proof of principle of the high spatiotemporal control, mCherry labelled MG63 spheroids (red) were encapsulated in a single cell suspension of GFP-labelled ASC/TERT cells (green). Only the spheroids were irradiated in the presence of the respective PS. As the cells are already fluorescently labelled, no additional live-dead staining was required to address the cell viability. If the cellular damage is caused by TPE-PDT the damage will only appear in the irradiated regions, and if the interaction is mediated by one-photon absorption, the surrounding green cells will be impaired as well. The controls irradiated with 720 nm, 850 nm and 960 nm with a peak intensity of  $700 \text{ GW cm}^{-2}$  showed no negative effect on cell viability (**Figure 54**). 0.25 mM Eosin Y irradiated at 960 nm also did not affect the cell viability. The green halo around the spheroids in the Eosin Y sample is probably a result from localized Eosin Y grafting into the hydrogel upon irradiation. The low efficiency of Eosin Y can be explained by its low cellular



uptake (**Figure 52**) and its low two-photon absorption in the spectral region accessible by the setup. Our study demonstrates that Eosin Y can be used in the presence of cells without significantly harming them. P2CK (0.5 mM) on the other hand causes substantial damage to the MG63 cell spheroid, both at 720 nm and 850 nm, as it has a relatively high  $\sigma_{2PA}$  at both these wavelengths (i.e. 292 GM and 405 GM respectively). At 960 nm, where its  $\sigma_{2PA}$  (66 GM) is low, the spheroids remained intact. In the presence of TPP, MG63 spheroids were completely eliminated at 720 nm where TPP has a  $\sigma_{2PA}$  as high as 8865 GM, while no significant damage was caused at the higher wavelengths at which the  $\sigma_{2PA}$  of TPP was below 100 GM (**Figure 55**). When compared to a common chemotherapeutic agent, cisplatin, the cell damage could be successfully restricted to the irradiated regions (**Figure 56**), demonstrating the benefit of TPE-PDT in terms of localized targeted treatment.

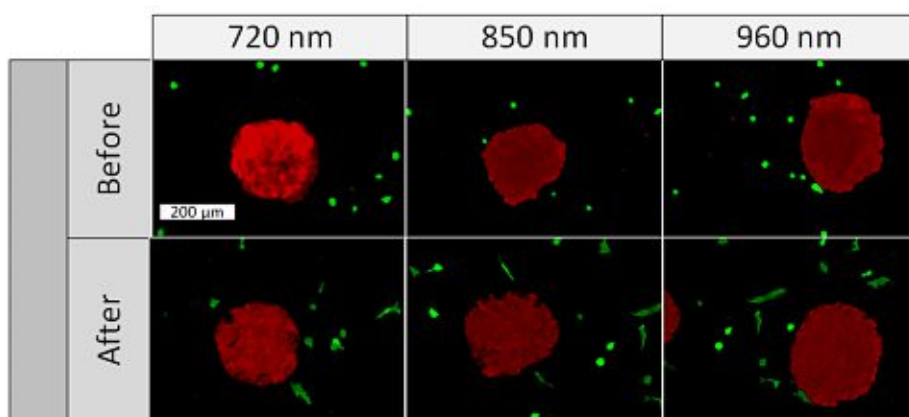


**Figure 54.** Cell viability before and after irradiation with different wavelengths (720 nm, 850 nm and 960 nm). None of the applied wavelengths caused cell damage.

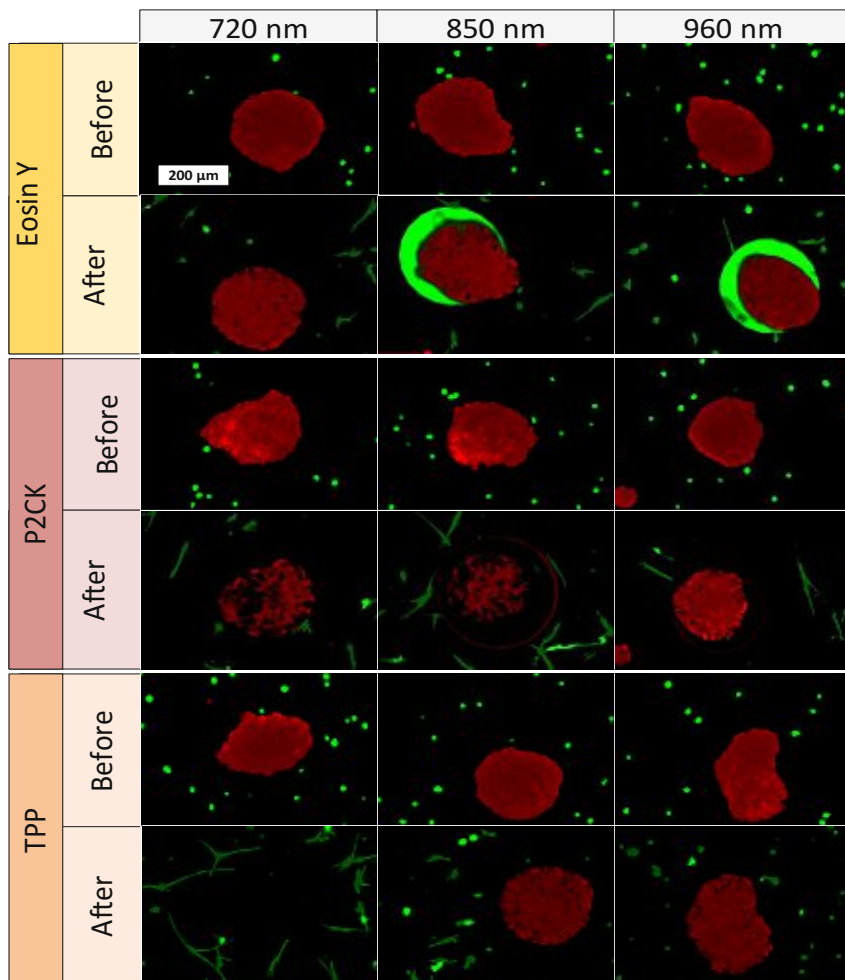


**Figure 55.** TPE-PDT treatment of mCherry MG63 spheroids (red) surrounded with ASC-GFP single cells (green). The before pictures were taken right after encapsulation of the cells. The irradiations of the samples were performed using different wavelengths of laser light. The region of irradiation was concentrated to the spheroids. One spheroid ( $\varnothing$  200  $\mu$ m) was irradiated for 3 min using a peak intensity of 700 GW cm<sup>2</sup>. The after photos were taken 48 h after treatment. Choosing the optimum wavelength of TPE-PS can increase the performance of the substances drastically. Eosin Y, even when it was irradiated at the optimal wavelength (960 nm and 58 GM) did not cause damage to cells. P2CK on the other hand caused damage both at 720 nm and 850 nm (296 GM and 405 GM, respectively). TPP eliminated the cancer cells completely when used at 720 nm (8865 GM) but not when it was irradiated with longer wavelengths, where its absorption is much lower (approximately 140 GM at 850 nm).

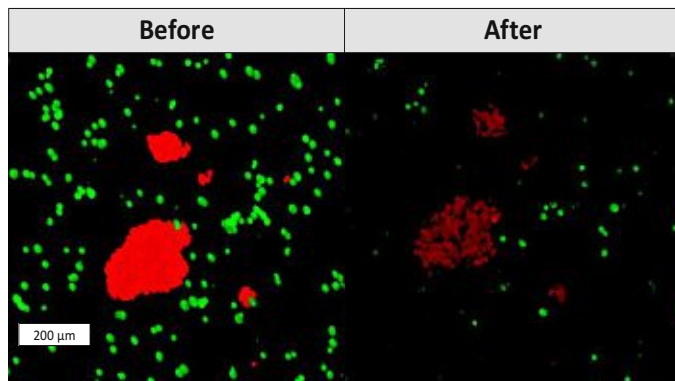


**Figure 56.** Cell viability after treatment with 30  $\mu$ M cisplatin. Cisplatin affects both the viability of the ASC and MG63 cells.

### 3.3.5 Conclusion

In this study we presented a systematic in vitro screening platform for TPE-PS. The automated z-scan setup enabled the determination of the two-photon absorption spectra of the TPE-PS investigated, providing indications about the optimal working window for each compound. Our results also demonstrated that the localization and the  $\sigma_{2PA}$  of TPE-PS is of crucial importance for the PDT efficacy. Additionally, TPE-PDT efficacy was quantified using a 3D model via Presto Blue metabolic assay, showing a significant reduction in cell viability after 2P irradiation in the presence of both P2CK and TPP. We were able to demonstrate the spatiotemporal control of TPE-PS using a 3D co-culture tumour model. The precision of TPE-PDT was evaluated by irradiating exclusively the osteosarcoma cells. In contrast to the use of cisplatin no collateral damage to non-irradiated regions was observed. Our pre-screening approach enables high throughput profiling of TPE-PS, thereby allowing the comprehensive analysis of PS efficacy in vitro.

## 3.4 T-cell Activation in 3D microenvironments

### 3.4.1 Introduction

T-cell activation plays a crucial role in adaptive immunity. Antigen presenting cells (APCs) present peculiar peptide bound to major histocompatibility complexes (pMHC) to which T-cells can bind to via their specific T-cell antigen receptors (TCRs), which in turn it recruits other molecules to initiate a signalling cascade. Apart from TCR-pMHC interactions, other molecules are required for the activation, for example co-receptors CD4/8 (facilitates the recognition process) and co-stimulatory molecule engagements of LFA-1, CD28, CTLA-4, CD2, CD45.<sup>249,250</sup> T-cell activation processes, including immunological synapse formation, cellular polarization, receptor sequestration and signalling are regulated by the cytoskeleton motility. The supra-molecular activation complexes (SMAC) contain of a central region (cSMAC) which shows high density of TCRs and its downstream effector protein kinase C (PKC- $\theta$ ) and a peripheral region (pSMAC) where the adhesion predominantly appears. Once a T-cell is activated, surface molecules from all over are recruited and transported to the nascent immunological synapse. A similar transport concerning lipid drafts was observed as TCR engagements also promote aggregation of lipid rafts which in turn facilitate interactions with signalling proteins, such as LAT, ZAP70 and Lck.<sup>251</sup> Spatial organization plays an important role in cell signalling and co-stimulation of T-cell activation. It has been showed that T-cells are sensitive to microscale separation of T-cell receptors C3 and CD28 and to the mechanical stiffness of stimulatory substrate presenting ligands to these.<sup>252</sup>

Most of the studies concerning T-cell antigen recognition and kinetics were mainly performed on 2D systems, such as Förster resonance energy transfer microscopy (FRET) and single-molecule mechanical assays.<sup>249</sup> 2PP is a powerful tool to fabricate high resolution 3D structures and by using a photosensitive sol-gel hybrid material, high optical quality, and good mechanical and chemical stability can be achieved. One of the materials that had been tested successfully for 2PP applications is a zirconium/silicon composite (MAPTMS:ZPO) which shows minimal shrinkage upon structuring and possesses glass-like properties.<sup>253</sup>

### 3.4.2 Aim

The aim of this project was to find a suitable material which has the capacity to non-specifically absorb antibodies and proteins while having low auto-fluorescence thereby

allowing the imaging of the labelled antibodies. After establishing the material processing, the aim was to create microstructures with well-defined parameters and absorb antibodies on the surface and study T-cell activation upon different stimuli.

### 3.4.3 Experimental

#### 3.4.3.1 *Surface Coating*

Glass cover slides were plasma treated and were methacrylated prior to the coating. Undiluted OrmoComp was used to create an approximately 10  $\mu\text{M}$  thick coating was illuminated for 5 min under UV irradiation at 365 nm. Afterwards the surface was washed with the developer solution (1 :1 solution of 4-methyl-2-pentanone and 2-propanol) and was dried before the addition of Mix&Go reagent (Anteo) for 30 min. Finally, the surface was washed and was incubated with a mixture of goat anti-mouse IgG-AlexaFlour647 and GFP Tag Polyclonal antibody AlexaFlour555 (1:1000) for one hour, and pictures were recorded using LSM with 63x oil immersion objective.

#### 3.4.3.2 *Mitochondria Staining*

The mitochondria staining was performed with MitoBeacon Orange (GeneCopoeia) according to the manufacturer's protocol. Different concentrations ranging from 31 nM to 500 nM was tested.

#### 3.4.3.3 *Live-Actin Staining*

AS a live actin stain, LifeAct (Ibidi) was used according to the manufacturer's protocol. For transfection via membrane fusion Fuse-It-P (Ibidi) was used.

#### 3.4.3.4 *Microplate Structuring*

The microplates were printed using the following parameters; 800 nm structuring wavelength, a 100  $\text{mm s}^{-1}$  writing speed, 50 mW laser power, hatch and layer spacing of 0.5  $\mu\text{m}$  using a 10x 0.3 NA objective. In preparation for calcium microscopy the microplates were treated with Mix&Go. Antibodies CD3, CD28, a 1:1 mixture and as a control fibronectin, each applied for 30 min.

#### 3.4.3.5 *Calcium Imaging*

Fura-2 dye was used for the ratiometric calcium imaging. The dye is excited by alternating at 340 nm and 380 nm and the emitting signals at 510 nm were recorded for 1000 frames per each wavelength. The data was analysed with Image-J by

calculating the ratio of each pixel of two consecutive pictures. Afterwards, the images were overlaid.

### 3.4.3.6 Results and Discussion

Several different materials were tested as coating for antibody absorption, including PEGDMA (low absorbance), zirconium hybrid with 4'4-bis photoinitiator (high auto-fluorescence) and ETA/TTA (low adhesion onto methacrylated glass). OrmoComp hybrid polymer was proposed as a material structuring due to its glass like properties and low auto-fluorescence (**Table 4**). The results show that the plasma treatment improved the uniform distribution of antibodies when compared to methacrylated glass, and the OrmoComp material showed a less homogenous non-specific absorption, which could possibly be improved by plasma treatment of the material after UV-polymerization (**Figure 57**).

**Table 4. OrmoComp parameters obtained from the manufacturer's website.**

Parameter	OrmoComp®
Viscosity	2 ± 0.5 Pa•s
Resolution	Down to 100 nm feature sizes
Thermal stability	Up to 270 °C (short term)
Volume shrinkage	5 – 7 %
Refractive index (589 nm, cured)	1.520
Replication with PDMS molds (no oxygen sensitivity)	Yes
Shelf-life	6 months
Solvent-free	Yes, ready-to-use solutions



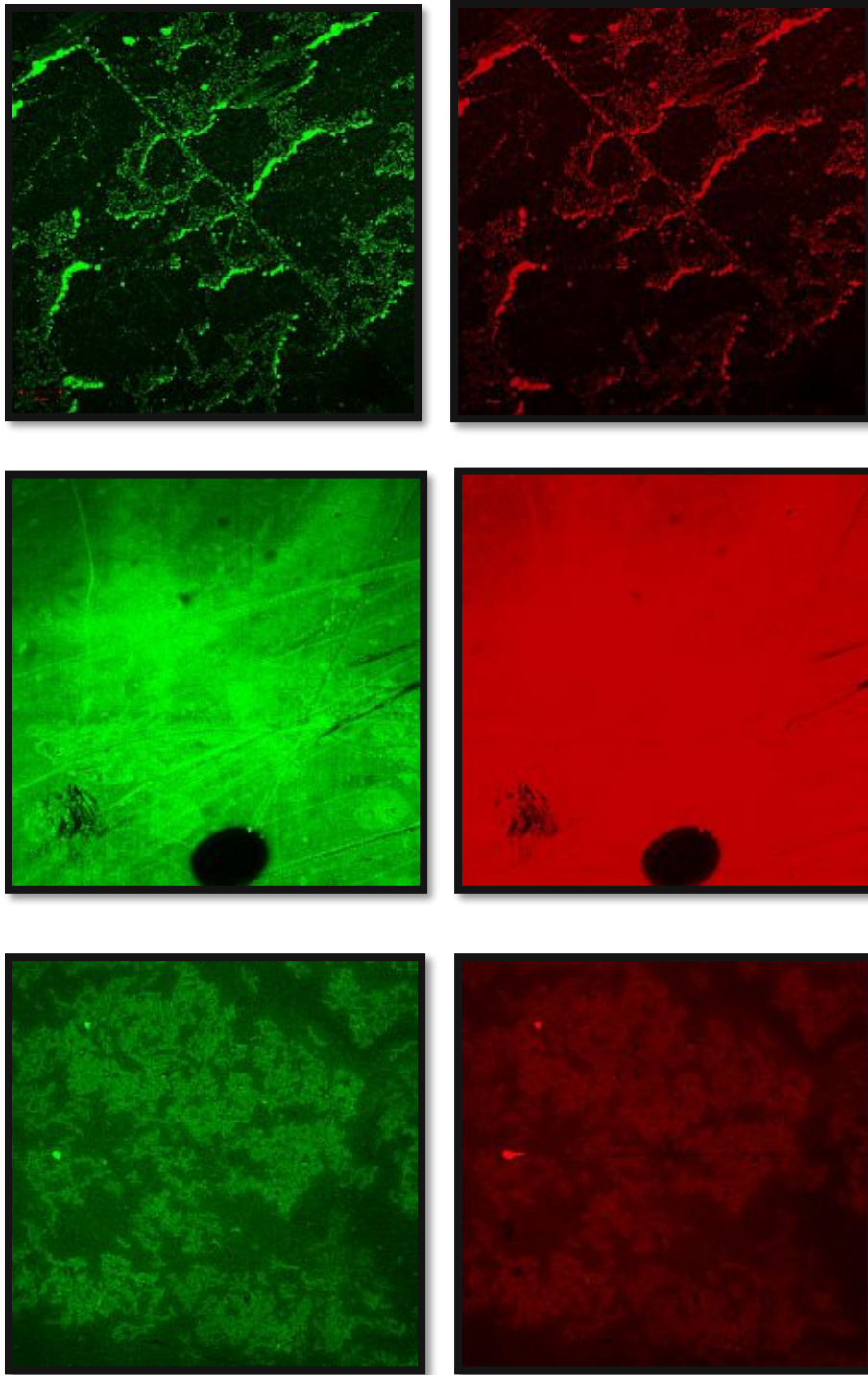


**Figure 57. (First row) Methacrylated glass without plasma treatment samples showing non uniform distribution of the antibodies. (Second row) Plasma treated methacrylated glass shows uniform distribution of antibodies. (Third row) OrmComp material absorbs antibodies similarly to control, although less uniform.**

Jurkat immortalized T-lymphocyte cells (provided by the Biophysics group, TU Wien) were used throughout the experiments, and four different sized chambers will be

printed and tested; 10x10  $\mu\text{m}$ , 15x15  $\mu\text{m}$ , 20x20  $\mu\text{m}$ , and 30x30  $\mu\text{m}$ . The wall between the chambers were set as 5  $\mu\text{m}$ , and one plate consisted of 25 chambers (**Figure 58**). OrmoComp material can be used directly in 2PP system without additional photoinitiator. First, the 30x30  $\mu\text{m}$  were printed and the above-mentioned antibodies were incubated after the application of Mix&Go reagent, and the structures were visualized using LSM. Although the absorption was not fully uniform, it could be improved via longer incubation and by applying gentle shaking (**Figure 59**).

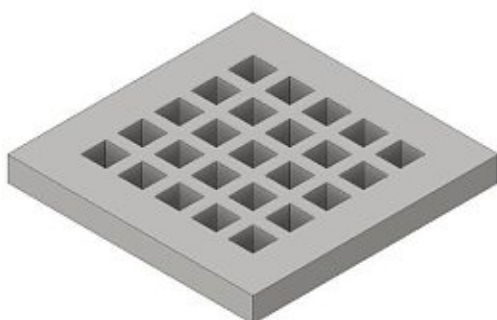


**Figure 58.** CAD picture of the designed microplates.

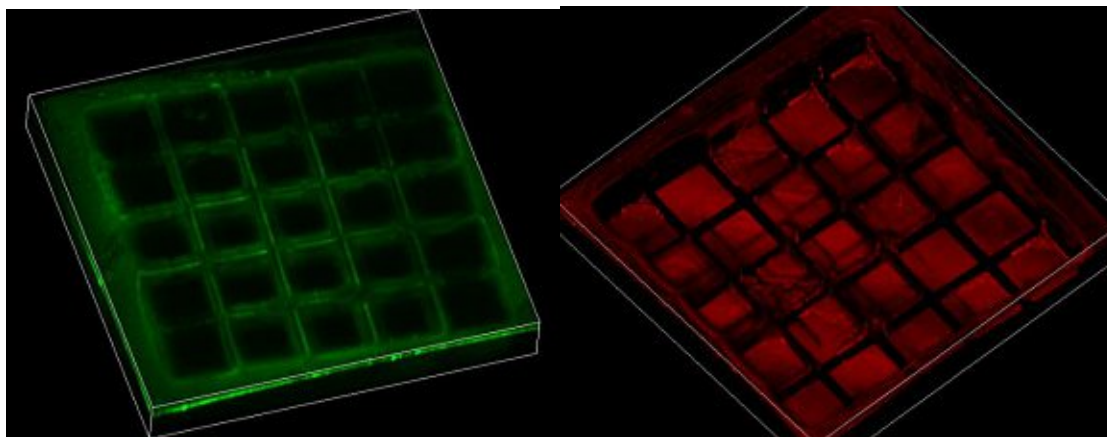
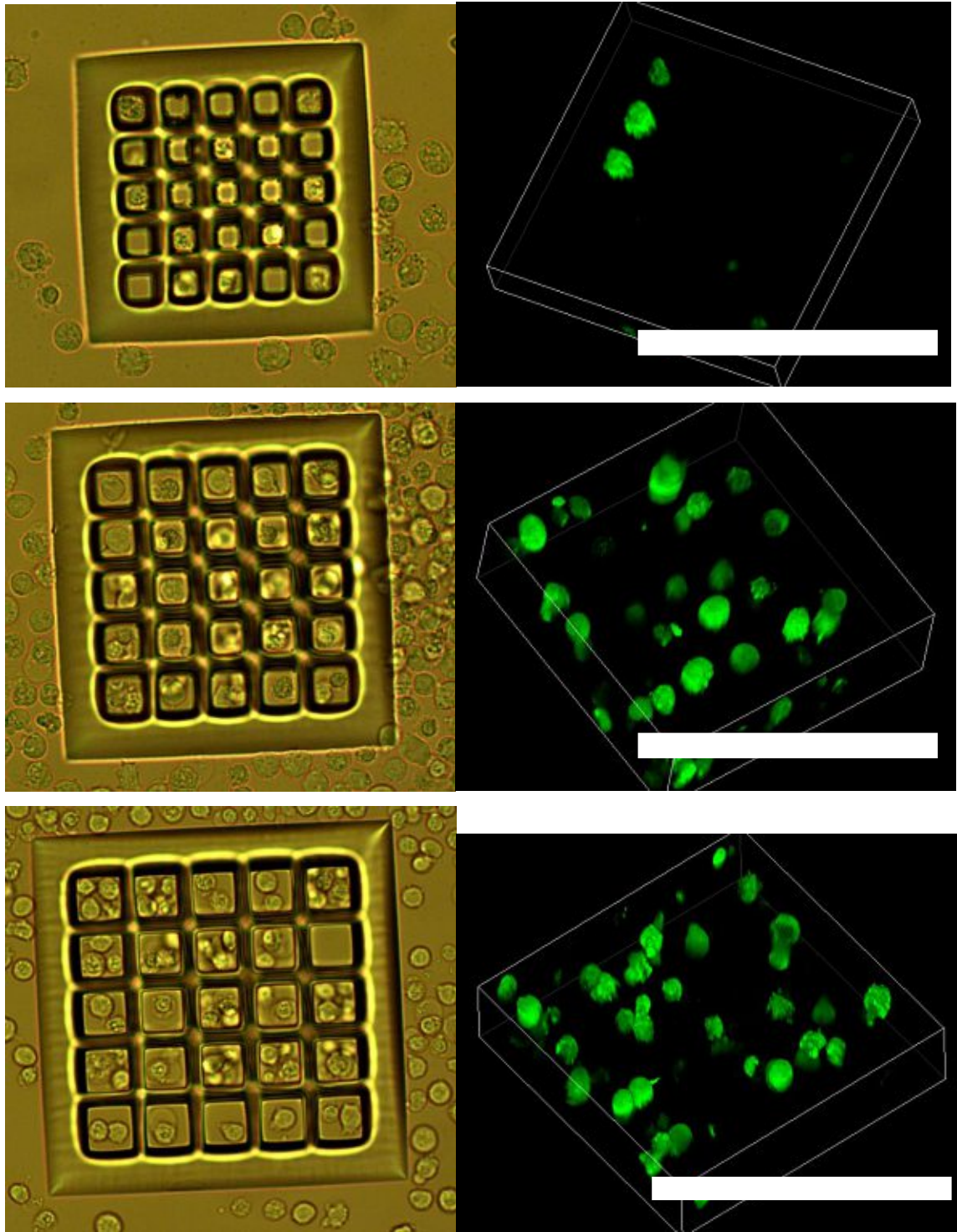


**Figure 59.** LSM pictures of the microplates visualized by the absorption of the antibodies.

Afterwards, GFP-Jurkat cells were used to determine the desired dimensionality of the microplates. After the printing and development of the microplates suspension Jurkat cells (1 million/mL) were added onto the surface for 15 min to sink to the bottom before

imaging (**Figure 60**). Based on uniform cell distribution a well size around 15  $\mu\text{m}$  is optimal (**Figure 61**).



Die approbierte gedruckte Originalversion dieser Dissertation ist an der TU Wien Bibliothek verfügbar.  
The approved original version of this doctoral thesis is available in print at TU Wien Bibliothek.



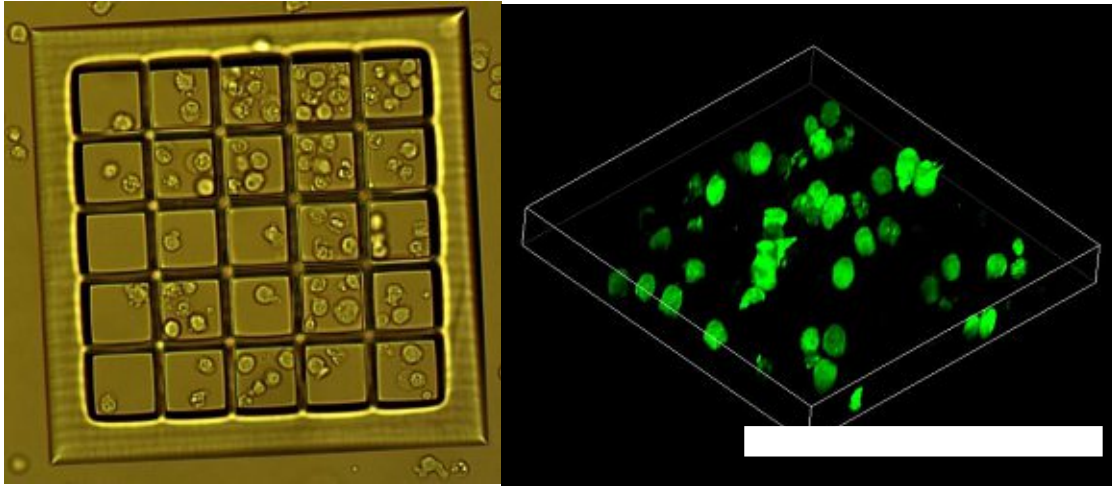


Figure 60. Jurkat cells seeded in the microplate. The most single cells/plate were archived with the 15  $\mu\text{m}$  well sized microplate. The 20 and 30  $\mu\text{m}$  lead to multiple cells/well, while the 10  $\mu\text{m}$  was too small for the cells to sediment down.

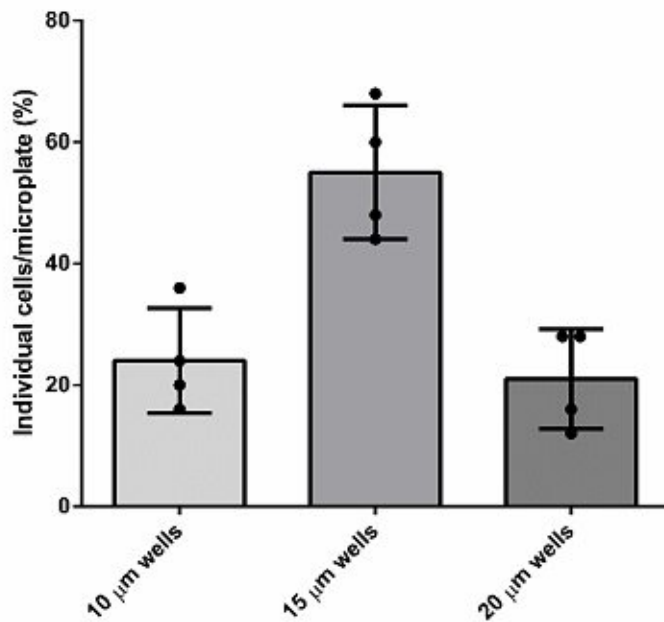
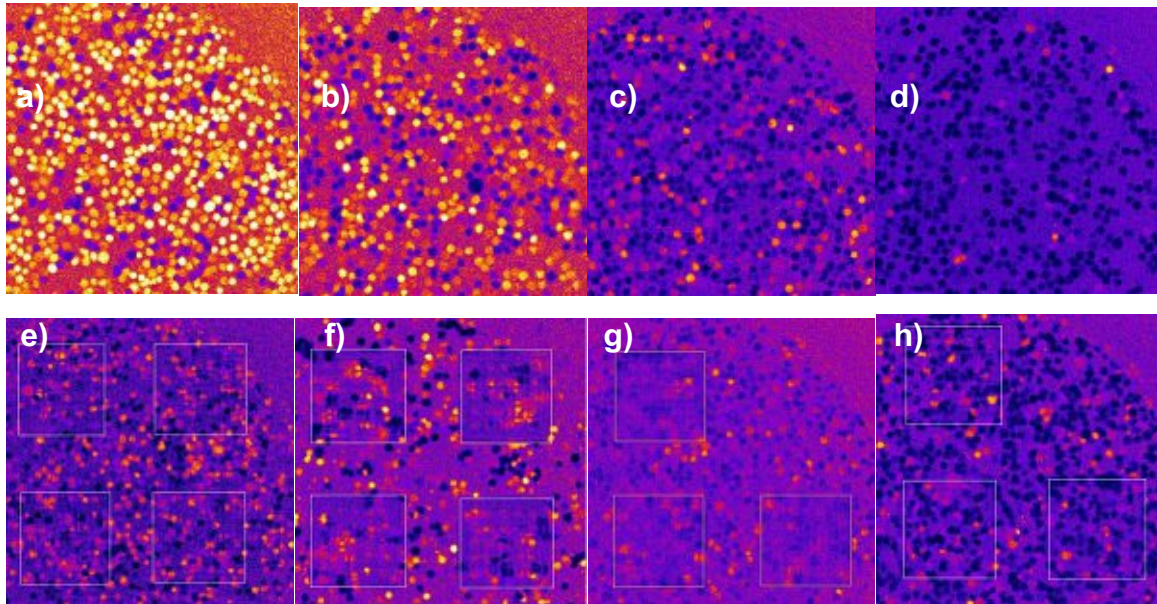


Figure 61. Number of individual Jurkat cells/microwell. 15  $\mu\text{m}$  pores proved to be the most useful for the entrapping of single cells.

In order to study the activation of Jurkat cells, three different conditions were applied, one with fibronectin coating (adhesion, but no activation), CD28 and CD3 and the combination of the two. The previously prepared microwells were coated with the antibodies using the previously mentioned protocol and cells were recorded using  $\text{Ca}^{2+}$  setup. For the ratiometric calcium imaging a glass cover slide was used as a 2D control. A qualitative analysis of 1000 frames (**Figure 62a-d**) showed the expected results with the highest level of activation with the combination of co-stimulatory CD28

and CD3, high activation with CD3, while CD28 alone and fibronectin did not induce the activation of Jurkat cells. The 3D experiments (**Figure 62e-f**) exhibits similar patterns similar results, but the background signal was increased compared to the 2D control, possibly due to insufficient washing during sample preparation.



**Figure 62.** Calcium Imaging of glass (top row, a: CD3 and CD28, b: CD3 alone, c: CD28 alone, and d: Fibronectin) and 3D substrate (bottom row, e: CD3 and CD28, f: CD3 alone, g: CD28 alone, and h: Fibronectin).

Mitochondria and actin staining were tested on Jurkat cells as well. Different concentrations of mitochondria staining were applied. The best signal was achieved with 62 nM and 125 nM of staining solution (**Figure 63**). Higher concentration of the staining led to the staining of the whole cells not only the mitochondria (e.g. 500 nM). However, the live actin staining showed weak signal which faded completely within the course of the experiment.

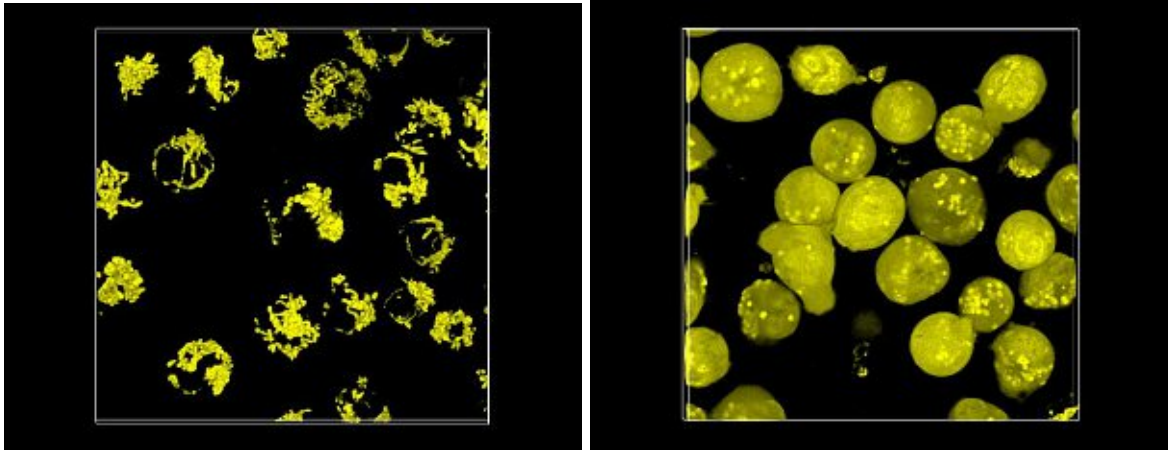


Figure 63. MitoBeacon staining of mitochondria using 62 nM (left) or 500 nM staining solution in Jurkat cells.

#### 3.4.4 Conclusion

OrmoComp material showed good processability and optical properties for microplate structuring. It also showed non-specific absorption properties that was similar to glass. Furthermore, Jurkat cells showed similar activation pattern compared to 2D glass surfaces, however for quantitative analysis an improvement of the applied cell preparation protocol has to be implemented. The mitochondria staining of the Jurkat cells was successful but an actin staining that meets the requirements of the experiment has to be established.

## 4 Conclusion

Throughout this PhD project we were able to successfully demonstrate the possibility to use 2PP for direct embedding of cells into bioinks and could be employed for the production of 3D cell-based applications. We have developed different bioink compositions using a novel biocompatible diazosulfonate photoinitiator DAS. The possible concentrations for biofabrication were optimized together with different gelatin derivatives including chain-growth hydrogels such as GelMOD and step-growth polymers as GelNB and GelNB-GelSH. The use of step growth hydrogels with DAS enabled high-definition bioprinting. Due to the ideal behaviour and associated fast crosslinking kinetics of this material, a wide range of processing parameters (laser power and writing speed) is supported without a strong variation the mechanical properties of the produced hydrogels. Different properties of the material such as degradation rate, swelling and stiffness can be fine-tuned by varying the applied laser power. Compared to scaffold seeding a more uniform cell loading and higher cell densities can be achieved via high definition bioprinting regardless the pore size.

We have also demonstrated the capacity of gel-NB-gel-SH thiol-ene photo-click hydrogels to support endothelial cell adhesion and proliferation both in a single cell suspension and spheroid culture via UV encapsulation. We used this bioink composition to improve both the accuracy and the throughput of the printing process. The spherical aberrations caused by the refractive index mismatch and the focusing depth was modelled by a custom-made algorithm, and the effect of the voxel compensation was demonstrated. Additionally, the two different printing modes, the top-down and bottom-up approach were compared to further optimize the resolution of high structures. The capacity of 2PP to create vascular structures within a microfluidic chip was tested with two different settings, first as a one-pot method, including both the supporting cells and the endothelial cell spheroids in the bioink, and as a supporting cell scaffold barrier to drop-seed the HUVECs spheroids after developing the structures.

We have also demonstrated the application of 2PP for bioprinting of a GBM-on-chip. A medical grade biocompatible pressure sensitive double-sided tape was used instead



of PDMS to produce the mold which can be mounted on high precision glass slide to enable the direct HD bioprinting of the membrane and the optical imaging of the channels. Both the endothelial cells and astrocytes cells showed good viability and monolayer formation after 2 day of seeding, and the embedded pericytes maintained their cell viability after embedding in the bioink. The membrane was characterized by the diffusion of different sized molecules across the membrane and it showed a size dependent perfusion rate of the different fluorescent substances. When the membrane was seeded with cells the diffusion rates decreased in all cases. This GBM construct could enable the screening of possible drugs and therapeutics and their transport through the BBB in order to improve the currently available treatment option and delivery strategies and gain more understanding in the disease progression.

During this PhD project we also presented a systematic *in vitro* screening platform for TPE-PS. The automated z-scan setup enabled the determination of the two-photon absorption spectra of the TPE-PS investigated, providing indications about the optimal working window for each compound. The precision of TPE-PDT was evaluated by irradiating exclusively the osteosarcoma cells. In contrast to the use of cisplatin no collateral damage to non-irradiated regions was observed. Our pre-screening approach enables high throughput profiling of TPE-PS, thereby allowing the comprehensive analysis of PS efficacy *in vitro*.

## 5 Bibliography

1. Wong, C. H., Siah, K. W. & Lo, A. W. Estimation of clinical trial success rates and related parameters. *Biostatistics* **20**, 273–286 (2019).
2. Mak, I. W. Y., Evaniew, N. & Ghert, M. Lost in translation: Animal models and clinical trials in cancer treatment. *American Journal of Translational Research* **6**, 114–118 (2014).
3. Ledford, H. Translational research: 4 ways to fix the clinical trial. *Nature* **477**, 526–528 (2011).
4. Törnqvist, E. *et al.* Strategic Focus on 3R Principles Reveals Major Reductions in the Use of Animals in Pharmaceutical Toxicity Testing. *PLoS One* **9**, e101638 (2014).
5. Antoni, D., Burckel, H., Josset, E. & Noel, G. Three-dimensional cell culture: a breakthrough in vivo. *Int. J. Mol. Sci.* **16**, 5517–27 (2015).
6. Cukierman, E., Pankov, R., Stevens, D. R. & Yamada, K. M. Taking Cell-Matrix Adhesions to the Third Dimension. *Science (80-. )*. **294**, 1708–1712 (2001).
7. Nyga, A., Cheema, U. & Loizidou, M. 3D tumour models: Novel in vitro approaches to cancer studies. *J. Cell Commun. Signal.* **5**, 239–248 (2011).
8. Breslin, S. & O'Driscoll, L. The relevance of using 3D cell cultures, in addition to 2D monolayer cultures, when evaluating breast cancer drug sensitivity and resistance. *Oncotarget* **7**, 45745–45756 (2016).
9. Melissaridou, S. *et al.* The effect of 2D and 3D cell cultures on treatment response, EMT profile and stem cell features in head and neck cancer. *Cancer Cell Int.* **19**, 16 (2019).
10. Friedrich, J., Seidel, C., Ebner, R. & Kunz-Schughart, L. A. Spheroid-based drug screen: considerations and practical approach. *Nat. Protoc.* **4**, 309–324 (2009).
11. Cannon, C. J. Approaches to corneal tissue engineering: Top-down or bottom-up? in *Procedia Engineering* **110**, 15–20 (Elsevier Ltd, 2015).
12. Lee, G. Y., Kenny, P. A., Lee, E. H. & Bissell, M. J. Three-dimensional culture models of normal and malignant breast epithelial cells. *Nat. Methods* **4**, 359–365

- (2007).
13. Napolitano, A. P. *et al.* Scaffold-free three-dimensional cell culture utilizing micromolded nonadhesive hydrogels. *Biotechniques* **43**, 494–500 (2007).
  14. De Moor, L. *et al.* High-throughput fabrication of vascularized spheroids for bioprinting. *Biofabrication* **10**, (2018).
  15. Glowacki, J. & Mizuno, S. Collagen scaffolds for tissue engineering. *Biopolymers* **89**, 338–344 (2008).
  16. Neves, M. I. *et al.* Molecularly Imprinted Intelligent Scaffolds for Tissue Engineering Applications. *Tissue Eng. Part B Rev.* **23**, 27–43 (2017).
  17. Elbert, D. L. Bottom-up tissue engineering. *Current Opinion in Biotechnology* **22**, 674–680 (2011).
  18. Ovsianikov, A., Yoo, J. & Mironov, V. *3D printing and biofabrication*. (Springer, 2018).
  19. Javaid, M. & Haleem, A. Additive manufacturing applications in orthopaedics: A review. *Journal of Clinical Orthopaedics and Trauma* **9**, 202–206 (2018).
  20. Shafiee, A. & Atala, A. Printing Technologies for Medical Applications. *Trends in Molecular Medicine* **22**, 254–265 (2016).
  21. Ozbolat, I. T. & Hospodiuk, M. Current advances and future perspectives in extrusion-based bioprinting. *Biomaterials* **76**, 321–343 (2016).
  22. Odde, D. J. & Renn, M. J. Laser-guided direct writing of living cells. *Biotechnol. Bioeng.* **67**, 312–318 (2000).
  23. Xu, T., Jin, J., Gregory, C., Hickman, J. J. & Boland, T. Inkjet printing of viable mammalian cells. *Biomaterials* **26**, 93–99 (2005).
  24. Nakamura, M. *et al.* Biocompatible inkjet printing technique for designed seeding of individual living cells. *Tissue Eng.* **11**, 1658–1666 (2005).
  25. Tasoglu, S. & Demirci, U. Bioprinting for stem cell research. *Trends Biotechnol.* **31**, 10–9 (2013).
  26. Murphy, S. V & Atala, A. 3D bioprinting of tissues and organs. *Nat. Biotechnol.* **32**, 773–785 (2014).

27. Zorlutuna, P., Jeong, J. H., Kong, H. & Bashir, R. Stereolithography-Based Hydrogel Microenvironments to Examine Cellular Interactions. *Adv. Funct. Mater.* **21**, 3642–3651 (2011).
28. Bártolo, P. J. *Stereolithography Materials, Processes and Applications*. Springer Science+Business Media (Springer US, 2011). doi:10.1007/978-0-387-92904-0\_2
29. Ovsianikov, A. *et al.* Laser fabrication of three-dimensional CAD scaffolds from photosensitive gelatin for applications in tissue engineering. *Biomacromolecules* **12**, 851–858 (2011).
30. Stampfl, J., Liska, R. & Ovsianikov, A. *Multiphoton lithography: techniques, materials and applications*. (Wiley-VCH Verlag GmbH & Co. KGaA).
31. Marino, A. *et al.* Two-Photon Lithography of 3D Nanocomposite Piezoelectric Scaffolds for Cell Stimulation. *ACS Appl. Mater. Interfaces* **7**, 25574–25579 (2015).
32. Nguyen, A. K. & Narayan, R. J. Two-photon polymerization for biological applications. *Mater. Today* **20**, 314–322 (2017).
33. Chichkov, B. N. & Ostendorf, A. Two-Photon Polymerization: A New Approach to Micromachining. *Photonics Spectra* **40**, 72–79 (2006).
34. Gungor-Ozkerim, P. S., Inci, I., Zhang, Y. S., Khademhosseini, A. & Dokmeci, M. R. Bioinks for 3D bioprinting: an overview. *Biomater. Sci.* **6**, 915–946 (2018).
35. Hölzl, K. *et al.* Bioink properties before, during and after 3D bioprinting. *Biofabrication* **8**, 032002 (2016).
36. Axpe, E. & Oyen, M. Applications of Alginate-Based Bioinks in 3D Bioprinting. *Int. J. Mol. Sci.* **17**, 1976 (2016).
37. Kobayashi, M. & Hyu, H. S. Development and evaluation of polyvinyl alcohol-hydrogels as an artificial articular cartilage for orthopedic implants. *Materials (Basel)*. **3**, 2753–2771 (2010).
38. Maitz, M. F. Applications of synthetic polymers in clinical medicine. *Biosurface and Biotribology* **1**, 161–176 (2015).
39. Zhu, J. & Marchant, R. E. Design properties of hydrogel tissue-engineering

- scaffolds. *Expert Rev. Med. Devices* **8**, 607–26 (2011).
40. Frantz, C., Stewart, K. M. & Weaver, V. M. The extracellular matrix at a glance. *J. Cell Sci.* **123**, 4195–4200 (2010).
  41. Kim, S. H., Turnbull, J. & Guimond, S. Extracellular matrix and cell signalling: The dynamic cooperation of integrin, proteoglycan and growth factor receptor. *J. Endocrinol.* **209**, 139–151 (2011).
  42. Sakai, S., Hirose, K., Taguchi, K., Ogushi, Y. & Kawakami, K. An injectable, in situ enzymatically gellable, gelatin derivative for drug delivery and tissue engineering. *Biomaterials* **30**, 3371–3377 (2009).
  43. Ahmed, E. M. Hydrogel: Preparation, characterization, and applications: A review. *J. Adv. Res.* **6**, 105–121 (2015).
  44. Jafari, B., Rafie, F. & Davaran, S. Preparation and characterization of a novel smart polymeric hydrogel for drug delivery of insulin. *BiolImpacts* **1**, 135–143 (2011).
  45. Hu, W., Wang, Z., Xiao, Y., Zhang, S. & Wang, J. Advances in crosslinking strategies of biomedical hydrogels. *Biomaterials Science* **7**, 843–855 (2019).
  46. Mendes-Felipe, C., Oliveira, J., Etxebarria, I., Vilas-Vilela, J. L. & Lanceros-Mendez, S. State-of-the-Art and Future Challenges of UV Curable Polymer-Based Smart Materials for Printing Technologies. *Adv. Mater. Technol.* **4**, 1800618 (2019).
  47. Whitby, R. *et al.* Photoinitiators for two-photon polymerisation: effect of branching and viscosity on polymerisation thresholds. *RSC Adv.* **7**, 13232–13239 (2017).
  48. Whitby, R. *et al.* Design, synthesis, and characterization of photoinitiators for two-photon polymerization. in *Active Photonic Materials VIII* (eds. Subramania, G. S. & Foteinopoulou, S.) **9920**, 992026 (SPIE, 2016).
  49. Bail, R. *et al.* The effect of a type I photoinitiator on cure kinetics and cell toxicity in projection-micromachining. in *Procedia CIRP* **5**, 222–225 (Elsevier B.V., 2013).
  50. Lalevée, J. *et al.* N-Heterocyclic Carbene Boranes Accelerate Type I Radical

- Photopolymerizations and Overcome Oxygen Inhibition. *Angew. Chemie Int. Ed.* **51**, 5958–5961 (2012).
51. Allen, N. S. *et al.* Photochemistry and photoinduced chemical crosslinking activity of type I & II co-reactive photoinitiators in acrylated prepolymers. *J. Photochem. Photobiol. A Chem.* **126**, 135–149 (1999).
  52. Tromayer, M. *et al.* A biocompatible macromolecular two-photon initiator based on hyaluronan. *Polym. Chem.* **8**, 451–460 (2017).
  53. Tromayer, M. *et al.* A biocompatible diazosulfonate initiator for direct encapsulation of human stem cells *via* two-photon polymerization. *Polym. Chem.* **9**, 3108–3117 (2018).
  54. Van Hoorick, J. *et al.* (Photo-)crosslinkable Gelatin Derivatives for Biofabrication Applications. *Acta Biomater.* **97**, 46–73 (2019).
  55. Van Den Bulcke, A. I. *et al.* Structural and Rheological Properties of Methacrylamide Modified Gelatin Hydrogels. *Biomacromolecules* **1**, 31–38 (2000).
  56. Yue, K. *et al.* Synthesis, properties, and biomedical applications of gelatin methacryloyl (GelMA) hydrogels. *Biomaterials* **73**, 254–271 (2015).
  57. Shih, H. & Lin, C.-C. Cross-Linking and Degradation of Step-Growth Hydrogels Formed by Thiol–Ene Photoclick Chemistry. *Biomacromolecules* **13**, 2003–2012 (2012).
  58. Lin, C. C., Ki, C. S. & Shih, H. Thiol-norbornene photoclick hydrogels for tissue engineering applications. *Journal of Applied Polymer Science* **132**, 41563 (2015).
  59. Hoyle, C. E. & Bowman, C. N. Thiol-Ene Click Chemistry. *Angew. Chemie Int. Ed.* **49**, 1540–1573 (2010).
  60. Nicodemus, G. D. & Bryant, S. J. Cell Encapsulation in Biodegradable Hydrogels for Tissue Engineering Applications. *Tissue Eng. Part B Rev.* **14**, 149–165 (2008).
  61. Bokhari, M., Carnachan, R. J., Cameron, N. R. & Przyborski, S. A. Culture of HepG2 liver cells on three dimensional polystyrene scaffolds enhances cell

- structure and function during toxicological challenge. *J. Anat.* **211**, 567–76 (2007).
62. Markovic, M. *et al.* Hybrid Tissue Engineering Scaffolds by Combination of Three-Dimensional Printing and Cell Photoencapsulation. *J. Nanotechnol. Eng. Med.* **6**, 021004 (2015).
63. Tong, M. H. *et al.* Multiphoton photochemical crosslinking-based fabrication of protein micropatterns with controllable mechanical properties for single cell traction force measurements. *Sci. Rep.* **6**, 20063 (2016).
64. Basu, S., Rodionov, V., Terasaki, M. & Campagnola, P. J. Multiphoton-excited microfabrication in live cells via Rose Bengal cross-linking of cytoplasmic proteins. *Opt. Lett.* **30**, 159–61 (2005).
65. Connell, J. L., Ritschdorff, E. T., Whiteley, M. & Shear, J. B. 3D printing of microscopic bacterial communities. *Proc. Natl. Acad. Sci. U. S. A.* **110**, 18380–5 (2013).
66. Fedorovich, N. E. *et al.* The effect of photopolymerization on stem cells embedded in hydrogels. *Biomaterials* **30**, 344–353 (2009).
67. Occhetta, P. *et al.* VA-086 methacrylate gelatine photopolymerizable hydrogels: A parametric study for highly biocompatible 3D cell embedding. *J. Biomed. Mater. Res. Part A* **103**, 2109–2117 (2015).
68. Fairbanks, B. D., Schwartz, M. P., Bowman, C. N. & Anseth, K. S. Photoinitiated polymerization of PEG-diacrylate with lithium phenyl-2,4,6-trimethylbenzoylphosphinate: polymerization rate and cytocompatibility. *Biomaterials* **30**, 6702–6707 (2009).
69. Schafer, K. J. *et al.* Two-photon absorption cross-sections of common photoinitiators. *J. Photochem. Photobiol. A Chem.* **162**, 497–502 (2004).
70. Pawlicki, M., Collins, H. A., Denning, R. G. & Anderson, H. L. Two-Photon Absorption and the Design of Two-Photon Dyes. *Angew. Chemie Int. Ed.* **48**, 3244–3266 (2009).
71. Li, Z. *et al.* Initiation efficiency and cytotoxicity of novel water-soluble two-photon photoinitiators for direct 3D microfabrication of hydrogels. *RSC Adv.* **3**, 15939



- (2013).
72. Ovsianikov, A. *et al.* Laser photofabrication of cell-containing hydrogel constructs. *Langmuir* **30**, 3787–3794 (2014).
  73. Nuyken, O., Kneppel, T. & Voit, B. Sulfur-containing azoinitiators and their properties. *Macromol. Chem. Phys.* **190**, 1015–1024 (1989).
  74. Boncler, M., Różalski, M., Krajewska, U., Podsedek, A. & Watala, C. Comparison of PrestoBlue and MTT assays of cellular viability in the assessment of anti-proliferative effects of plant extracts on human endothelial cells. *J. Pharmacol. Toxicol. Methods* **69**, 9–16 (2014).
  75. Cesarone, C. F., Bolognesi, C. & Santi, L. Improved microfluorometric DNA determination in biological material using 33258 Hoechst. *Anal. Biochem.* **100**, 188–197 (1979).
  76. Skulachev, V. P. Bioenergetic aspects of apoptosis, necrosis and mitoptosis. *Apoptosis* **11**, 473–485 (2006).
  77. Nita, M. & Grzybowski, A. The Role of the Reactive Oxygen Species and Oxidative Stress in the Pathomechanism of the Age-Related Ocular Diseases and Other Pathologies of the Anterior and Posterior Eye Segments in Adults. *Oxidative Medicine and Cellular Longevity* **2016**, (2016).
  78. Simon, H. U., Haj-Yehia, A. & Levi-Schaffer, F. Role of reactive oxygen species (ROS) in apoptosis induction. *Apoptosis* **5**, 415–418 (2000).
  79. Papa, S. & Skulachev, V. P. Reactive oxygen species, mitochondria, apoptosis and aging. *Mol. Cell. Biol.* **174**, 305–319 (1997).
  80. Czubak, K., Antosik, A., Cichon, N. & Zbikowska, H. M. Vitamin C and Trolox decrease oxidative stress and hemolysis in cold-stored human red blood cells. *Redox Rep.* **22**, 445–450 (2017).
  81. Frei, B. Ascorbic acid protects lipids in human plasma and low-density lipoprotein against oxidative damage. *Am. J. Clin. Nutr.* **54**, 1113S-1118S (1991).
  82. Vergauwen, H. *et al.* Trolox and ascorbic acid reduce direct and indirect oxidative stress in the IPEC-J2 cells, an In Vitro model for the porcine gastrointestinal tract. *PLoS One* **10**, e0120485 (2015).

83. Arrigoni, O. & De Tullio, M. C. Ascorbic acid: Much more than just an antioxidant. *Biochim. Biophys. Acta* **1569**, 1–9 (2002).
84. Meister, A. On the antioxidant effects of ascorbic acid and glutathione. *Biochem. Pharmacol.* **44**, 1905–1915 (1992).
85. Lin, C.-H., Lin, K.-F., Mar, K., Lee, S.-Y. & Lin, Y.-M. Antioxidant N Acetylcysteine and Glutathione Increase the Viability and Proliferation of MG63 Cells Encapsulated in the Gelatin Methacrylate/VA-086/Blue Light Hydrogel System. *Tissue Eng. Part C Methods* **22**, 792–800 (2016).
86. Forman, H. J., Zhang, H. & Rinna, A. Glutathione: Overview of its protective roles, measurement, and biosynthesis. *Mol. Aspects Med.* **30**, 1–12 (2009).
87. Marí, M., Morales, A., Colell, A., García-Ruiz, C. & Fernández-Checa, J. C. Mitochondrial glutathione, a key survival antioxidant. *Antioxidants and Redox Signaling* **11**, 2685–2700 (2009).
88. Aldini, G. *et al.* N-Acetylcysteine as an antioxidant and disulphide breaking agent: the reasons why. *Free Radic. Res.* **52**, 751–762 (2018).
89. Moldéus, P., Cotgreave, I. A. & Berggren, M. Lung protection by a thiol-containing antioxidant: N-acetylcysteine. *Respiration* **50**, 31–42 (1986).
90. Dekhuijzen, P. N. R. Antioxidant properties of N-acetylcysteine: Their relevance in relation to chronic obstructive pulmonary disease. *European Respiratory Journal* **23**, 629–636 (2004).
91. Inoue, M., Sakaguchi, N., Isuzugawa, K., Tani, H. & Ogihara, Y. Role of Reactive Oxygen Species in Gallic Acid-Induced Apoptosis. *Biol. Pharm. Bull.* **23**, 1153–1157 (2000).
92. Sohi, K. K., Mittal, N., Hundal, M. K. & Khanduja, K. L. Gallic acid, an antioxidant, exhibits antiapoptotic potential in normal human lymphocytes: A Bcl-2 independent mechanism. *J. Nutr. Sci. Vitaminol. (Tokyo)*. **49**, 221–7 (2003).
93. Aruoma, O. I., Murcia, A., Butler, J. & Halliwell, B. Evaluation of the Antioxidant and Prooxidant Actions of Gallic Acid and Its Derivatives. *J. Agric. Food Chem.* **41**, 1880–1885 (1993).
94. Jansen, T. & Daiber, A. Direct Antioxidant Properties of Bilirubin and Biliverdin.

- Is there a Role for Biliverdin Reductase? *Front. Pharmacol.* **3**, 30 (2012).
95. Feng, Q. *et al.* Electrospun Regenerated Cellulose Nanofibrous Membranes Surface-Grafted with Polymer Chains/Brushes via the Atom Transfer Radical Polymerization Method for Catalase Immobilization. *ACS Appl. Mater. Interfaces* **6**, 20958–20967 (2014).
96. Goyal, M. M. & Basak, A. Human catalase: Looking for complete identity. *Protein and Cell* **1**, 888–897 (2010).
97. Preston, T. J., Muller, W. J. & Singh, G. Scavenging of Extracellular H<sub>2</sub>O<sub>2</sub> by Catalase Inhibits the Proliferation of HER-2/Neu-transformed Rat-1 Fibroblasts through the Induction of a Stress Response. *J. Biol. Chem.* **276**, 9558–9564 (2001).
98. Lalevée, J., Dirani, A., El-Roz, M., Allonas, X. & Fouassier, J. P. Silanes as New Highly Efficient Co-initiators for Radical Polymerization in Aerated Media. *Macromolecules* **41**, 2003–2010 (2008).
99. Dolmans, D. E., Fukumura, D. & Jain, R. K. Photodynamic therapy for cancer. *Nat. Rev. Cancer* **3**, 380–387 (2003).
100. Pritchard, C. D. *et al.* An injectable thiol-acrylate poly(ethylene glycol) hydrogel for sustained release of methylprednisolone sodium succinate. *Biomaterials* **32**, 587–597 (2011).
101. Nilsson, C., Malmström, E., Johansson, M. & Trey, S. M. Dendrimers in thiol-ene crosslinked networks and the effect of subsequent generations on thermoset properties. *J. Polym. Sci. Part A Polym. Chem.* **47**, 589–601 (2009).
102. Xu, Y., Meng, F., Cheng, R. & Zhong, Z. Reduction-Sensitive Reversibly Crosslinked Biodegradable Micelles for Triggered Release of Doxorubicin. *Macromol. Biosci.* **9**, 1254–1261 (2009).
103. Muñoz, Z., Shih, H. & Lin, C.-C. Gelatin hydrogels formed by orthogonal thiol–norbornene photochemistry for cell encapsulation. *Biomater. Sci.* **2**, 1063–1072 (2014).
104. Nam, J. A. *et al.* Synthesis and Characterization of a Multi-Sensitive Crosslinked Injectable Hydrogel Based on Pluronic. *Macromol. Biosci.* **11**, (2011).

105. Wei, J., Wang, H., Jiang, X. & Yin, J. Novel Photosensitive Thio-Containing Polyurethane as Macrophotoinitiator Comprising Side-Chain Benzophenone and Co-Initiator Amine for Photopolymerization. *Macromolecules* **40**, 2344–2351 (2007).
106. Gómez, M. L., Avila, V., Montejano, H. A. & Previtali, C. M. A mechanistic and laser flash photolysis investigation of acrylamide polymerization photoinitiated by the three component system safranine-T/triethanolamine/diphenyliodonium chloride. *Polymer (Guildf)*. **44**, 2875–2881 (2003).
107. Neumann, M. G. & Rodrigues, M. R. The mechanism of the photoinitiation of the polymerization of MMA by the thionine-triethanolamine system. *Polymer (Guildf)*. **39**, 1657–1661 (1998).
108. Miri, A. K. *et al.* Effective bioprinting resolution in tissue model fabrication. *Lab Chip* **19**, 2019–2037 (2019).
109. Petrochenko, P. E. *et al.* Laser 3D Printing with Sub-Microscale Resolution of Porous Elastomeric Scaffolds for Supporting Human Bone Stem Cells. *Adv. Healthc. Mater.* **4**, 739–747 (2015).
110. Ovsianikov, A., Li, Z., Torgersen, J., Stampfl, J. & Liska, R. Selective functionalization of 3D matrices via multiphoton grafting and subsequent click chemistry. *Adv. Funct. Mater.* **22**, 3429–3433 (2012).
111. Gramlich, W. M., Kim, I. L. & Burdick, J. A. Synthesis and orthogonal photopatterning of hyaluronic acid hydrogels with thiol-norbornene chemistry. *Biomaterials* **34**, 9803–9811 (2013).
112. Van Vlierberghe, S., Schacht, E. & Dubruel, P. Reversible gelatin-based hydrogels: Finetuning of material properties. *Eur. Polym. J.* **47**, 1039–1047 (2011).
113. Van Hoorick, J. *et al.* Highly Reactive Thiol-Norbornene Photo-Click Hydrogels : Toward Improved Processability. *Macromol. Rapid Commun.* **39**, 1800181 (2018).
114. Baudis, S. *et al.* Modular material system for the microfabrication of biocompatible hydrogels based on thiol-ene-modified poly(vinyl alcohol). *J. Polym. Sci. Part A Polym. Chem.* **54**, 2060–2070 (2016).

115. Anderson, S. B., Lin, C.-C., Kuntzler, D. V. & Anseth, K. S. The performance of human mesenchymal stem cells encapsulated in cell-degradable polymer-peptide hydrogels. *Biomaterials* **32**, 3564–3574 (2011).
116. Qin, X.-H. *et al.* Three-dimensional microfabrication of protein hydrogels via two-photon-excited thiol-vinyl ester photopolymerization. *J. Polym. Sci. Part A Polym. Chem.* **51**, 4799–4810 (2013).
117. Steiger, W. *et al.* Fully automated z-scan setup based on a tunable fs-oscillator. *Opt. Mater. Express* **9**, 3567 (2019).
118. Knezevic, L. *et al.* Engineering Blood and Lymphatic Microvascular Networks in Fibrin Matrices. *Front. Bioeng. Biotechnol.* **5**, 25 (2017).
119. Hutter, J. L. & Bechhoefer, J. Calibration of atomic-force microscope tips. *Rev. Sci. Instrum.* **64**, 1868–73 (1993).
120. Kain, L. *et al.* Calibration of colloidal probes with atomic force microscopy for micromechanical assessment. *J. Mech. Behav. Biomed. Mater.* **85**, 225–236 (2018).
121. Neto, C. & Craig, V. S. Colloid Probe Characterization: Radius and Roughness Determination. *Langmuir* **17**, 2097–2099 (2001).
122. Oliver, W. C. & Pharr, G. M. An improved technique for determining hardness and elastic modulus using load and displacement sensing indentation experiments. *J. Mater. Res.* **7**, 1564–1583 (1992).
123. Van Hoorick, J. *et al.* Cross-Linkable Gelatins with Superior Mechanical Properties Through Carboxylic Acid Modification: Increasing the Two-Photon Polymerization Potential. *Biomacromolecules* **18**, 3260–3272 (2017).
124. Stevens, R., Stevens, L. & Price, N. C. The Stabilities of Various Thiol Compounds used in Protein Purifications. in *Biochemical Education* **11** (2) 70 (1983).
125. Fairbanks, B. D., Singh, S. P., Bowman, C. N. & Anseth, K. S. Photodegradable, photoadaptable hydrogels via radical-mediated disulfide fragmentation reaction. *Macromolecules* **44**, 2444–2450 (2011).
126. Greene, T., Lin, T., Andrisani, O. M. & Lin, C. Comparative study of visible light

- polymerized gelatin hydrogels for 3D culture of hepatic progenitor cells. *J. Appl. Polym. Sci.* **44585**, 1–10 (2017).
127. Aimetti, A. A., Machen, A. J. & Anseth, K. S. Poly(ethylene glycol) hydrogels formed by thiol-ene photopolymerization for enzyme-responsive protein delivery. *Biomaterials* **30**, 6048–6054 (2009).
128. Li, Y. & Kilian, K. A. Bridging the Gap: From 2D Cell Culture to 3D Microengineered Extracellular Matrices. *Adv. Healthc. Mater.* **4**, 2780–2796 (2015).
129. Skylar-Scott, M. A., Liu, M.-C., Wu, Y., Dixit, A. & Yanik, M. F. Guided Homing of Cells in Multi-Photon Microfabricated Bioscaffolds. *Adv. Healthc. Mater.* **5**, 1233–1243 (2016).
130. Scholzen, T. & Gerdes, J. The Ki-67 protein: From the known and the unknown. *J. Cell. Physiol.* **182**, 311–322 (2000).
131. Ehrbar, M. *et al.* Elucidating the role of matrix stiffness in 3D cell migration and remodeling. *Biophys. J.* **100**, 284–93 (2011).
132. Knight, E. & Przyborski, S. Advances in 3D cell culture technologies enabling tissue-like structures to be created *in vitro*. *J. Anat.* **227**, 746–756 (2015).
133. Ahmad, A. A. *et al.* Optimization of 3-D organotypic primary colonic cultures for organ-on-chip applications. *J. Biol. Eng.* **8**, 9 (2014).
134. Huh, D., Hamilton, G. A. & Ingber, D. E. From 3D cell culture to organs-on-chips. *Trends Cell Biol.* **21**, 745–754 (2011).
135. Drury, J. L. & Mooney, D. J. Hydrogels for tissue engineering: Scaffold design variables and applications. *Biomaterials* **24**, 4337–4351 (2003).
136. Ullah, F., Othman, M. B. H., Javed, F., Ahmad, Z. & Akil, H. M. Classification, processing and application of hydrogels: A review. *Mater. Sci. Eng. C* **57**, 414–433 (2015).
137. Kular, J. K., Basu, S. & Sharma, R. I. The extracellular matrix: Structure, composition, age-related differences, tools for analysis and applications for tissue engineering. *Journal of Tissue Engineering* **5**, 204173141455711 (2014).
138. Antoine, E. E., Vlachos, P. P. & Rylander, M. N. Tunable collagen I hydrogels for



- engineered physiological tissue micro-environments. *PLoS One* **10**, 1–19 (2015).
139. Deng, C. *et al.* Collagen and glycopolymer based hydrogel for potential corneal application. *Acta Biomater.* **6**, 187–194 (2010).
140. Suri, S. & Schmidt, C. E. Photopatterned collagen-hyaluronic acid interpenetrating polymer network hydrogels. *Acta Biomater.* **5**, 2385–2397 (2009).
141. Nikkhah, M. *et al.* Gelatin-Based Biomaterials For Tissue Engineering And Stem Cell Bioengineering. in *Biomaterials from Nature for Advanced Devices and Therapies* 37–62 (John Wiley & Sons, Inc., 2016). doi:10.1002/9781119126218.ch3
142. Dobos, A. *et al.* Thiol–Gelatin–Norbornene Bioink for Laser-Based High-Definition Bioprinting. *Adv. Healthc. Mater.* (2019). doi:10.1002/adhm.201900752
143. Rouwkema, J., Rivron, N. C. & van Blitterswijk, C. A. Vascularization in tissue engineering. *Trends Biotechnol.* **26**, 434–441 (2008).
144. Kim, J. J., Hou, L. & Huang, N. F. Vascularization of three-dimensional engineered tissues for regenerative medicine applications. *Acta Biomater.* **41**, 17–26 (2016).
145. Carmeliet, P. & Jain, R. K. Angiogenesis in cancer and other diseases. *Nature* **407**, 249–257 (2000).
146. Yuan, S. Y. & Rigor, R. R. *Regulation of Endothelial Barrier Function. Regulation of Endothelial Barrier Function* (Morgan & Claypool Life Sciences, 2010).
147. Burton, A. C. Relation of Structure to Function of the Tissues of the Wall of Blood Vessels. *Physiol. Rev.* **34**, 619–643 (1954).
148. Patan, S. Vasculogenesis and angiogenesis. *Cancer Treat. Res.* **117**, 3–32 (2004).
149. Gafni, Y. *et al.* Design of a Filamentous Polymeric Scaffold for *in Vivo* Guided Angiogenesis. *Tissue Eng.* **12**, 3021–3034 (2006).
150. Druecke, D. *et al.* Neovascularization of poly(ether ester) block-copolymer



- scaffolds in vivo: Long-term investigations using intravital fluorescent microscopy. *J. Biomed. Mater. Res.* **68A**, 10–18 (2004).
151. Bishop, E. T. *et al.* An in vitro model of angiogenesis: basic features. *Angiogenesis* **3**, 335–44 (1999).
152. Guzzardi, M. A., Vozzi, F. & Ahluwalia, A. D. Study of the Crosstalk Between Hepatocytes and Endothelial Cells Using a Novel Multicompartmental Bioreactor: A Comparison Between Connected Cultures and Cocultures. *Tissue Eng. Part A* **15**, 3635–3644 (2009).
153. Strassburg, S., Nienhueser, H., Björn Stark, G., Finkenzeller, G. & Torio-Padron, N. Co-culture of adipose derived stem cells and endothelial cells in fibrin induces angiogenesis and vasculogenesis in a chorioallantoic membrane model. *J. Tissue Eng. Regen. Med.* **10**, 496–506 (2016).
154. Lozito, T. P., Kuo, C. K., Taboas, J. M. & Tuan, R. S. Human mesenchymal stem cells express vascular cell phenotypes upon interaction with endothelial cell matrix. *J. Cell. Biochem.* **107**, 714–722 (2009).
155. Kirkpatrick, C. J., Fuchs, S. & Unger, R. E. Co-culture systems for vascularization — Learning from nature. *Adv. Drug Deliv. Rev.* **63**, 291–299 (2011).
156. Kim, S., Kim, W., Lim, S. & Jeon, J. S. Vasculature-On-A-Chip for In Vitro Disease Models. *Biengineering* **4**, (2017).
157. Baker, B. M., Trappmann, B., Stapleton, S. C., Toro, E. & Chen, C. S. Microfluidics embedded within extracellular matrix to define vascular architectures and pattern diffusive gradients. *Lab Chip* **13**, 3246–3252 (2013).
158. Chrobak, K. M., Potter, D. R. & Tien, J. Formation of perfused, functional microvascular tubes in vitro. *Microvasc. Res.* **71**, 185–196 (2006).
159. Datta, P., Ayan, B. & Ozbolat, I. T. Bioprinting for vascular and vascularized tissue biofabrication. *Acta Biomater.* **51**, 1–20 (2017).
160. Zhang, Y., Yu, Y. & Ozbolat, I. T. Direct Bioprinting of Vessel-Like Tubular Microfluidic Channels. *J. Nanotechnol. Eng. Med.* **4**, 020902 (2013).
161. Bertassoni, L. E. *et al.* Hydrogel bioprinted microchannel networks for vascularization of tissue engineering constructs. *Lab Chip* **14**, 2202–11 (2014).

162. Norotte, C., Marga, F. S., Niklason, L. E. & Forgacs, G. Scaffold-free vascular tissue engineering using bioprinting. *Biomaterials* **30**, 5910–5917 (2009).
163. Kucukgul, C. *et al.* 3D bioprinting of biomimetic aortic vascular constructs with self-supporting cells. *Biotechnol. Bioeng.* **112**, 811–821 (2015).
164. Zhou, X., Hou, Y. & Lin, J. A review on the processing accuracy of two-photon polymerization. *AIP Adv.* (2015). doi:10.1063/1.4916886
165. Benedikt, S. *et al.* Highly efficient water-soluble visible light photoinitiators. *J. Polym. Sci. Part A Polym. Chem.* **54**, 473–479 (2016).
166. Zipfel, W. R., Williams, R. M. & Webb, W. W. Nonlinear magic: multiphoton microscopy in the biosciences. *Nat. Biotechnol.* **21**, 1369–1377 (2003).
167. Nasse, M. J. & Woehl, J. C. Realistic modeling of the illumination point spread function in confocal scanning optical microscopy. *J. Opt. Soc. Am. A* **27**, 295 (2010).
168. Laschke, M. W. & Menger, M. D. Spheroids as vascularization units: From angiogenesis research to tissue engineering applications. *Biotechnol. Adv.* **35**, 782–791 (2017).
169. Booth, M. J. & Wilson, T. Refractive-index-mismatch induced aberrations in single-photon and two-photon microscopy and the use of aberration correction. *J. Biomed. Opt.* **6**, 266 (2001).
170. Billiet, T., Gevaert, E., De Schryver, T., Cornelissen, M. & Dubruel, P. The 3D printing of gelatin methacrylamide cell-laden tissue-engineered constructs with high cell viability. *Biomaterials* **35**, 49–62 (2014).
171. Ma, S. *et al.* Monodisperse collagen–gelatin beads as potential platforms for 3D cell culturing. *J. Mater. Chem. B* **1**, 5128 (2013).
172. Sun, H.-B., Takada, K., Kim, M.-S., Lee, K.-S. & Kawata, S. Scaling laws of voxels in two-photon photopolymerization nanofabrication. *Appl. Phys. Lett.* **83**, 1104–1106 (2003).
173. Yang, S., Graham, J., Kahn, J. W., Schwartz, E. A. & Gerritsen, M. E. Functional roles for PECAM-1 (CD31) and VE-cadherin (CD144) in tube assembly and lumen formation in three-dimensional collagen gels. *Am. J. Pathol.* **155**, 887–95

- (1999).
174. Brinkmann, B. F. *et al.* VE-cadherin interacts with cell polarity protein Pals1 to regulate vascular lumen formation. *Mol. Biol. Cell* **27**, 2811–2821 (2016).
  175. Lampugnani, M. G. & Dejana, E. Interendothelial junctions: structure, signalling and functional roles. *Curr. Opin. Cell Biol.* **9**, 674–82 (1997).
  176. Bush, N. A. O., Chang, S. M. & Berger, M. S. Current and future strategies for treatment of glioma. *Neurosurgical Review* **40**, (2017).
  177. Wen, P. Y. & Kesari, S. Malignant gliomas in adults. *N. Engl. J. Med.* **359**, 492–507 (2008).
  178. Alphandéry, E. Glioblastoma treatments: An account of recent industrial developments. *Frontiers in Pharmacology* **9**, (2018).
  179. Alifieris, C. & Trafalis, D. T. Glioblastoma multiforme: Pathogenesis and treatment. *Pharmacology and Therapeutics* **152**, 63–82 (2015).
  180. Abbott, N. J., Rönnbäck, L. & Hansson, E. Astrocyte–endothelial interactions at the blood–brain barrier. *Nat. Rev. Neurosci.* **7**, 41–53 (2006).
  181. Janzer, R. C. & Raff, M. C. Astrocytes induce blood-brain barrier properties in endothelial cells. *Nature* **325**, 253–7
  182. Baeten, K. M. & Akassoglou, K. Extracellular matrix and matrix receptors in blood-brain barrier formation and stroke. *Dev. Neurobiol.* **71**, 1018–1039 (2011).
  183. Lalatsa, A. & Butt, A. M. Physiology of the Blood–Brain Barrier and Mechanisms of Transport Across the BBB. in *Nanotechnology-Based Targeted Drug Delivery Systems for Brain Tumors* 49–74 (Academic Press, 2018). doi:10.1016/B978-0-12-812218-1.00003-8
  184. Abbott, N. J., Patabendige, A. A. K., Dolman, D. E. M., Yusof, S. R. & Begley, D. J. Structure and function of the blood–brain barrier. *Neurobiol. Dis.* **37**, 13–25 (2010).
  185. Rosenberg, G. A. Neurological diseases in relation to the blood-brain barrier. *J. Cereb. Blood Flow Metab.* **32**, 1139–51 (2012).
  186. Booth, R. & Kim, H. Characterization of a microfluidic in vitro model of the blood-

- brain barrier ( $\mu$ BBB). *Lab Chip* **12**, 1784–1792 (2012).
187. Griep, L. M. *et al.* BBB on CHIP: Microfluidic platform to mechanically and biochemically modulate blood-brain barrier function. *Biomed. Microdevices* **15**, 145–150 (2013).
188. Kim, J. A. *et al.* Collagen-based brain microvasculature model in vitro using three-dimensional printed template. *Biomicrofluidics* **9**, 024115 (2015).
189. Achyuta, A. K. H. *et al.* A modular approach to create a neurovascular unit-on-a-chip. *Lab Chip* **13**, 542–553 (2013).
190. Ma, S. H., Lepak, L. A., Hussain, R. J., Shain, W. & Shuler, M. L. An endothelial and astrocyte co-culture model of the blood–brain barrier utilizing an ultra-thin, nanofabricated silicon nitride membrane. *Lab Chip* **5**, 74–85 (2005).
191. Brown, J. A. *et al.* Recreating blood-brain barrier physiology and structure on chip: A novel neurovascular microfluidic bioreactor. *Biomicrofluidics* **9**, 054124 (2015).
192. Deosarkar, S. P. *et al.* A Novel Dynamic Neonatal Blood-Brain Barrier on a Chip. *PLoS One* **10**, e0142725 (2015).
193. Wang, Y. I., Abaci, H. E. & Shuler, M. L. Microfluidic blood-brain barrier model provides in vivo-like barrier properties for drug permeability screening. *Biotechnol. Bioeng.* **114**, 184–194 (2017).
194. Akay, M. *et al.* Drug Screening of Human GBM Spheroids in Brain Cancer Chip. *Sci. Rep.* **8**, (2018).
195. Fan, Y., Nguyen, D. T., Akay, Y., Xu, F. & Akay, M. Engineering a Brain Cancer Chip for High-throughput Drug Screening. *Sci. Rep.* **6**, (2016).
196. Ayuso, J. M. *et al.* Glioblastoma on a microfluidic chip: Generating pseudopalisades and enhancing aggressiveness through blood vessel obstruction events. *Neuro. Oncol.* **19**, 503–513 (2017).
197. Yi, H.-G. *et al.* A bioprinted human-glioblastoma-on-a-chip for the identification of patient-specific responses to chemoradiotherapy. *Nat. Biomed. Eng.* **1** (2019). doi:10.1038/s41551-019-0363-x
198. Peterson, S. L., McDonald, A., Gourley, P. L. & Sasaki, D. Y.

- Poly(dimethylsiloxane) thin films as biocompatible coatings for microfluidic devices: Cell culture and flow studies with glial cells. *J. Biomed. Mater. Res.* **72A**, 10–18 (2005).
199. Piruska, A. *et al.* The autofluorescence of plastic materials and chips measured under laser irradiation. *Lab Chip* **5**, 1348 (2005).
200. Toepke, M. W. & Beebe, D. J. PDMS absorption of small molecules and consequences in microfluidic applications. *Lab Chip* **6**, 1484 (2006).
201. Paguirigan, A. L. & Beebe, D. J. From the cellular perspective: exploring differences in the cellular baseline in macroscale and microfluidic cultures. *Integr. Biol. (Camb)*. **1**, 182–95 (2009).
202. Wen, H., Hao, J. & Li, S. K. Characterization of Human Sclera Barrier Properties for Transscleral Delivery of Bevacizumab and Ranibizumab. *J. Pharm. Sci.* **102**, 892 (2013).
203. Chen, Z., Krishnamachary, B., Penet, M.-F. & Bhujwalla, Z. M. Acid-degradable Dextran as an Image Guided siRNA Carrier for COX-2 Downregulation. *Theranostics* **8**, 1–12 (2018).
204. Bloom, A. K., Samsom, M. L., Regmi, S. C., Steele, B. L. & Schmidt, T. A. Investigating the effect of proteoglycan 4 on hyaluronan solution properties using confocal fluorescence recovery after photobleaching. *BMC Musculoskelet. Disord.* **20**, 93 (2019).
205. Sadasivan, S., Zanin, M., O'Brien, K., Schultz-Cherry, S. & Smeyne, R. J. Induction of Microglia Activation after Infection with the Non-Neurotropic A/CA/04/2009 H1N1 Influenza Virus. *PLoS One* **10**, e0124047 (2015).
206. Gustafsson, S. *et al.* Blood-brain barrier integrity in a mouse model of Alzheimer's disease with or without acute 3D6 immunotherapy. *Neuropharmacology* **143**, 1–9 (2018).
207. Manaenko, A., Chen, H., Kammer, J., Zhang, J. H. & Tang, J. Comparison Evans Blue injection routes: Intravenous versus intraperitoneal, for measurement of blood–brain barrier in a mice hemorrhage model. *J. Neurosci. Methods* **195**, 206–210 (2011).

208. Xu, C.-J. *et al.* Evaluation of blood-brain barrier permeability in tryptophan hydroxylase 2-knockout mice. *Exp. Ther. Med.* **8**, 1467–1470 (2014).
209. Patel, M., Vadlapatla, R. K., Pal, D. & Mitra, A. K. Molecular and functional characterization of riboflavin specific transport system in rat brain capillary endothelial cells. *Brain Res.* **1468**, 1–10 (2012).
210. Zhang, Z. *et al.* Laser-triggered intraocular implant to induce photodynamic therapy for posterior capsule opacification prevention. *Int. J. Pharm.* **498**, 1–11 (2016).
211. Sharma, S., Brown, G. C. & Brown, M. M. The Cost-effectiveness of Photodynamic Therapy for Fellow Eyes with Subfoveal Choroidal Neovascularization Secondary to Age-related Macular Degeneration. *Ophthalmology* **6420**, 2051–2059
212. Hamblin, M. R. & Hasan, T. Photodynamic therapy: a new antimicrobial approach to infectious disease? *Photochem. Photobiol. Sci.* **3**, 436 (2004).
213. Dougherty, T. J. *et al.* Photodynamic Therapy: *J. Natl. Cancer Inst.* **90**, 40–45 (1998).
214. Zheng, Y. *et al.* Photodynamic-therapy Activates Immune Response by disrupting Immunity Homeostasis of Tumor Cells, which Generates Vaccine for Cancer Therapy. *Int. J. Biol. Sci.* **12**, 120–32 (2016).
215. Moan, J. On the diffusion length of singlet oxygen in cells and tissues. *J. Photochem. Photobiol. B.* **6**, 343–347 (1990).
216. Dysart, J. S. & Patterson, M. S. Characterization of Photofrin photobleaching for singlet oxygen dose estimation during photodynamic therapy of MLL cells *in vitro*. *Phys. Med. Biol.* **50**, 2597–2616 (2005).
217. Brown, S. B., Brown, E. A. & Walker, I. The present and future role of photodynamic therapy in cancer treatment. *Lancet Oncol.* **5**, 497–508 (2004).
218. Ash, C., Dubec, M., Donne, K. & Bashford, T. Effect of wavelength and beam width on penetration in light-tissue interaction using computational methods. *Lasers Med. Sci.* **32**, 1909–1918 (2017).
219. Sun, Z., Zhang, L.-P., Wu, F. & Zhao, Y. Photosensitizers for Two-Photon



- Excited Photodynamic Therapy. *Adv. Funct. Mater.* **27**, 1704079 (2017).
220. Bhawalkar, J. D., He, G. S. & Prasad, P. N. Nonlinear multiphoton processes in organic and polymeric materials. *Reports Prog. Phys.* **59**, 1041–1070 (1996).
221. Fowley, C., Nomikou, N., McHale, A. P., McCaughan, B. & Callan, J. F. Extending the tissue penetration capability of conventional photosensitisers: a carbon quantum dot–protoporphyrin IX conjugate for use in two-photon excited photodynamic therapy. *Chem. Commun.* **49**, 8934–8936 (2013).
222. Wachter, E., Heidary, D. K., Howerton, B. S., Parkin, S. & Glazer, E. C. Light-activated ruthenium complexes photobind DNA and are cytotoxic in the photodynamic therapy window. *Chem. Commun.* **48**, 9649–9651 (2012).
223. Ogawa, K. & Kobuke, Y. Two-Photon Photodynamic Therapy by Water-Soluble Self-Assembled Conjugated Porphyrins. *Biomed Res. Int.* **2013**, 125658 (2013).
224. Lan, M. *et al.* Water-Soluble Polythiophene for Two-Photon Excitation Fluorescence Imaging and Photodynamic Therapy of Cancer. *ACS Appl. Mater. Interfaces* **9**, 14590–14595 (2017).
225. Zhao, Y. *et al.* Polyethylene glycol-functionalized benzylidene cyclopentanone dyes for two-photon excited photodynamic therapy. *Org. Biomol. Chem.* **9**, 4168–4175 (2011).
226. Schmitt, J. *et al.* Diketopyrrolopyrrole-Porphyrin Conjugates with High Two-Photon Absorption and Singlet Oxygen Generation for Two-Photon Photodynamic Therapy. *Angew. Chemie Int. Ed.* **54**, 169–173 (2015).
227. Collins, H. A. *et al.* Blood-vessel closure using photosensitizers engineered for two-photon excitation. *Nat. Photonics* **2**, 420–424 (2008).
228. Khurana, M. *et al.* Quantitative In Vitro Demonstration of Two-Photon Photodynamic Therapy Using Photofrin<sup>®</sup> and Visudyne<sup>®</sup>. *Photochem. Photobiol.* **83**, 1441–1448 (2007).
229. Gu, B. *et al.* Precise Two-Photon Photodynamic Therapy using an Efficient Photosensitizer with Aggregation-Induced Emission Characteristics. *Adv. Mater.* **29**, 1701076 (2017).
230. Bolze, F., Jenni, S., Sour, A. & Heitz, V. Molecular photosensitisers for two-



- photon photodynamic therapy. *Chem. Commun.* **53**, 12857–12877 (2017).
231. Shen, Y., Shuhendler, A. J., Ye, D., Xu, J.-J. & Chen, H.-Y. Two-photon excitation nanoparticles for photodynamic therapy. *Chem. Soc. Rev.* **45**, 6725–6741 (2016).
232. Abrahamse, H. & Hamblin, M. R. New photosensitizers for photodynamic therapy. *Biochem. J.* **473**, 347–364 (2016).
233. Starkey, J. R. *et al.* New two-photon activated photodynamic therapy sensitizers induce xenograft tumor regressions after near-IR laser treatment through the body of the host mouse. *Clin. Cancer Res.* **14**, 6564–6573 (2008).
234. Imamura, Y. *et al.* Comparison of 2D- and 3D-culture models as drug-testing platforms in breast cancer. *Oncol. Rep.* **33**, 1837–1843 (2015).
235. Souza, A. G. *et al.* Comparative Assay of 2D and 3D Cell Culture Models: Proliferation, Gene Expression and Anticancer Drug Response. *Curr. Pharm. Des.* **24**, 1689–1694 (2018).
236. Yang, Y. *et al.* Evaluation of photodynamic therapy efficiency using an in vitro three-dimensional microfluidic breast cancer tissue model. *Lab Chip* **15**, 735–44 (2015).
237. Chen, Y.-C., Lou, X., Zhang, Z., Ingram, P. & Yoon, E. High-Throughput Cancer Cell Sphere Formation for Characterizing the Efficacy of Photo Dynamic Therapy in 3D Cell Cultures. *Sci. Rep.* **5**, 12175 (2015).
238. Moan, J. Porphyrin Photosensitization and Phototherapy. *Photochem. Photobiol.* **43**, 681–690 (1986).
239. Marinic, K. *et al.* Repeated exposures to blue light-activated eosin Y enhance inactivation of *E. faecalis* biofilms, in vitro. *Photodiagnosis Photodyn. Ther.* **12**, 393–400 (2015).
240. Farsari, M., Filippidis, G., Sambani, K., Drakakis, T. S. & Fotakis, C. Two-photon polymerization of an Eosin Y-sensitized acrylate composite. *J. Photochem. Photobiol. A Chem.* **181**, 132–135 (2006).
241. Deforest, C. A. & Anseth, K. S. Cytocompatible click-based hydrogels with dynamically tunable properties through orthogonal photoconjugation and

- photocleavage reactions. *Nat. Chem.* **3**, 925–931 (2011).
242. Lunzer, M. *et al.* A Modular Approach to Sensitized Two-Photon Patterning of Photodegradable Hydrogels. *Zuschriften Angewandte. Angew. Chem. Int. Ed.* **130**, 15342–15347 (2018).
243. Stryland, E. W. Van & Sheik-Bahae, M. *Z-Scan Measurements of Optical Nonlinearities. Characterization Techniques and Tabulations for Organic Nonlinear Materials* (1998). doi:10.1142/S0218863509004671
244. Sheik-Bahae, M., Said, A. A., Wei, T.-H., Hagan, D. J. & Van Stryland, E. W. Sensitive measurement of optical nonlinearities using a single beam. *IEEE J. Quantum Electron.* **26**, 760–769 (1990).
245. Gnoli, A., Razzari, L. & Righini, M. Z-scan measurements using high repetition rate lasers: how to manage thermal effects. *Opt. Express* **13**, 7976–7981 (2005).
246. Van Hoorick, J. *et al.* Highly Reactive Thiol-Norbornene Photo-Click Hydrogels: Towards Improved Processability. *Macromol. Rapid Commun.* (2018).
247. Kaiser, W. & Garrett, C. G. B. Two-Photon Excitation in  $\text{Ca F}_2 : \text{Eu}^{2+}$ . *Phys. Rev. Lett.* **7**, 229–231 (1961).
248. Göppert-Mayer, M. Über Elementarakte mit zwei Quantensprüngen. *Ann. Phys.* **401**, 273–294 (1931).
249. Huang, J., Meyer, C. & Zhu, C. T cell antigen recognition at the cell membrane. *Mol. Immunol.* **52**, 155–164 (2012).
250. Huppa, J. B. & Davis, M. M. *The Interdisciplinary Science of T-cell Recognition. Advances in Immunology* **119**, (Elsevier Inc., 2013).
251. Huppa, J. B. & Davis, M. M. T-cell Antigen Recognition and the Immunological Synapse. *Nat. Immunol.* **3**, 973–989 (2003).
252. Bashour, K. T. *et al.* Cross talk between CD3 and CD28 is spatially modulated by protein lateral mobility. *Mol. Cell. Biol.* **34**, 955–64 (2014).
253. Ovsianikov, A. *et al.* Two-Photon Polymerization of Hybrid Sol-Gel Materials for Photonics Applications. *Laser Chem.* **42**, 1–7 (2008).

## 6 Curriculum Vitae

### ■ Personal Data

---

Name: Agnes Dobos  
Academic degree: MSC  
Nationality: Hungarian  
Date of birth: 05. December 1989  
Place of birth: Budapest  
Email: agnes.dobos@ugent.be  
Tel.: +43 677-62136797

### ■ Education

#### **November 2016 – Today**

PhD Candidate

Technical University of Vienna (TU WIEN), Austria

#### **August 2015-June 2016**

Master degree in Experimental and Medical Biosciences *Double Degree*

Linköping University, Sweden

and

#### **Sept 2014-July 2015**

Master degree in Tissue Engineering and Regenerative Medicine MSc *Double Degree*

FH Technikum Wien, Austria

#### **Sept 2009– June 2014**

Bachelor degree in Biochemical Engineering

Budapest University of Technology and Economics, Hungary

## ■ Publications

1. M. Tromayer\*, A. Dobos\*, P. Gruber, A. Ajami, R. Dedic, A. Ovsianikov, R. Liska, "A biocompatible diazosulfonate initiator for direct encapsulation of human stem cells via two-photon polymerization," *Polym. Chem.* **2018**  
DOI: 10.1039/c8py00278a, \* equal contribution
2. A. Dobos, W. Steiger, D. Theiner, P. Gruber, M. Lunzer, J. Van Hoorick, S. Van Vlierberghe, A. Ovsianikov, "Screening of two-photon activated photodynamic therapy sensitizers using a 3D osteosarcoma model," *Analyst* **2019**  
DOI 10.1039/C9AN00068B.
3. A. Dobos, J. Van Hoorick, W. Steiger, P. Gruber, M. Markovic, O. G. Andriotis, A. Rohatschek, P. Dubruel, P. J. Thurner, S. Van Vlierberghe, S. Baudis, A. Ovsianikov "Thiol-Gelatin-Norbornene Bioink for Laser-Based High-Definition Bioprinting" *Advanced Healthcare Materials* **2019**  
DOI: 10.1002/adhm.201900752
4. W. Steiger, P. Gruber, D. Theiner, A. Dobos, M. Lunzer, J. Van Hoorick, S. Van Vlierberghe, R. Liska and A. Ovsianikov "Fully automated z-scan setup based on a tunable fs-oscillator" *Opt. Mater. Express* **2019**  
DOI: 10.1364/OME.9.003567
5. J. Van Hoorick, L. Tytgat, A. Dobos, H. Ottevaere, J. Van Erps, H. Thienpont, A. Ovsianikov, P. Dubruel, S. Van Vlierberghe "(Photo-)crosslinkable Gelatin Derivatives for Biofabrication Applications" *Acta Biomaterialia* **2019**  
DOI:10.1016/j.actbio.2019.07.035
6. A. Dobos, F. Gartner, M. Markovic, J. Van Hoorick, L. Tytgat, S. Van Vlierberghe and A. Ovsianikov "On-Chip High-Definition Bioprinting of Microvascular Structures" **2020 Submitted to Biofabrication**

7. L. Tytgat, A. Dobos, M. Markovic, J. Van Hoorick, F. Bray, C. Rolando, H. Thienpont, H. Ottevaere, P. Dubruel, A. Ovsianikov<sup>3</sup>, S. Van Vlierberghe "Two-photon polymerization of photo-crosslinkable recombinant collagen to serve tissue engineering applications" **2020 Submitted to *Biomacromolecules***

### Talks and Poster Presentations

- **Talk** "High resolution 3D printing, Hydrogels, and Biofabrication", ISBF, Ohio, USA, 2019
- **Poster Presentation** "High resolution 3D printing, Hydrogels, and Biofabrication", ESB, Dresden, Germany, 2019
- **Talk** "Organ-on-Chip Technologies", Brainstorms Festival, Vienna, Austria, 2019
- **Talk** "High resolution 3D printing, Hydrogels, and Biofabrication", CMIT Seminar Series, UCLA Los Angeles, USA, 2019
- **Talk** "High resolution 3D printing, Hydrogels, and Biofabrication", Austrian Cluster of Tissue Regeneration Annual meeting, Vienna, Austria, 2019
- **Poster Presentation** "Laser-based 3D printing of hydrogels: a versatile approach for accurate 3D cellular models", TERMIS, Tokyo, Japan, 2018
- **Talk** "On-Chip Two-Photon Polymerization of Vascular Structures" ISBF, Wurzburg, Germany, 2018
- **Talk** " Screening of Two-Photon Activated Photodynamic Therapy Sensitizers Using 3D Cancer Models" BSTE, Ghent, Belgium, 2018
- **Talk** "High-resolution 3D printing of biomimetic microenvironments to study T-cell activation", Wilhelm und Else Heraeus-Seminar: Micro-and Nanostructured Biointerfaces, Bad Honnef, Germany, 2018
- **Talk** "High resolution 3D printing, Hydrogels, and Biofabrication" Portuguese Association for Biofabrication, Porto, Portugal, 2018
- **Poster presentation** "Comparison of the Effect of Photoinitiator P2CK and AS7 on the Viability of Encapsulated Human Adipose-Derived Stem Cells via Two-Photon Polymerization", the Danube Vltava Sava Polymer Meeting (DVSPM), Vienna, Austria, 2017